STRENGTHENING MECHANISMS OF SPUTTERED COPPER, COBALT AND THEIR NANOCOMPOSITES

A Dissertation

by

YUE LIU

Submitted to the Office of Graduate and Professional Studies of
Texas A&M University
in partial fulfillment of the requirements for the degree of

DOCTOR OF PHILOSOPHY

Chair of Committee,	Xinghang Zhang
Committee Members,	Karl Hartwig
	Ibrahim Karaman
	Haiyan Wang
Head of Department,	Ibrahim Karaman

May 2014

Major Subject: Materials Science and Engineering

ABSTRACT

Low energy planar defects such as twin boundaries have been employed to strengthen materials effectively with insignificant loss of the conductivity and ductility. High density growth twins can be formed in low stacking fault energy (SFE) metals, such as copper (Cu) and silver (Ag). However, low SFE metal cobalt (Co) received little attention due to the complex coexistence of hexagonal close-packed (HCP) and face-centered cubic (FCC) structure. The focus of this research is to identify the strengthening mechanisms of planar defects such as twin boundaries, stacking faults, and layer interfaces in epitaxial FCC/HCP Co, and Cu/Co multilayers. Our studies show that epitaxial Cu/Co multilayers with different texture have drastic different mechanical properties, dictated by the transmission of partial vs. full dislocations across layer interfaces. Furthermore the mechanical properties of epitaxial Co are dominated by high density stacking faults. Moreover, by applying advanced nanoindentation techniques, such as thermal-drift corrected strain-rate sensitivity measurement, the mechanical properties including strain-rate sensitivity is accurately determined. By using in situ nanoindentation under transmission electron microscope (TEM), we determined deformation physics of nanotwinned Cu, including detwinning, dislocation-twin interactions and work hardening. This project provides an important new perspective to investigate mechanical behavior of nanostructured metals with high density stacking faults.

DEDICATION

This dissertation is dedicated to:

My wife, Chu Wang

and my daughter, Keyu Liu

ACKNOWLEDGEMENTS

First, I must thank my advisor, Dr. Xinghang Zhang for his support, guidance, and encouragement during my studies here at Texas A&M University. I thank my committee members, Drs. Karl Hartwig, Ibrahim Karaman, and Haiyan Wang for challenging me to produce great results in the pursuit of my degree. Additional thanks goes to Dr. Wang for the use of her laboratory facilities.

I greatly appreciate the Mechanical Engineering department staff at Texas A&M University, and I am indebted to the Materials Science and Engineering program coordinator, Jan Gerston, who guided me through my graduate studies.

I want to thank my collaborators from the Wang group, Joonhwan Lee, Jie Jian and from Agilent Company, Jennifer Hay, for their direct contributions to this work. I want to thank former Zhang research group members, Drs. Osman Anderoglu, Engang Fu, and Nan Li for their guidance as I began my graduate school career. I also want to thank my friends and coworkers, Steven Rios, Dr. Kaiyuan Yu, Dr. Daniel Bufford, Youxing Chen, Dr. Byoungsoo Ham, Dr. Cheng Sun, Miao Song, and Zhe Fan for contributions during meeting discussions, support when working late at night and taking classes, and in general, their companionship through my graduate school journey. Finally, I want to thank my wife, Chu Wang, for her constant support and understanding throughout the past years.

I acknowledge funding from the National Science Foundation's Division of Materials Research (NSF-DMR) grant program. I also acknowledge the Texas A&M University Microscopy Center and Materials Characterization Facility for the use of numerous microscopes and other instruments.

TABLE OF CONTENTS

Page

LIST OF FIGURES

Page

LIST OF TABLES

Page

LIST OF EQUATIONS

Page

CHAPTER I

INTRODUCTION

I.1 Strengthening Mechanisms of Various Interfaces

Interfaces are defined as three dimensional (3D) boundaries that isolate two distinct structures. These distinct structures can be different phases of dissimilar metallic materials, or different texture/orientation in a monolithic metallic material. Interfaces are one of the most critical factors for discovering strengthening mechanisms in materials. In this section, the strengthening mechanisms of various interfaces in materials are overviewed.

I.1.1 Grain Boundary Strengthening I – Hall-Petch Relation

As the most common type of interfaces, a grain boundary is an interface between two grains, or crystallites, in a polycrystalline material. This type of boundary tends to decrease the electrical and thermal conductivity of the material. Also, most grain boundaries are preferred sites for the onset of corrosion and for the precipitation of new phases from the solid. For mechanical properties, creep and strain rate sensitivity are affected by grain boundaries. Most importantly, because grain boundaries can block the motion of dislocation, reducing crystalline size is a common way to improve strength. The well-known Hall-Petch strengthening model is the first to quantify the relation between the mechanical strength and grain sizes. The Hall-Petch model

Equation 1 $$\boldsymbol{\sigma_y = \sigma_0 + kd^{-n}}$$

was first empirically derived for steels. Here σ_y is the yield strength, σ_0 is the friction stress, k is the Hall-Petch slope, d is the grain size, and n is a constant, typically ~ 0.5 [1,

2]. In this equation, σ_0 represents the contribution from the flow stress. The most famous aspect of this relationship is the $kd^{-1/2}$ relation. k represents the resistance of the grain boundaries to dislocation transmission, while the $d^{-1/2}$ quantifies the grain size dependence or the contribution from the grain boundary density.

When grain boundaries act as the dislocation obstacles, the dislocations are emitted from a source, and then piled up against these boundaries. The number of pile-up dislocation at an applied shear stress with a distance between source and obstacle can be described [3]

Equation 2 $$\boldsymbol{N = \frac{\pi L(1-\nu)(\tau-\tau_0)}{\mu b}}$$

where ν is the Poisson ratio, μ is the shear modulus, b is the length of the Burgers vector, τ_0 is the lattice friction, and L is the distance from a dislocation source to the grain boundary. When a leading dislocation in the pile-up is just able to cross the interface and is emitted to the other side of the boundaries, the stress reaches the barrier strength, τ^*. Therefore, the Hall-Petch relationship can be expressed as

Equation 3 $$\boldsymbol{\tau = \tau_0 + \left(\frac{\tau^* \mu b}{\pi(1-\nu)L}\right)^n}$$

where τ^* is the barrier stress, or critical stress required for cross slip across a grain boundary, n is a constant, typically ~ 0.5. Here L, the distance from a dislocation source to the grain boundary, represents the grain size (d) in general understanding. The most useful part of this form is that the strength contribution from k is expressed in terms of material parameters, including shear modulus, Poisson ratio, Burgers vector, and interface or barrier strength.

I.1.2 Grain Boundary Strengthening II – Nanocrystalline

As indicated in previous section, increasing the density of grain boundaries by refining the grain sizes as small as possible has been of great importance to the development of higher strength metals. When the grain size is less than 100 nanometers (nm), the material enters the so-called nanocrystalline regime. (As a side note, metals with 100-1000 nm grains are often termed “ultra-fine grained”, however, there is some overlap in terminology among various authors, and sometimes the terms are used interchangeably.)[4].

In comparison with the polycrystalline materials, nanocrystalline materials possess incredible densities of grain boundaries, and the interfaces properties become dominate factors to provide strengthening. Several important reviewer articles have demonstrated that nanocrystalline can provide great strengthening because of the resistance of high density grain boundaries. Furthermore, although greater strength can be achieved in nanocrystalline materials, a large deviation of the Hall-Petch relation indicates more complicated strengthening mechanisms rather than simply dislocation piling-up [4-6].

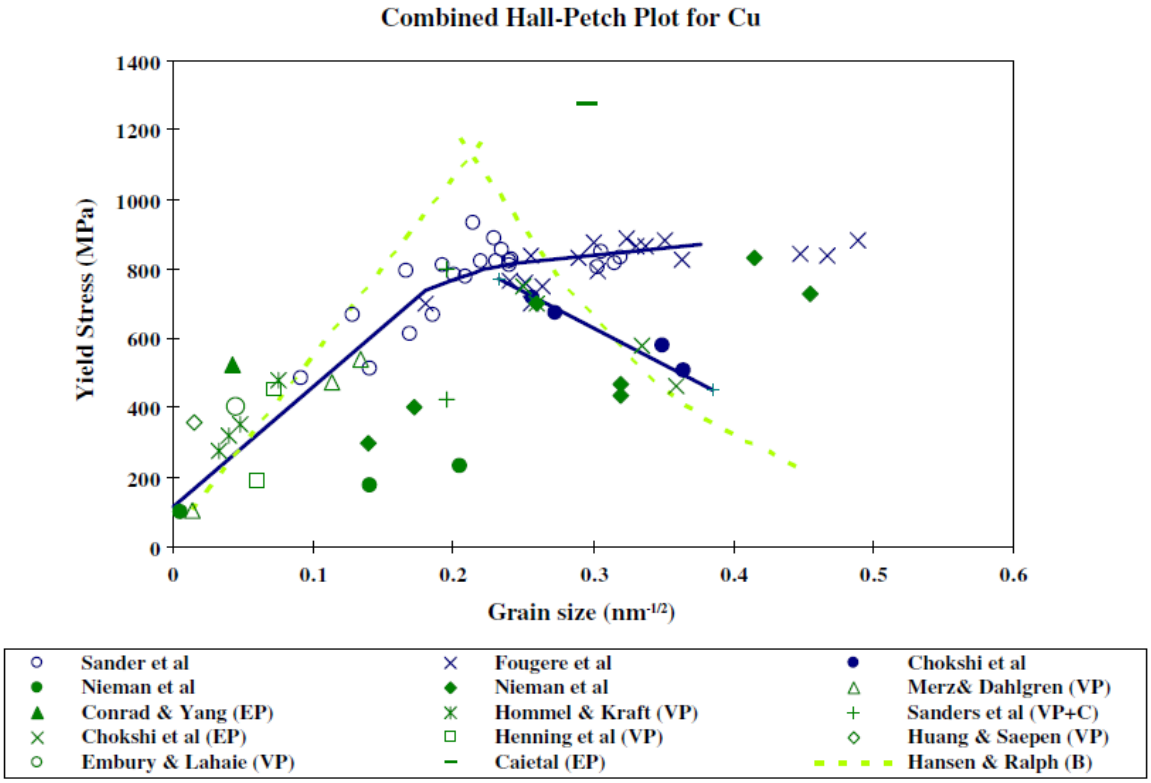

Figure 1 Compiled yield stress versus grain size plot for Cu from various sources ranging from coarse to nanograin size. The plot shows different trends as the grain size falls below a critical size.[6]

For example, Fig. 1 shows the Hall-Petch plot of nanocrystalline Cu from different sources. The saturation in strengthening may occur when grain size is below ~ 25 nm ($d^{-1/2}$=0.2). Some studies showed a trend of strength reduction, so-called reverse Hall-Petch relation [7]. The main reason of this large deviation to the Hall-Petch relation is the limited dislocation movement including dislocation piling-up in such small grain sizes. In other words, it is difficult to maintain the same type of dislocation activities in nanocrystalline materials. The possible mechanisms are proposed including break-up of dislocation pile-ups, grain boundary sliding, grain rotation, grain coalescence, or grain-boundary dislocation emission and annihilation [6].

Grain boundaries normally possess higher interfacial energies because of the large magnitude of incoherency between two distinct structures. This leads to the decrease of corrosion resistance, electrical and thermal conductivity. More importantly, ductility of nanocrystalline metals is often low, as a result of several factors: (1) artifacts from processing (porosity), (2) tensile instability, or (3) crack nucleation or shear instability. Dislocation-mediated plasticity can be suppressed at small length scales. Strain localization and reducing elongation to failure may occur in macroscopic specimens, especially at room temperature or below. Therefore, new strengthening methods are of great interest despite the introduction of low energy interfaces.

I.1.3 Interphase Boundary Strengthening – Multilayer Composites

Multilayer composites with interphase boundaries fabricated by thin film deposition techniques have received attention for various reasons. One feature that is particularly interesting is the ability to precisely tailor the alternating individual layer thickness as small as 1 nm, compared to several tens nm of grain size in nanocrystalline metals as described in the previous section. At this small length scale, multilayer composites have advanced properties, including giant-magnetron resistance [8, 9]; high mechanical strength and deformability [10-14]; and superior radiation tolerance [15-17], and hence may have various engineering applications.

Multilayer composites often exhibit layer-thickness-dependent strengthening and near-theoretical strength at ultra-small individual layer thicknesses. Fig. 2 presents the Hall-Petch plot of several Cu-based multilayer composites. Compared to Fig.1, this plot explores the mechanical properties when layer thickness (grain size) is below 5 nm. The

strengths are maintained at high strength (Cu/Nb, or Cu/Cr) or encountered a load-drop (Cu/Ni) when further reducing the layer thickness.

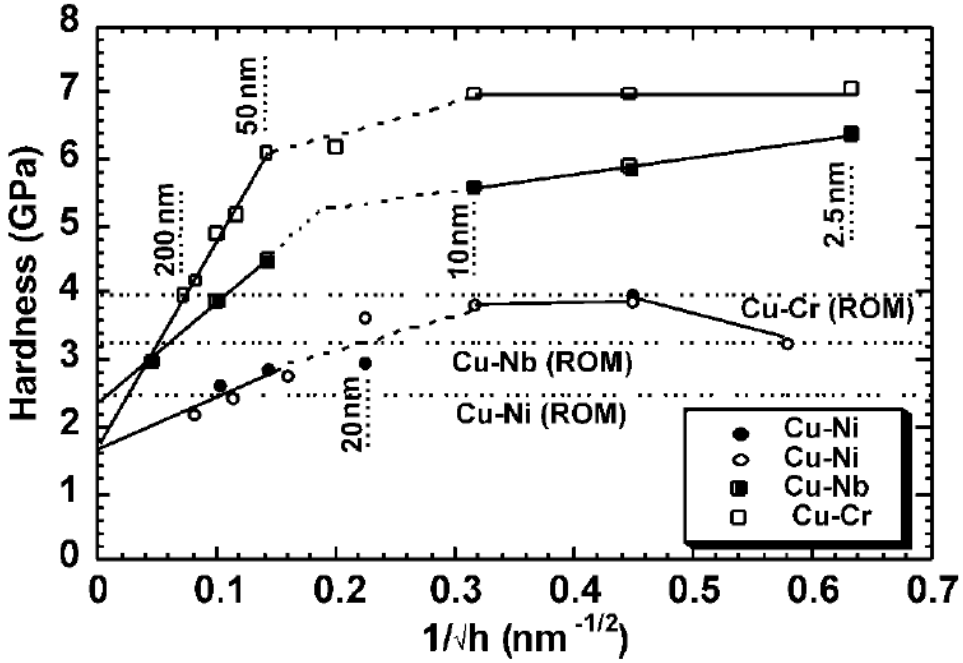

Figure 2 The dependence of hardness on layer thickness (*h*) for Cu-Ni, Cu-Cr and Cu-Nb multilayers. The rule of mixtures (ROM) are indicated by dotted lines for each of the three systems respectively [10].

The schematic in Fig. 3 explicitly explains the strengthening mechanisms of multilayer strength at different length scale (individual layer thickness). When individual layer thickness, *h*, is greater than 50 nm, dislocations that pile-up on layer interfaces are dominated mechanisms. Thus the strengthening behavior typically follows Hall-Petch (H-P) relation [1, 2, 18-20]. When 50 nm > *h* > 10 nm, the pile-up of dislocations are limited in such small length scale. The dislocation movement is confined within layers. Thus the corresponding strengthening mechanism can be described by the confined layer slip (CLS) model that considers bowing of dislocations [3, 21-23]. When h reduces to several nanometers, multilayers frequently achieve their maximum strength, which is determined

by numerous factors including Koehler stress that comes from modulus mismatch [24, 25], misfit dislocations, coherency stress [26-30], texture [31], twinning [32-35], and interface shear strength [36, 37]. At this length scale, the interface properties are primary factors on strengthening.

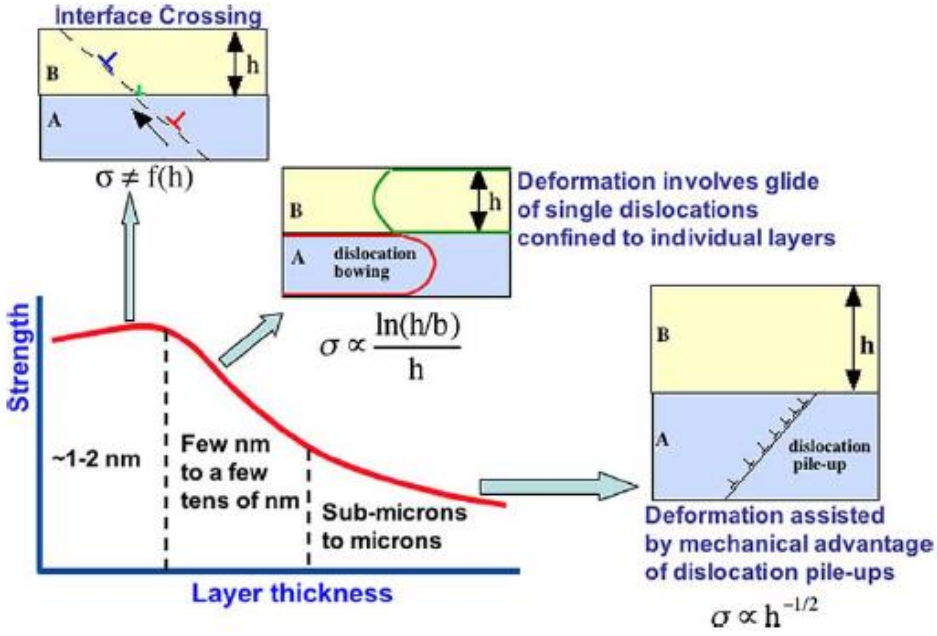

Figure 3 Schematic illustration of the dislocation mechanisms of multilayer strength operative at different length scale [3].

Misfit dislocation and coherency stress originate from lattice mismatch between two materials [38, 39]. In coherent systems (two materials have similar lattice parameters, such as Cu/Ni), the elastic strain energy builds up at greater layer thickness, *h*. When h exceeds critical thickness, misfit dislocations form to release elastic strain energy [40-42]. Koehler stress arises from the elastic modulus mismatch between neighboring layers and becomes significant when a large modulus difference exists [25]. In incoherent systems (two materials have large lattice parameters, such as Cu/Nb and Cu/Cr), a hardness plateau is typically observed at smaller value of *h* [3, 12, 43, 44],

wherein certain coherent systems, such as Cu/Ni, softening (the reduction of hardness at smaller h) occurs due to the formation of fully coherent interfaces [18, 31]. This is due to these coherent interfaces are less effective barriers to the transmission of dislocations compared with incoherent interfaces [45]. In incoherent systems, interfaces retain slip discontinuity and remain strong barriers to the penetration of dislocations [46]. When multilayer composites using interphase interfaces to strengthen materials, the interface energy is either comparable or slightly lower than grain boundaries. As a type of low energy interfaces, twin boundaries have drawn great interesting in past several decades.

I.1.4 Twin Boundary Strengthening

Twin boundary is a special class of grain boundaries in which the lattices on either side are related by mirror symmetry across the so-called twinning plane. Common twinning planes vary from one crystal structure to the next. For Faced Centered Cubic (FCC) metals, two of the most important twin boundaries are: the Σ3 (111) coherent twin boundary (CTB) and Σ3 (112) incoherent twin boundary (ITB). Compared to a grain boundary, twin boundary has a more coherent structure with less free volume as shown in Fig. 4.

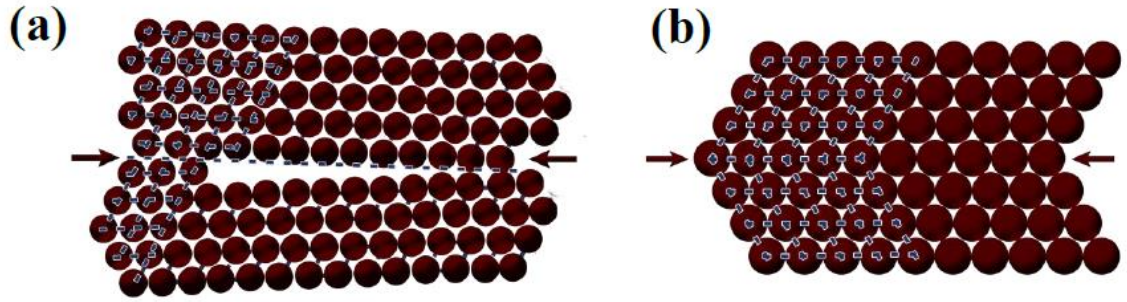

Figure 4 Schematics comparison of (a) a grain boundary and (b) a Σ 3 (111) coherent twin boundary (CTB), the CTB shows more coherent structure with less from volume.

Due to interface structure configurations, the interfacial energies of CTBs, ITBs, conventional high and low angle grain boundaries differ dramatically. For example, in Cu, the CTB, ITB, and high angle grain boundary energies are 24-39, 590-714, and 625-710 mJ/m2, respectively [47-49]. Among these interfaces, the CTBs often possess the lowest energy which makes CTBs much more stable than many other grain boundaries.

High density nanotwinned metals (average twin spacing is less than 100 nm) often show very high mechanical strength. This is because twin boundary blocks dislocation transmission with a strength comparable to that of conventional grain boundaries. Increasing densities of twin boundaries result in enhanced mechanical strength, similar to increasing grain boundary density, as previously mentioned. However, twin boundaries are highly coherent, and thus lack free volume. Some combinations of properties in nanotwinned metals are not commonly associated with each other, and at times are seemingly paradoxical. For example, nanocrystalline Cu shows increased strength with decreasing ductility compared with polycrystalline Cu. This phenomenon is a result of small grain size inhibiting dislocation-mediated plasticity. However, it has been shown that nanotwinned Cu may exhibit both high strength and good ductility as shown in Fig. 5[50]. Furthermore, unlike the nanocrystalline Cu, the electrical resistivity of nanotwinned Cu does not increase with increased of twin boundary density.

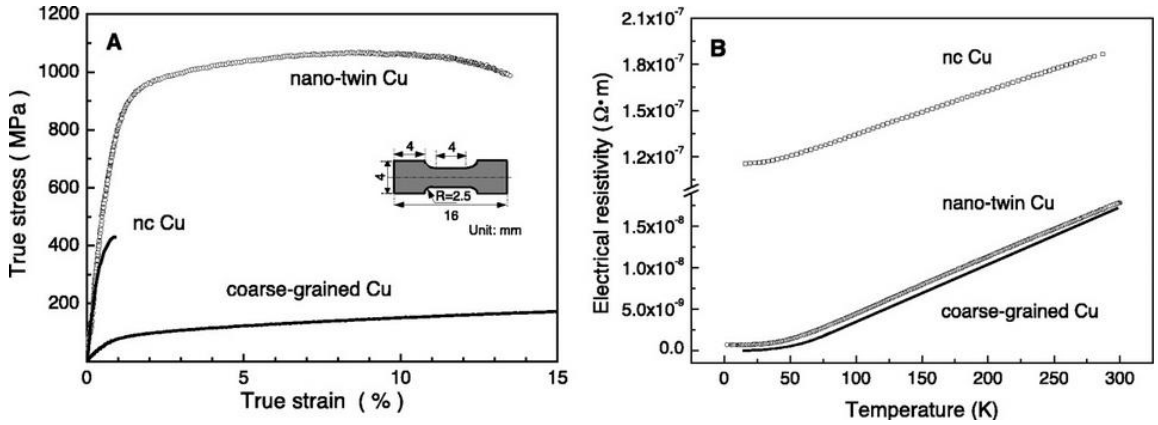

Figure 5 (a) Tensile stress-strain curve for the electro-deposited nanotwinned Cu in comparison with that for a coarse-grained polycrystalline Cu (~100 μm grain size) and a nanocrystalline Cu (~30 nm grain size); (b) electrical resistivity of nanotwinned Cu sample at various temperature in comparison with that of polycrystalline and nanocrystlaline Cu[50]

Twin boundaries play a significant role in dislocation blocking and generation, and thus are important to strengthening. As a coherent interface, twin boundary may also encounter a softening if the average twin spacing is further reduced. This is the similar to the phenomenon in coherent multilayer composites as previous mentioned. Fig. 6 shows how strength and ductility vary with twin thickness in nanotwinned Cu. The strength reaches a maximum when average twin thickness is 15 nm, but falls for thinner twin thickness [51]. It is worth noting that when the average twin thickness is further reduced from 15 nm to 4 nm, the ductility increases dramatically. One possible explanation is the less stability but large plastic strain accommodation of fine twins. A recent study on nanotwinned Cu revealed that most of fine twins are removed after plastic rolling [52]. As shown in Fig. 7, the twin boundaries sustain large amount of dislocations after ~ 50% plastic deformation. Twin boundaries appear to act as sinks for dislocations during high-strain deformation induced via rolling.

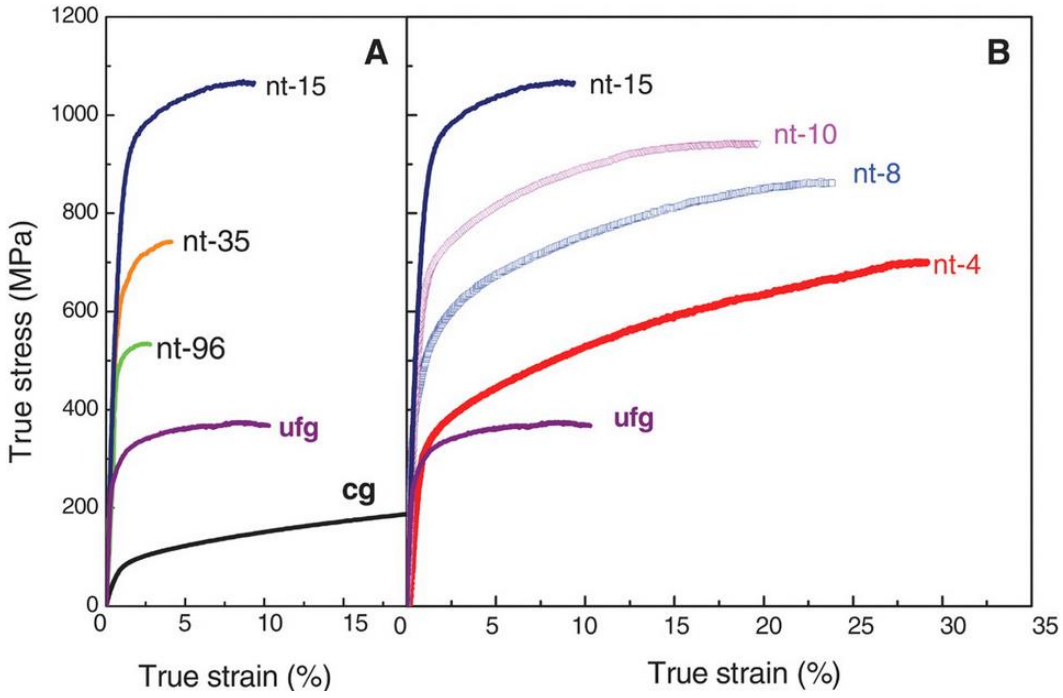

Figure 6 Tensile test stress-strain curves from Cu with ufg and coarse-grained microstructures, as well as nanotwinned (nt) Cu with average twin thickness varying from 4 to 96 nm. The box on the left shows both increasing strength and ductility with decreasing twin thickness, with a maximum strength achieved at 15 nm. On the right, twin thickness is decreased from 15 to 4 nm. Strength falls, but ductility increases at this length scale [51]

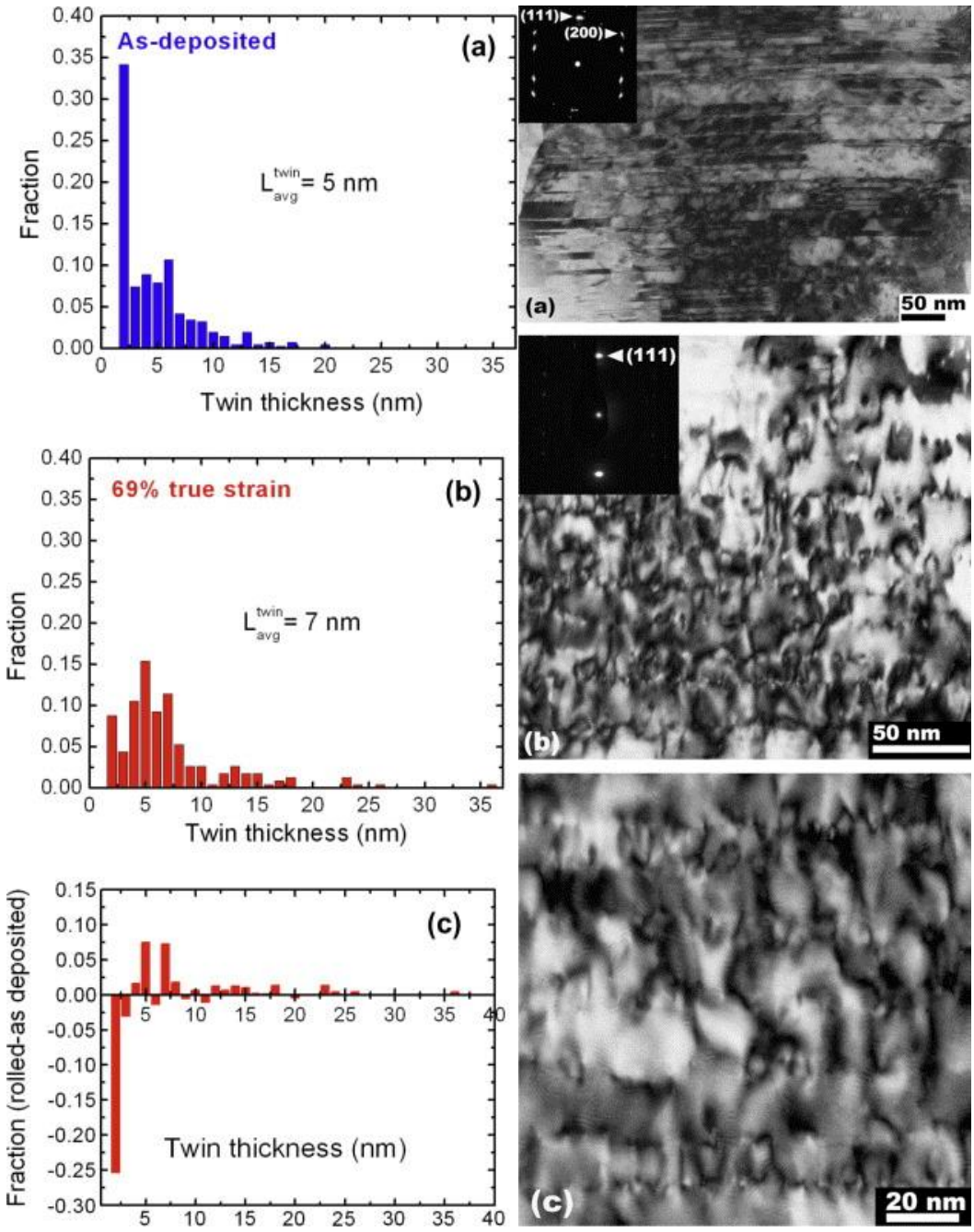

Figure 7 Plastic rolling on nanotwinned Cu showing that twin boundary sustains large amount of dislocations; ultrafine twins is less stable than thicker twins [52]

Under deformation, twin may change in average thickness or ITBs (incoherent twin boundaries) may migrate on (111) planes. Recent *in situ* nanoindentation studies inside of a TEM observed the interactions between dislocations and CTBs that resulted in

the generation of new dislocations, so-called dislocation multiplication. [53]. Since thinner twins are easier to move, ITB migration often results in the elimination of thinner twins, leading to decreased twin density. It was mentioned that ITBs may migrate as a result of stress as shown in Fig. 8. These studies shed some light on the mechanisms by which twin boundaries may move and interact with dislocations during deformation, and may help to explain the improved elongation to failure observed in nanotwinned Cu.[54]

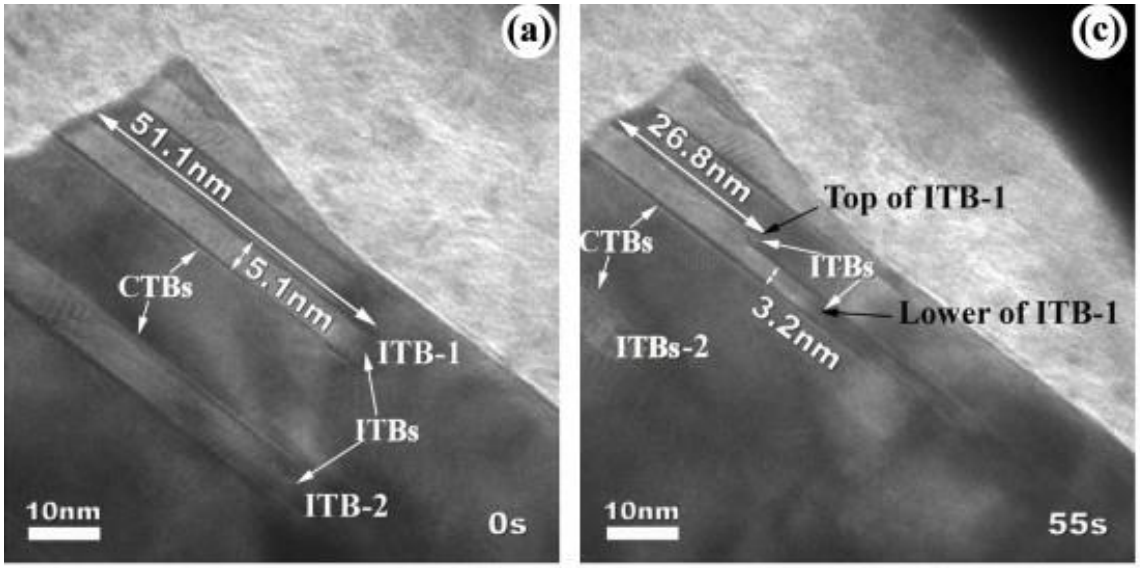

Figure 8 *in situ* nanoindentation on nanotwinned Cu shows the migration of ITBs, and thickness reduction of the fine twins[54]

In this section, the strengthening mechanisms of various interfaces are overviewed. In comparison with the Hall-Petch relation in conventional polycrystalline materials, nanocrystalline materials deviated from that relation when strength either become saturated or decreased if further reducing the grain sizes. Compared to nanocrystalline metals, multilayer composites explore the interface properties dominated strengthening mechanisms when layer thickness/grain sizes are less than 5 nm.

Furthermore, the strengthening mechanisms of the low energetic twin boundaries are introduced as a possible solution to overcome the strength-ductility paradox. Twin boundaries can sustain dislocation, but fine twins may migrate under stress.

I.2 Formation Mechanisms of Twin Boundaries

As previously mentioned, nanotwinned metals exhibit high strength due to (111) coherent twin boundaries (CTB) and can provide great strengthening by resisting dislocation slip transfers [55-60]. Furthermore, nanotwinned materials show better ductility [51, 61, 62], thermal stability [63-65], creep and fatigue resistance [66-68], and electrical conductivity [50, 69, 70] compared to nanocrystalline metals. In this section, the formation mechanisms of the twin boundaries are discussed.

There are several ways to introduce twin boundaries. The most common is post-processed methods including severe plastic deformation, annealing, phase transformation, and surface mechanical attrition treatment (SMAT) where large stress can be introduced [71-74]. In particular, deformation twins form by a homogeneous simple shear of the parent lattice under stress, at temperatures below those at which individual atoms move by diffusion. These post-processed twins are less favored because of low density twin formation, large twin spacing, and high dislocation density.

Recently, high density nanotwins can be introduced by simple growth process, for example electro-deposition or physical vapor deposition. In the following section, the formation mechanisms of high density growth twin boundaries are discussed particularly.

I.2.1 Growth Twins in Low Stacking Fault Energy Metals

Most studied growth nanotwinned metals have low stacking fault energy (γ_{sf}). This is because low γ_{sf} metals tend to form twin boundaries more easily than those with higher γ_{sf}. For example, Cu and Ag form abundant growth twin boundaries during magnetron sputtering, one type of physical vapor deposition technique. A thermodynamic model derived from nucleation theory predicts that the probability of forming a twinned nucleus and a perfect nucleus[33] can be expressed as

Equation 4 $$\boldsymbol{\gamma^*_{perfect}} = \frac{\boldsymbol{\gamma}}{\left(\frac{\boldsymbol{kT}}{\boldsymbol{\Omega}}\boldsymbol{\ln}\left[\frac{\boldsymbol{J\sqrt{2\pi mkT}}}{\boldsymbol{P_s}}\right]\right)}$$

Equation 5 $$\boldsymbol{\gamma^*_{twin}} = \frac{\boldsymbol{\gamma}}{\left(\frac{\boldsymbol{kT}}{\boldsymbol{\Omega}}\boldsymbol{\ln}\left[\frac{\boldsymbol{J\sqrt{2\pi mkT}}}{\boldsymbol{P_s}}\right]-\frac{\boldsymbol{\gamma_{sf}}}{\boldsymbol{2h}}\right)}$$

where k is the Boltzmann constant, T is the substrate temperature during deposition, Ω is the atomic volume, J is the deposition flux, P_s is the vapor-pressure above solid, m is the atomic mass of depositing species, γ_{sf} is the stacking fault energy. Comparing these two equations, if the γ_{sf} is small and the volume free energy difference ($\frac{\boldsymbol{kT}}{\boldsymbol{\Omega}}\boldsymbol{\ln}\left[\frac{\boldsymbol{J\sqrt{2\pi mkT}}}{\boldsymbol{P_s}}\right]$) is large, the difference between $\boldsymbol{\gamma^*_{perfect}}$ and $\boldsymbol{\gamma^*_{twin}}$ will be negligibly small, and the possibility of twinned nuclei formation is similar to that of perfect nuclei formation. Therefore, either low γ_{sf} or high deposition flux contributes the most to the formation of nanoscale twins. Fig. 9 (a) shows the calculation of radius differences between perfect and twin nuclei at different deposition rates, and (b) the evidence of high density growth twins in sputtered Ag [75].

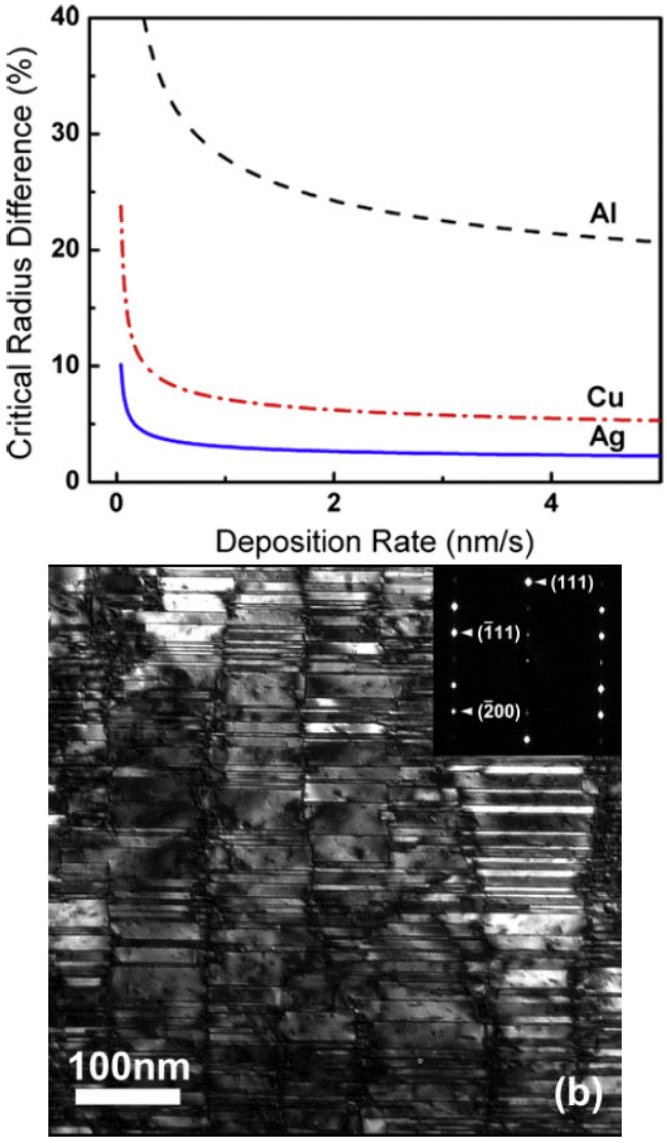

Figure 9 (a) The calculation of radius differences between perfect and twin nuclei at different deposition rates; and (b) the evidence of high density growth twins in sputtered Ag. High density growth twins are more favored in lower stacking fault energy metals at higher deposition rates [75]

At low deposition rates, incoming atoms have ample time to diffuse to their ideal lattice sites. Increasing deposition rate results in the formation of more growth defects, as incoming atoms have less time to reach equilibrium lattice sites before more atoms pile up. Hence, the high deposition rate is preferable for twin formation. As shown in Fig. 10, higher deposition rates result in enhanced twin formation in sputtered Cu films [76].

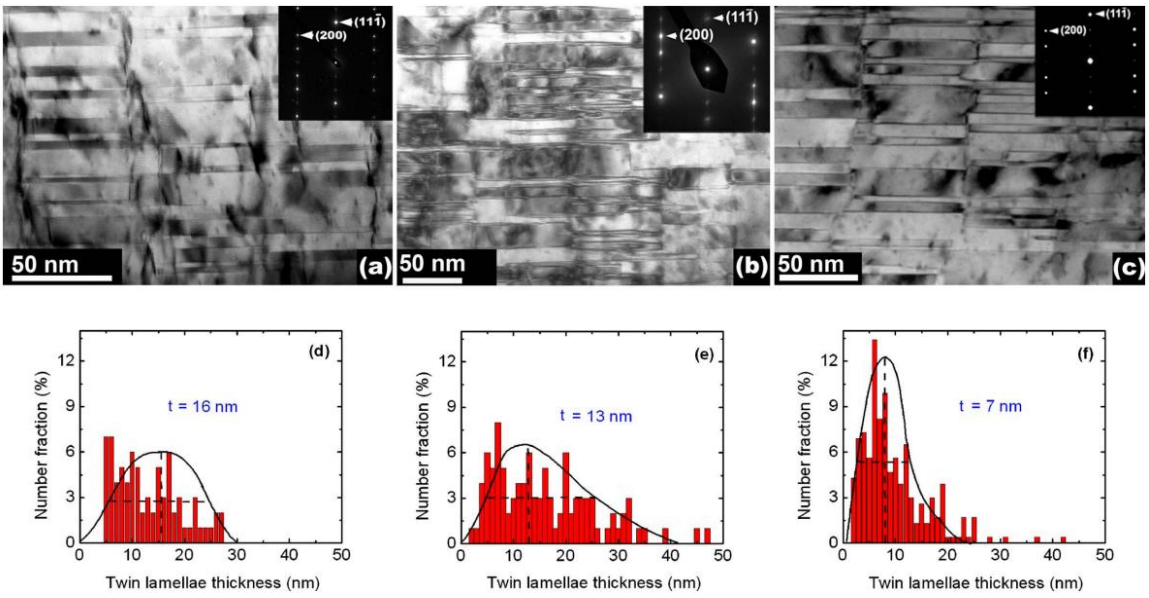

Figure 10 Cross-section TEM images of Cu films deposited at (a) 9A/s, (b) 30A/s, and (c) 40A/s, examined from <110> direction. (d-f) Statistical distribution of twin thicknesses deposited at 9, 30 and 40 A/s, respectively. Average twin thickness decreases with increasing deposition rate [76].

Table 1 The stacking fault energy (SFE) of various metals

Metal	Ag	Co	Au	Cu	Ni	Pd	Al
SFE (mJ/m^2)	16	12~24	32	41	125	160	166

As shown in Table 1, growth twins can be achieved in low stacking fault energy including Cu, Ag, Co etc. For metals with high value of γ_{sf}, simply increasing the deposition rate is not sufficient to induce growth twin formation.

The tendency of a metal to form twins, *T*, is used to better understand the stacking fault energy effect on twin formation [77]. This property is related to the stacking fault energy (γ_{sf}), twin boundary energy (γ_t), and more importantly the ratio of unstable stacking (γ_{us}) to twinning energy (γ_{ut}). Generally these energies correlate to each other, hence fcc metals with low γ_t form twins most readily during nucleation or deformation. Tendency, *T*, is defined as

Equation 6 $$\boldsymbol{T = \lambda_{crit}\sqrt{\frac{\gamma_{us}}{\gamma_{ut}}}}$$

where λ_{crit} is a normalized nucleation load dependent on γ_{sf}, γ_{ut}, ν, and several parameters defining the geometry of the crack. It is noteworthy that *T* is a competition between twinning and full dislocation emission. The incidence of twinning increases as cross slip is inhibited in low γ_{sf} metals. T explains some seemingly paradoxical behavior, such as why Al rarely twins, while Pd, a metal with similar γ_{sf}, will show deformation twinning. This is because Al and Pd have dissimilar γ_{us} /γ_{ut} ratios, which causes Pd to twin more easily than Al.

It should be noted that lowering γ_{sf} by alloying is a well-known method for increasing the tendency of a metal to twin. However, sometimes the properties of the pure metal might be adversely affected by alloying (e.g., in the case of electrical conductors). As we will see later in this section, other methods exist for inducing twins without varying the γ_{sf}.

I.2.2 Growth Twins in High Stacking Fault Energy Metals

Recent studies on metallic multilayer composites have proposed another approach to introduce nanotwins into high SFE metals, such as Al, Ni, by forming coherent or

semi-coherent interfaces with low SFE Cu and Ag [32, 78-83]. Due to the extra elastic stress rising from lattice mismatch, high density twins can form in Cu or Ag seed layers and penetrate into Ni or Al over layers as shown in Fig. 11. This method sheds light on how to grow twins directly in high SFE metals by providing interfaces from low SFE metals.

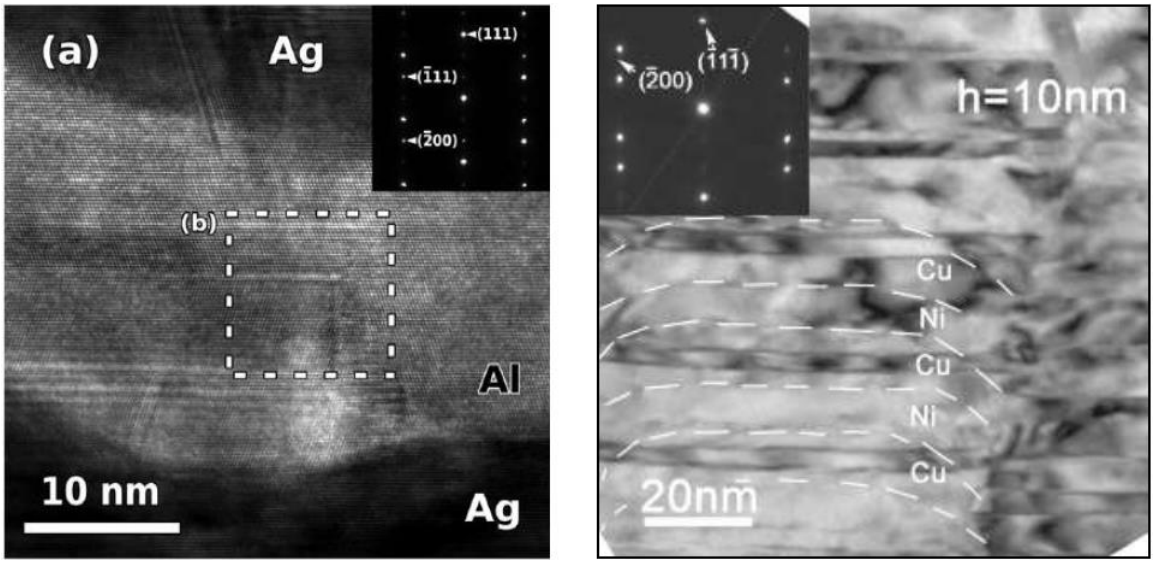

Figure 11 Possibility to form twins in high stacking fault energy Al and Ni, evident by fabricating (a) Ag/Al and (b) Cu/Ni multilayer composites[79, 80]

Here shows one example of the nucleation of twins in Cu/Ni multilayers via shear stress induced Shockley partials. During the island growth process, adatoms are typically attached to the peripherals of terraces, as shown schematically in Fig. 12. At the surface of the free edge, there is no stress. However inside the island, biaxial stress quickly arises to a steady state value, i.e. coherency stress (coming from mismatch strain) in this case. The coherency stress in films is known to be transferred by a shear stress between film (Cu) and substrate (Ni) at the corner of the islands. Such a shear stress may promote the

formation of partials, and hence generate twins. The magnitude of shear stress, τ, can be roughly estimated as follows [84]

Equation 7 $$\tau \approx \boldsymbol{\sigma_m}\sqrt{\frac{kh_f}{2\pi x}}$$

where σ_m is the biaxial mismatch stress in films, h_f is the film thickness, and x is the distance from film edge. k is the biaxial modulus ratio between substrate and films, and can be calculated by[84]

Equation 8 $$\boldsymbol{k} = \frac{\frac{E_s}{1-\nu_s}}{\frac{E_f}{1-\nu_f}}$$

where E and ν are respective modulus and Poisson's ratio of substrate and film. The magnitude of shear stress typically decreases rapidly when atoms are away from film edges. In the case of epitaxial growth of Cu (film) on Ni (substrate), k is estimated to be ~ 2. σ_m can be calculated by $\varepsilon_{max}E_{Cu}/(1-\nu_{Cu})$, where ε_{max} is the mismatch strain, ~ 2.3% between Cu and Ni. Then τ is estimated to be 1.3 – 2.2 GPa when x is 1-3 times greater than the film thickness. It has been shown that a shear stress of ~ 540 MPa is necessary to create Shockley partials in Cu.

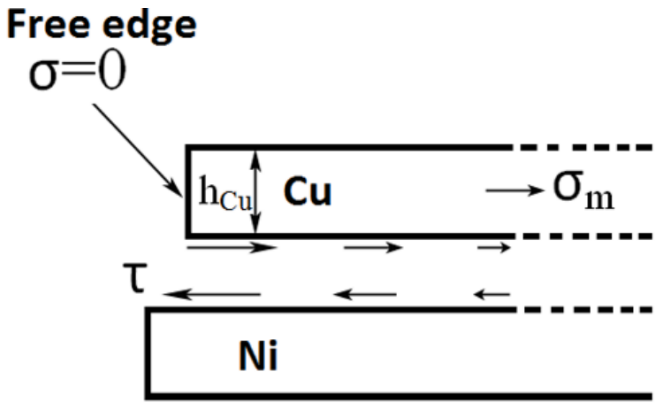

Figure 12 Schematics for shear stress in Cu/Ni nuclei. Shear stresses in Cu and Ni at interfaces quickly decay at increasing distance from the stress-free surface. The magnitude of shear stress is sufficient to generate sequential partials which in turn lead to the formation of nanotwins.[80]

In this section, the formation mechanisms of growth twins are overviewed. Higher deposition rates can increase the growth twin density in low stacking fault energy metals, such as Ag and Cu. In order to form high density twins in high stacking fault energy metals including Ni and Al, fabricating multilayer composites is a validated approach by forming coherent or semi-coherent interfaces with low SFE Cu and Ag.

I.3 Stacking Faults

As previously mentioned, twin boundary is an intrinsic low-energy coherent interface that follows mirror symmetry. Common twinning planes in FCC crystals are (111) closed packed planes. Twin boundaries have great advantages on strengthening but not losing much ductility. Thus, as the other (111) low energy coherent interfaces, stacking faults has drawn great attention recently on their formation and strengthening mechanisms.

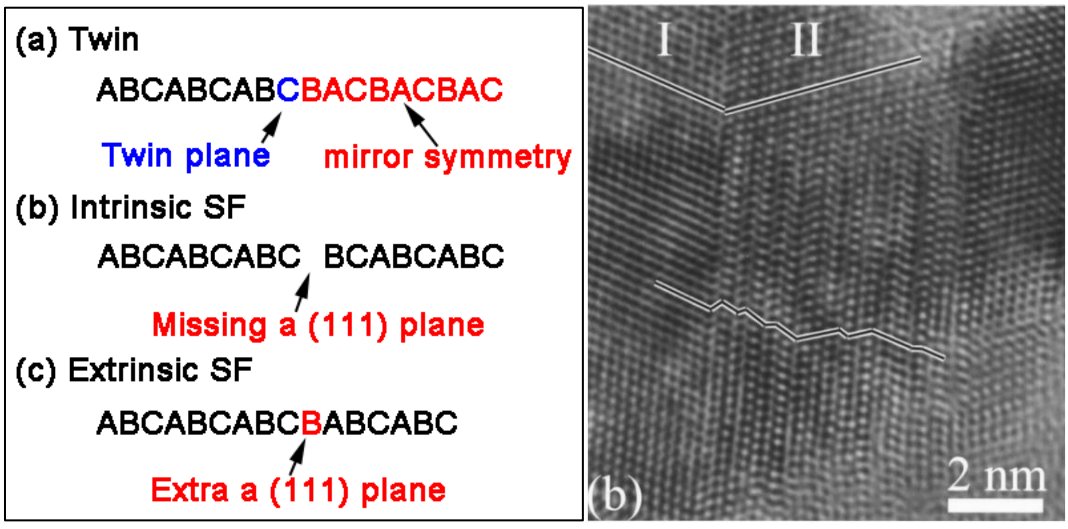

Figure 13 (a) The stacking sequence of a twin, and intrinsic and extrinsic stacking fault. (b) High resolution bright field TEM of a twin boundary and a set of stacking faults in deformed nanocrystalline Cu. The upper part of the image shows only symmetric twin domains (I and II), while the lower part have a lot of microtwins and stacking faults marked by the virtual guide [85].

To better understand the formation and strengthening mechanisms of the stacking faults, it is necessary to first differentiate the stacking sequence of twin boundaries and stacking faults, for example, in FCC crystals. Fig. 13(a) shows the stacking sequence for a twin, an intrinsic and extrinsic stacking fault (SF) on closed packed (111) planes. "ABC" represent three types of (111) periodic planes with the differences of a Burgers vector $\frac{1}{6} < 112 >$. The twinning plane is formed by in-plane shearing, while the stacking faults refer to insert or remove a (111) plane. Fig. 13(b) gives an example of a twin and a set of stacking faults in deformed nanocrystalline Cu by a high resolution TEM image. The upper part of the image shows only symmetric twin domains (I and II), while the lower part have a lot of microtwins and stacking faults marked by the virtual guide.

Although the twin boundary energy is estimated as half of stacking fault energy [49], the stacking fault energy is still much lower if compared to conventional grain boundary energies. Therefore, stacking fault energy, which is an intrinsic material property, can be used to characterize the coherent interfaces including both twins and stacking faults. Rest of this section will discussed the formation of the stacking faults, and their strengthening mechanisms.

I.3.1 Stacking Faults Formation

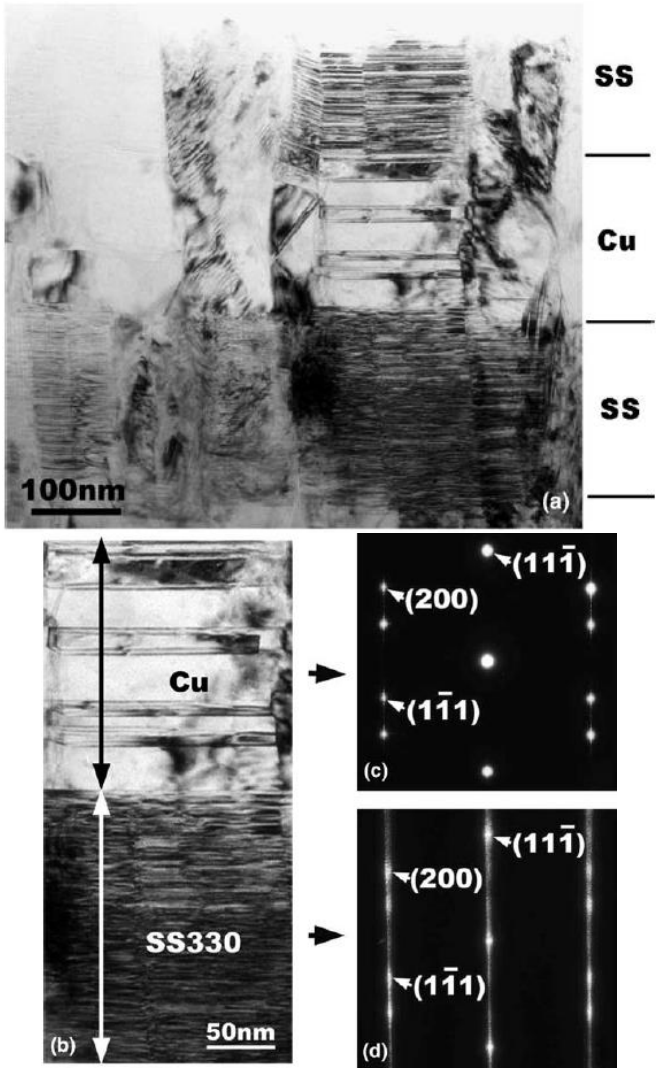

Figure 14 (a) Low magnification cross-section TEM of Cu/330 SS multilayer with a 200 nm thickness for each layer, showing high density twins in Cu layer and high density of stacking faults in SS 330. (b)Enlarged TEM image of one Cu/SS330 bilayer, Cu layer show twinning, while the SS330 has high density of stacking faults. (c) SAD of Cu showing a typical twinning structure, and (d) SAD of SS330 showing the evidence of stacking faults (striking lines)[33]

Stacking faults are commonly observed especially in heavily deformed metals with sufficiently low stacking fault energies. The processing methods include cryo or room temperature ball milling [86]; surface mechanical attrition treatment [87, 88]; tensile deformation [89, 90]; and high pressure torsion [85]. The large stress that

introduced by these deformation methods is sufficient to provide shear stress on forming stacking faults.

Some stacking faults can be achieved by thin film deposition technique. For example, Fig. 14 shows high density stacking fault ribbons have been seen in sputtered stainless steel (SS) 330 that has ultra-low stacking fault energy [33, 91]. Furthermore, high resolution TEM images in same studies reveal the differences of twin (in Cu) and stacking faults (in SS330) as shown in Fig. 15. SAD is another powerful tool to identify the difference between stacking faults (striking lines) and twinning (mirror symmetry).

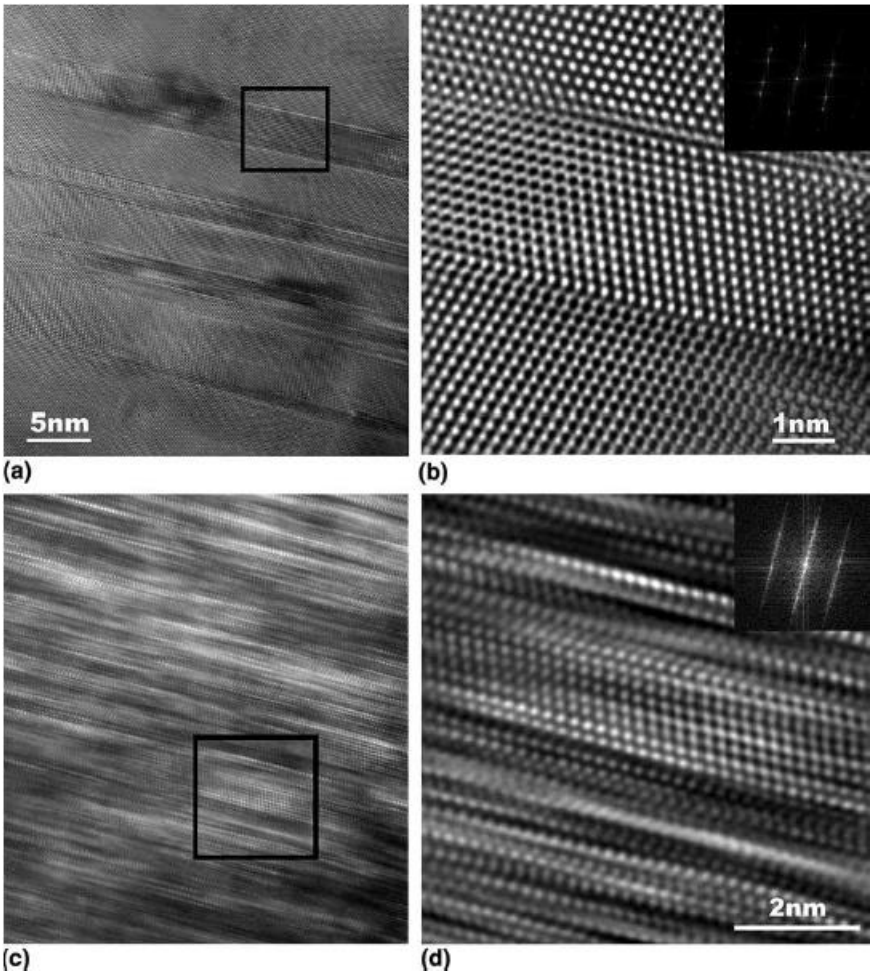

Figure 15 (a) HRTEM image of twinning in Cu (b) Enlarged view of the square in (a) showing regular nanoscale twinning in Cu. (c) HRTEM image of stacking faults in SS 330. (d) Enlarged view of the square in (c) showing extremely fine stacking faults [33].

Besides of deformation induced stacking faults, and growth stacking faults in ultra-low stacking fault energy metals. Recent studies on defect-twin boundaries interaction in nanotwinned Ag exhibit the twin boundaries to stacking faults transition during heavy-ion irradiation [92]. As shown in Fig.16, since twin boundaries act as defect sinks, the new stacking faults will form when the twin boundaries interact with radiation induced defect such as stacking fault tetrahedral (SFT). This might due to the higher boundary energy of stacking faults, compared to that of coherent twin boundaries.

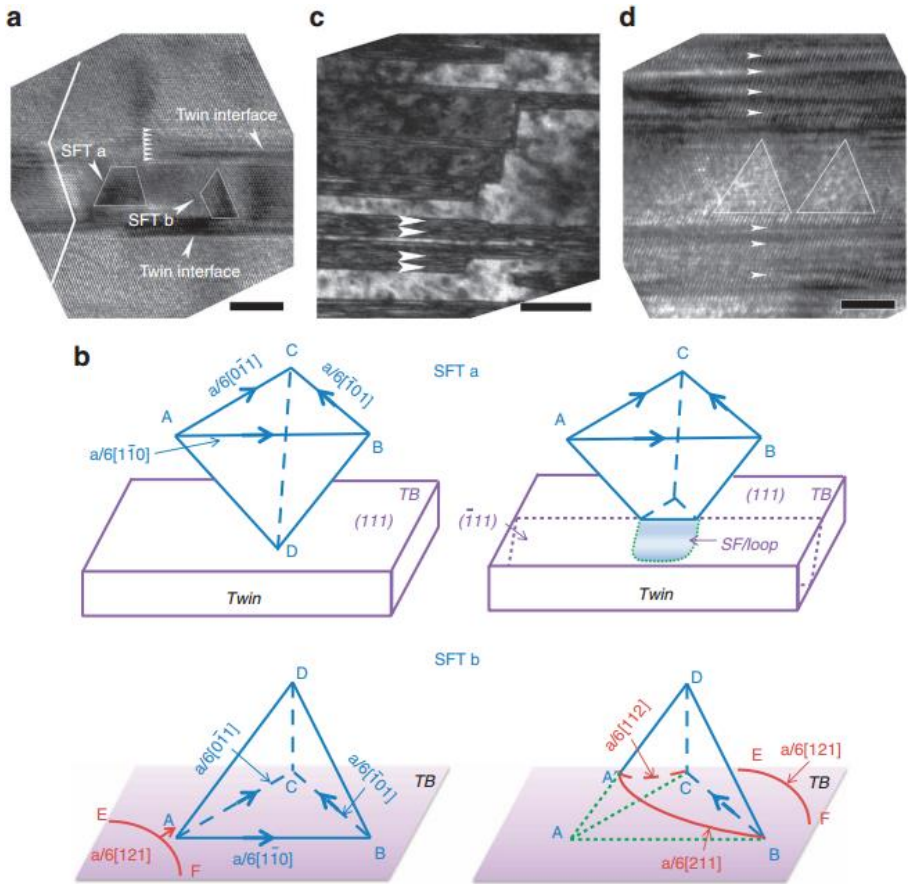

Figure 16 | High-resolution TEM of SFTs and their interaction mechanism with twin boundaries. (a) HRTEM image of two truncated SFTs during their interactions with CTBs. SFT-a was truncated from its apex, whereas SFT-b was destructed from its base. Scale bar, 4 nm. (b) Schematics of two types of interactions between SFTs and twin boundaries corresponding to the two cases in (a). (c) Stacking faults along twin boundaries in irradiated nt Ag (tave¼8 nm) were induced by SFT–twin boundary interactions as shown by XTEM micrograph. Scale bar, 40 nm. (d) HRTEM micrograph showing the formation of groups of stacking faults in irradiated thin nt Ag (up to 1 dpa). Scale bar, 4 nm.[92]

I.3.2 Stacking Faults Strengthening

As previously mentioned, grain boundaries, multilayer composites and twin boundaries are follows classical Hall-Petch relationship when grain size/layer thickness/twin spacing is larger than 50 nm. For stacking fault strengthening, recent studies proposed that yield strength may follow a linear relation as a function of stacking fault spacing [90, 93].

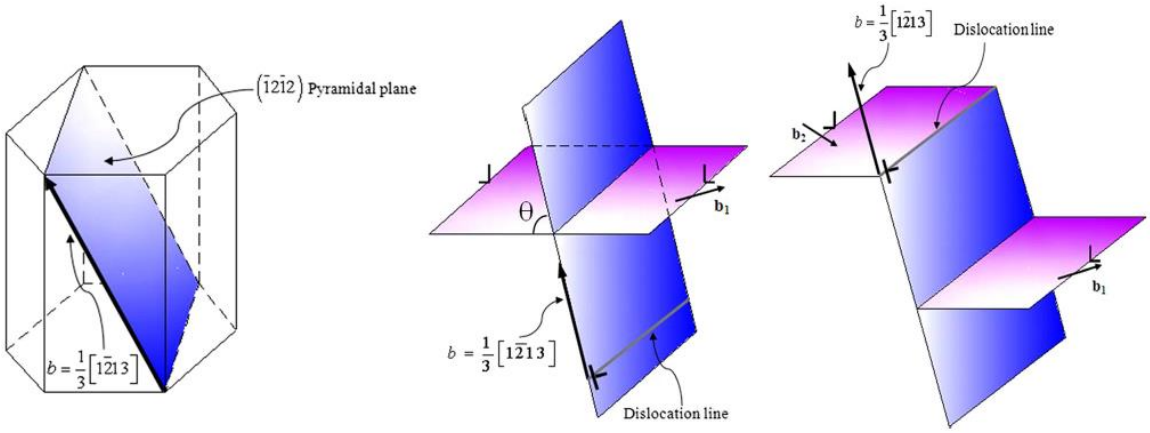

Figure 17 Schematic illustration of (a) pyramidal dislocation (b) pyramidal dislocation motion and interaction with a basal stacking fault, and (c) pyramidal dislocation cutting through the stacking fault [90].

Fig. 17 shows a schematic of pyramidal dislocation interaction with stacking faults on the Basel plane in a HCP metal. During the dislocation cutting process, the extra energy that is applied on dislocation movement is equal to the extra energy consumed by cutting the stacking faults. This can be expressed as

Equation 9 $$\boldsymbol{\Delta\tau x = \frac{xE_s}{d/sin\theta}}$$

where τ is the applied shear stress, x is the dislocation of dislocation movement, E_s is the energy consumed to cutting through the stacking faults. The shear stress can be then

expressed as a function of grain size ($1/d$). Thus, the yield strength as a function of grain sizes is shown as

$$\text{Equation 10} \quad \boldsymbol{\sigma = \sigma_a + k/d}$$

where $k=E_s\, sin\theta$ is the constant. Compared to Hall-Petch relation, the yield strength in this equation is dependent on d^{-1} instead of $d^{-1/2}$.

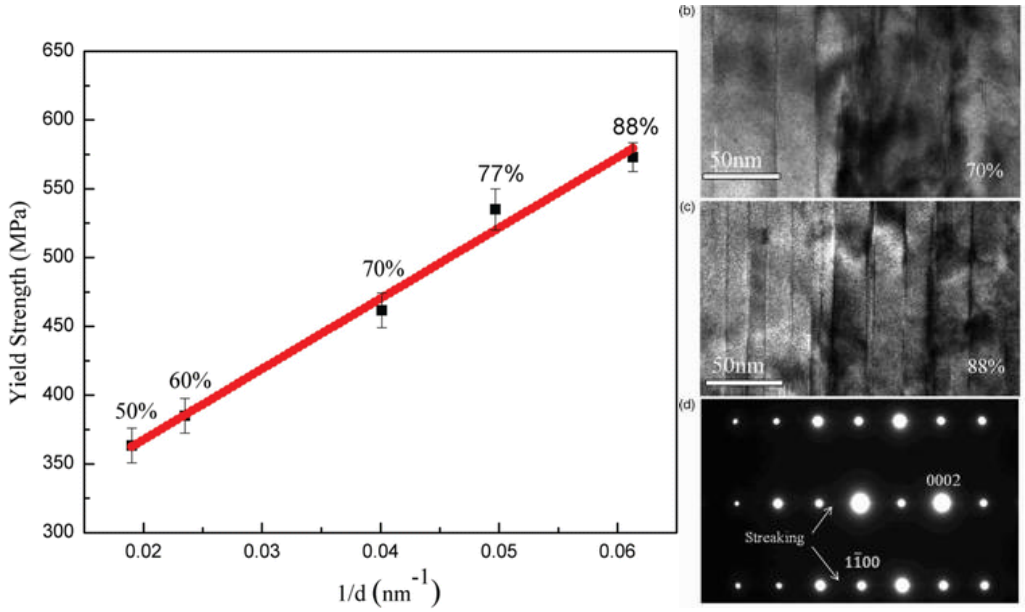

Figure 18 (a) Yield strength vs the reciprocal of the mean spacing between SFs of rolled Mg with different thickness reduction. (b-c) Bright field TEM images show the example of stacking fault spacing when thickness reduction at 70% and 88%, respectively. (d) SAD of the Mg sample shows the basel (0002) type stacking faults [93].

Fig. 18 presents the experimental observation of the yield strength as a function of d^{-1} instead of $d^{-1/2}$ in Hall-Petch relation. However, it is worth noting that the material system in these studies is single-crystal HCP Mg. The deformation mechanisms of the HCP metal, such as pyramidal slip, prismatic slip, or basel slip may play important roles during dislocation interactions. Therefore, further evidence is needed to study on stacking fault strengthening with different stacking fault spacing in various crystals.

In this section, a stacking fault is proposed as another low energy internal boundary. It can be formed by thin film growth, severe deformation or ion-irradiation. The yield strength may be dependent on d^{-1} instead of $d^{-1/2}$ (Hall-Petch relation).

I.4 Epitaxial Thin Films

Epitaxy refers to the deposition of a crystalline layer on a crystalline substrate, where the deposited layer follows or mimics the lattice arrangement of the substrate. This deposited thin film is so-called epitaxial thin film, which may be grown from majority gaseous precursors by various physical vapor deposition or chemical vapor deposition techniques. If an epitaxial thin film is deposited on a substrate of the same composition, the process is called homoepitaxy. In the semiconductor industry, the homoepitaxial growth of Si film on Si substrate is almost one of the first steps in transistor fabrication, in order to ensure the desired Si properties. Heteroepitaxy otherwise, refers to the deposited epitaxial films are different materials with substrates. Fig. 19 gives an example of a heteroepitaxial growth of TaN/TiN thin film on Si (100) substrate [94]. In this case, TiN is grown epitaxially on Si substrate. Then TaN is grown on top of the TiN seed layer as the next heteroepitaxial layers. Misfit dislocations that marked in Fig. 19(c) typically exist in heteroepitaxial films due to the lattice parameter differences between the film and the substrate.

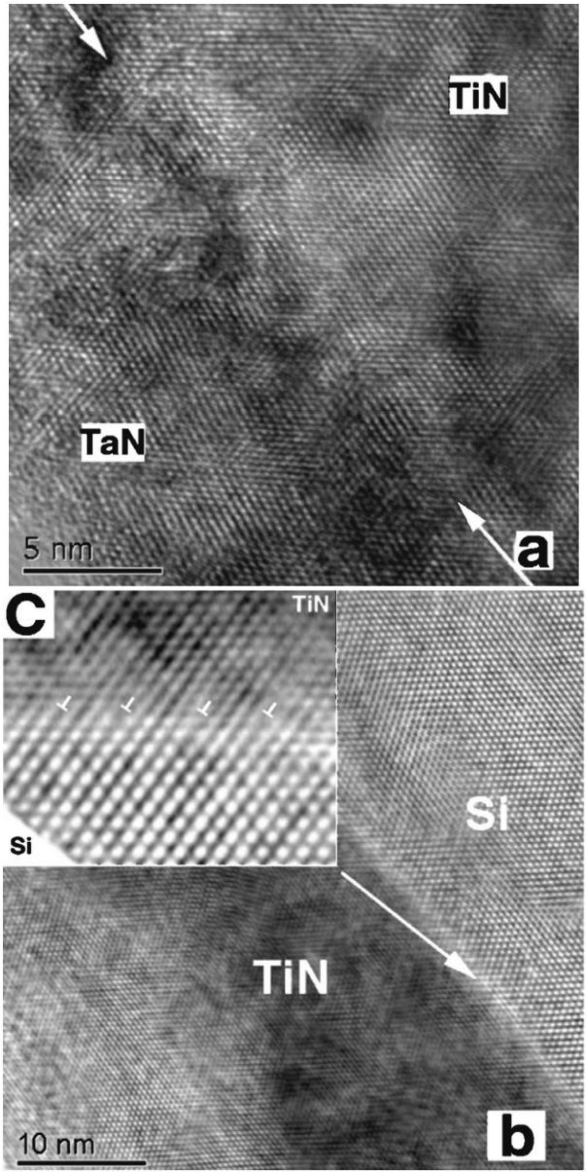

Figure 19 High-resolution cross-section bright field images at the interface of (a) epitaxial TaN/TiN; and (b) epitaxial TiN/Si substrate. The magnified (c) marked the misfit dislocation at the TiN/Si interfaces [94]

Heteroepitaxial films have various advantages on electrical and optoelectronic performance, because large amount of detrimental grain boundaries can be successfully prevented. For mechanical properties, epitaxial film is clearly needed when exploring the strengthening mechanisms of certain types of interfaces, including twin boundaries and

stacking faults. A first important concept that characterizes heteroepitaxial is mismatch strain (or misfit strain) at substrate-film interface, *f*, which is defined as

$$\text{Equation 11} \quad \boldsymbol{f = \frac{a_s - a_f}{\frac{1}{2}(a_s + a_f)}}$$

where a_s and a_f are lattice parameter of substrate and film, respectively. This mismatch strain that is generated between a substrate and film exists in nearly all of the heteroepitaxial film, because of the lattice parameter differences. During the epitaxial film deposition, mismatch strain is first accommodated by forming fully coherent interface, so-called coherency strain. At certain critical film thickness, misfit dislocations start to form in order to partially or fully relax (or reduce) the elastic strain [41, 42]. The total elastic energy (E_{tot}), can be calculated by combining the coherency strain energy and misfit dislocation energy by using [42]

$$\text{Equation 12} \quad \boldsymbol{E_{tot} = \varepsilon_c^2 B h + \frac{\mu_f b}{2\pi(1-v)}(f - \varepsilon_c)\left[ln\left(\frac{h}{b}\right) + 1\right]}$$

where ε_c is the coherency strain, *b* is Burgers vector. *B* is biaxial modulus, which equals to$\frac{2\mu_f(1+v)}{1-v}$. The critical layer thickness, h_c, can be calculated after$\frac{dE_{tot}}{d\varepsilon_c} = 0$, and it is given by

$$\text{Equation 13} \quad \boldsymbol{h_c = \frac{b}{8\pi(1+v)f}\left[ln\left(\frac{h_c}{b}\right) + 1\right]}$$

where h_c is determined when misfit dislocation can fully relax the coherent strain.

It is worth noting that beside misfit dislocations, misfit twins may form to relax elastic strain in epitaxial films systems such as Si/Ge, Ga/As, Au/Ni, and Pd/Ni [95-99]. In this case the misfit strain is relaxed by twinning partial dislocations instead of perfect dislocations. In order to reduce the mismatch strain, these misfit twin boundaries typically form inclined to the interface in the epitaxial film only. As shown in Fig. 20,

misfit twins can be successfully introduced in one of the high stacking fault energy metals, Pd, on Ni substrate.

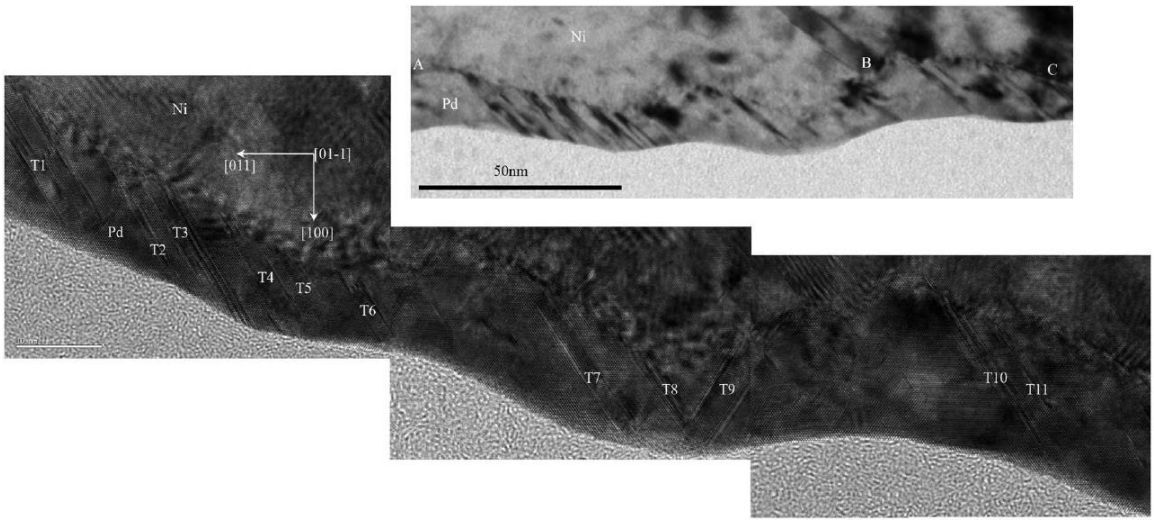

Figure 20 Cross-section bright field high resolution TEM images of a Pd epitaxial film electrodeposited on a Ni substrate. High density of misfit twins is observed [99].

In this section, the parameters on determining epitaxial thin film growth are overviewed. During heteroepitaxial growth, mismatch strain can be relaxed at certain critical film thickness by forming misfit dislocations or misfit twins.

I.5 Strain-Rate Sensitivity

As discussed previously, nanocrystalline generally exhibit substantially higher strength and much lower tensile ductility than their polycrystalline counterparts. Since the strength, hardness, and ductility of metal and alloys are strongly dependent upon their micro-nano scale structure characteristics under plastic deformation, the valuation of strain-rate sensitivity in nanocrystalline, nanotwin, or multilayer composites become a significant factor to understand the deformation mechanisms. This section will introduce

the definition of strain-rate sensitivity index, and the deformation physics behind this index.

Strain-rate sensitivity index and activation volume refer to the thermally activated mechanisms contributing to plastic deformation processes in metals and alloys. The activation volume is broadly defined as the rate of decrease of activation enthalpy with respect to flow stress at fixed temperature. The origin of strain-rate sensitivity index is a special case of inverse of stress exponent for creep.

Creep in metals is a thermally activated process which is governed by diffusion: vacancies diffuse into the material and enable dislocations to move more freely and overcome obstacles to motion. Thus, modeling the relationship between the plastic stresses sustained in creep (σ) and the steady-state strain rate ($\dot{\varepsilon}_c$) requires an Arrhenius form. One equation for modeling creep in metals is

$$\text{Equation 14} \quad \dot{\boldsymbol{\varepsilon}}_{\boldsymbol{c}} = \boldsymbol{B}\,\mathbf{exp}\left(-\frac{\boldsymbol{Q_c}}{\boldsymbol{kT}}\right)\boldsymbol{\sigma}^{\boldsymbol{n}}$$

where B is the base strain rate (a constant governed primarily by the microstructure), Q_c is the activation energy for creep, k is the Boltzmann constant, T is the absolute temperature, and n is the stress exponent for creep. In creep literature, Equation 14 is called the "Dorn" model, after John E. Dorn who proposed and developed the form in his foundational work on creep throughout the 1960's [100, 101].

In order to fully describe the creep behavior of a particular material with the Dorn model, the values of three constitutive constants must be determined: B, Q_c, and n. Taking the natural logarithm of both sides of Equation 14 yields

$$\text{Equation 15} \quad \mathbf{ln}(\dot{\boldsymbol{\varepsilon}}_{\boldsymbol{c}}) = \mathbf{ln}(\boldsymbol{B}) - \frac{\boldsymbol{Q}}{\boldsymbol{kT}} + \boldsymbol{n}\,\mathbf{ln}(\boldsymbol{\sigma})$$

which makes it clear that if temperature is held constant and strain rate is varied, then the stress exponent, n, can be determined as the slope of ln ($\dot{\varepsilon}_c$) with respect to ln (σ). Likewise, if stress is invariant, then the slope of ln ($\dot{\varepsilon}_c$) vs. ($1/T$) is equal to $-Q/k$ which leads directly to a value for Q. Finally, if both Q and n are known for a particular material, then the experimental determination of B is straightforward. Of these three constants, the stress exponent n is the simplest to determine experimentally, because the required testing is conducted at a constant temperature - often room temperature. Determination of the activation energy Q requires testing at multiple temperatures, and the determination of B can be determined by n and Q.

Thus, the stress exponent, n, is the starting point for creep characterization, not only because it is the simplest constitutive parameter to determine, but also because it conveys much information about the creep capacity of the material. At a constant temperature, Equation 14 simplifies to

$$\text{Equation 16} \quad \dot{\boldsymbol{\varepsilon}}_{\boldsymbol{c}} = \boldsymbol{C}\boldsymbol{\sigma}^{\boldsymbol{n}}$$

where C is a constant that incorporates both the base strain rate and the Arrhenius form. The theoretical lower bound for n is 1, which expresses Newtonian viscous flow (stress proportional to strain rate). There is no theoretical upper bound for n; larger values of n manifest better resistance to creep.

The *inverse* of the stress exponent is called the strain-rate sensitivity (SRS). Expression of the strain-rate sensitivity is often preferred to expression of the stress exponent, because strain-rate sensitivity is theoretically bounded and lends itself more easily to a conceptual understanding of creep. Raising both sides of Equation 16 to the power of ($1/n$) and rearranging to solve for stress yields

$$\text{Equation 17} \quad \boldsymbol{\sigma} = \boldsymbol{D}\dot{\boldsymbol{\varepsilon}}_{\boldsymbol{c}}^{\boldsymbol{m}}$$

where D is a constant and m is the strain-rate sensitivity ($m = 1/n$). Theoretically, the strain-rate sensitivity must have a value between 0 and 1, with larger values manifesting greater creep capacity. At the lower limit ($m = 0$), the right-hand side of Equation 17 is simply the constant D which means that the stress sustained does not depend at all on the rate at which the material is deformed—the material is just as strong at very low strain rates as it is at very high strain rates. For example, the strain-rate sensitivity for sapphire is nearly zero, indicating that it has almost no capacity for creep. At the upper limit ($m = 1$), the right-hand side of Equation 17 expresses Newtonian viscous flow, wherein stress is proportional to strain rate. At a constant temperature, m is simply the slope of ln (σ) with respect to ln ($\dot{\varepsilon}_c$) (Equation 15).

If modified Equation 15, the strain-rate sensitivity, m, can be expressed as

Equation 18 $$\boldsymbol{m = \frac{\sqrt{3}kT}{\sigma v^*}}$$

where $\boldsymbol{v}^*$ is activation volume. Thus, larger strain-rate sensitivity leads to smaller activation volume, which decreases the rate of decrease of activation enthalpy with respect to flow stress at fixed temperature.

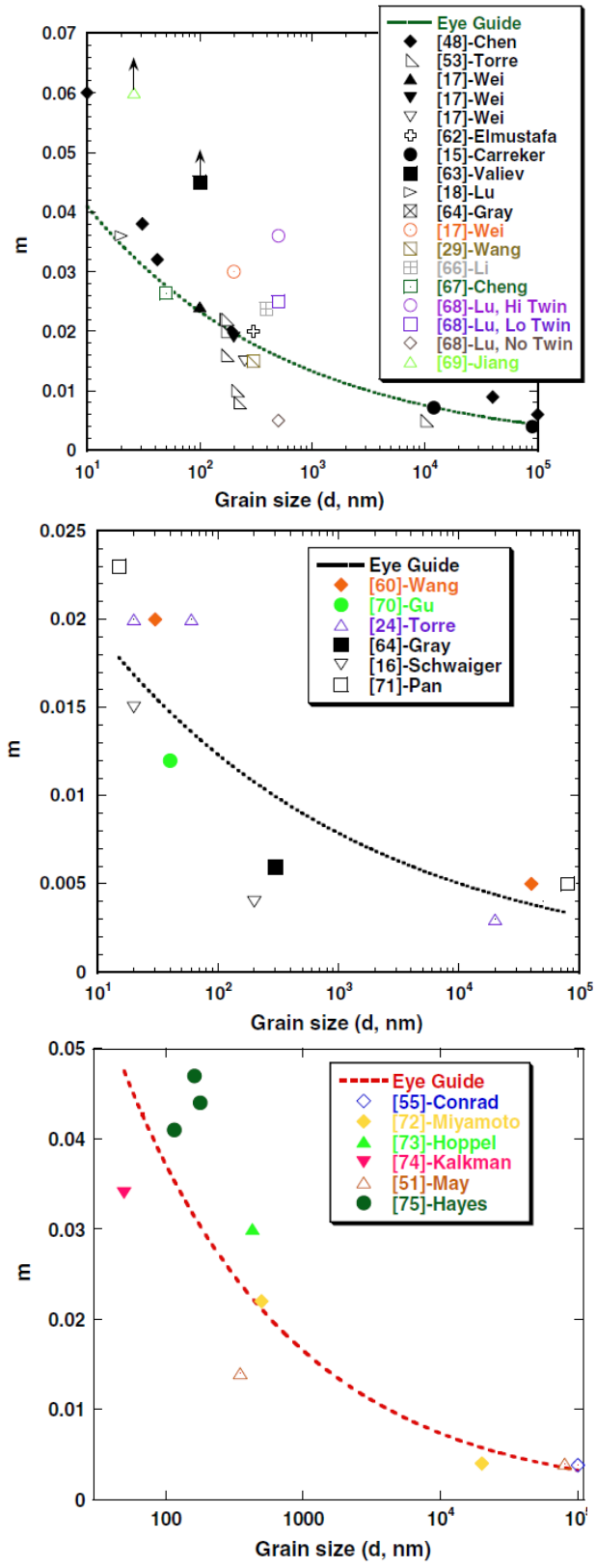

Figure 21 Strain-rate sensitivity, *m*, of (a) Cu, (b) Ni and (c) Al as a function of grain size [102]

The dependence of m values on grain size in nanocrytalline draws great attention. As shown in Fig. 21. For monolithic metals with FCC structure, such as Cu, Ni, Al, the m value is typically found to increase with decreasing grain sizes, whereas the opposite holds true for metals with bcc structure as shown in Fig. 22. The differences of the deformation mechanisms between FCC and BCC nanocrystalline may be the major reasons.

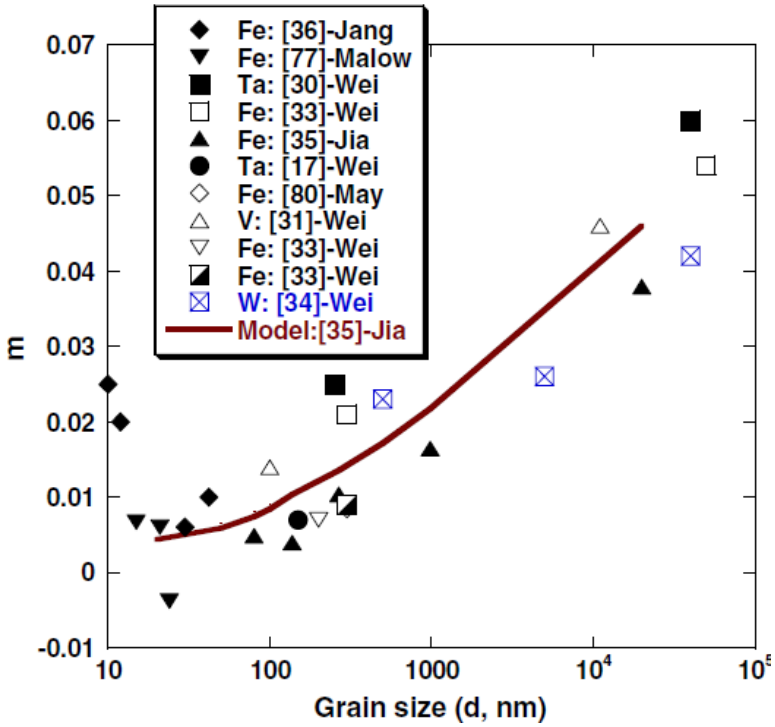

Figure 22 Strain-rate sensitivity, m, of various BCC metals as a function of grain size[102]

In FCC nanocrystalline, the activation volume v^* can be described by

$$\boldsymbol{v}^* = \boldsymbol{b} \cdot \boldsymbol{\xi} \cdot \boldsymbol{l}^* \quad \text{Equation 19}$$

where l^* is the length of dislocation segment involved in thermal activation. $\boldsymbol{\xi}$ is the distance swept out by the glide dislocation during one activation event. If Equation 19 is substituted into Equation 18, m is shown as

Equation 20 $$m = \frac{kT}{\tau \cdot l^* \cdot \xi \cdot b}$$

where flow stress τ is ($\sigma/\sqrt{3}$). If we consider this flow stress follows Hall-Pech relation, and l^* is proportional to grain size d, m can be rewritten as

Equation 21 $$m = \frac{kT}{\xi b} \cdot \frac{1}{\chi(\alpha \mu b \sqrt{\rho} d) + \beta \sqrt{d}}$$

where α, χ, β are constants. Equation 21 suggests that when the grain size is refined into the nanocrystalline regime, SRS should increase with reduced grain size. It can serve as at least a qualitative explanation for the grain size dependence of SRS of FCC metals.

For BCC metals, the activation volume maintain constant when the stress is increased to a moderate level. This phenomenon can be readily understood by appealing to the double-kink nucleation process as the rate-controlling mechanism for BCC metals at low homologous temperatures [103, 104]. Reduction in grain size is equivalent to increasing the flow stress or yield strength according to the Hall–Petch relation. The critical length of the double kink, or the spread width between the two kinks would be ~ 1.0 μm. Below this, the activation volume decreases with stress slowly. However, the stress is still following the Hall–Petch relation. Therefore, m can be described as

Equation 22 $$m = \frac{kT}{(\tau_0 + k d^{-1/2}) v^*}$$

when considering Hall-Petch relation on the stress. Therefore, if activation volume keeps the same, SRS should decrease with reducing grain size for BCC metals. It is worth noting that no clear trend are seen in HCP metal as a function of grain sizes.

In this section, the strain-rate sensitivity is overviewed on its role in plastic deformation, and grain size dependence. This index is closed related to the activation volume, which has direct connection with structure characteristics under plastic

deformation. This may help better understanding the deformation mechanisms of various interfaces with nanoscale spacing.

I.6 *In Situ* Nanoindentation

In situ nanoindentation refers to the observation in microstructural evolution during the mechanical test with nanoindentation under TEM column. The real time observation allows more reliable study with great correlation between variation of the mechanical properties and structural response. Since the last decade, several *in situ* TEM characterization methods have been introduced [105-110]. For example, *in situ* TEM heating that characterizes the microstructural evolution during heating process; *in situ* TEM straining that observes the structural response during straining process; *in situ* scanning tunneling microscopy that explores the microstructural evolution when applying electrical potential in TEM. Among them, *in situ* nanoindentation is a great technique that balances both microstructure characterization and mechanical properties [111].

Conventional nanoindentation technique has been developed in the mid of 1970s, this method is mainly used to measure the mechanical properties of small volume of materials such as hardness, stiffness and young's modulus. The details of working principle will discuss in detail in experimental section. The limitation of this technique is small correlation between microstructure and mechanical properties. However, in spite of such enormous efforts, direct observation of the deformation events during the microstructural evolution under indentation has still been desirable. Therefore, *in situ* TEM nanoindentation has become one of widely used system to explore microstructural evolution during the deformation under real time observation.

For *in situ* TEM nanoindentation, diamond nanoindenter tip, indenter sensor and piezoelectric motion controller are equipped in conventional TEM holder. Under the TEM column, indentation can be conducted with fine motion of TEM specimen, approaching to the nanoindenter tip. More potentially, during the indentation, the indenter sensor can detect the pressure sensed by tip and generate the force-displacement plot just like the conventional *ex situ* nanoindentation system. Therefore, it can provide chance of more quantitative study.

Table 2 Recent research progress with *in situ* TEM nanoindentation on metals

Materials		Reference
Nanocrystalline Al thin film	Grain rotation and coarsening, grain boundary migration and grain growth	[112]
Polycrystalline Al	Theoretical strength of defect-free lattice	[113]
Nanocrystalline Ni pillar	Dislocation annihilation under stress	[114]
Bulk Ni with a twin boundary	Direct observation of the dislocation Lomer-Cottrell lock on the twin boundary	[115]
Nanotwined Cu thin film	Dislocation multiplication at Twin boundary (TB); incoherent TB migration	[53, 54]
Fe-0.4wt%C Martensitic steel	Grain boundary deformations at low and high angle grain boundaries	[116]
Irradiated Cu pillar	Size independent strengths in irradiated Cu	[117]
Al-Mg alloy	Minor Mg strengthening grain boundary	[118]
Al/Nb multilayer	Dislocation glide at layer interfaces	[119]

With such novel technique, lately several research studies have demonstrated impressive property-structure correlations of nanomaterials with *in situ* TEM nanoindentation. Table 2 summarizes the results from recent researches on various nano-poly crystalline metals characterized with *in situ* nanoindentation. For a metal, most of the microstructural evolution involving dislocation-boundary interaction, such as dislocation pil-up, cross-slip, twinning or detwinning etc.

Since E. Stach reported the development of an *in situ* nanoindentation in TEM on 2001, tremendous studies have been conducted. Jin et al. has demonstrated that the different deformation behaviors of Al thin film depending on the size of grains during the *in situ* TEM nanoindentation [112]. As shown in Fig. 23, when the grain size is on submicrometer range, grain boundary migration and grain coalescence have been observed, which is mainly driven by dislocation interaction at the grain boundary. Meanwhile, nanocrystalline Al thin film shows rapid change of deformation behavior with grain growth and grain rotation. Similarly, Ohmura et al. also observed grain boundary and dislocation interactions during *in situ* TEM nanoindentation on martensitic steel [116]. Furthermore, Soer et al studied the effects of solute Mg on grain boundary and dislocation dynamics during nanoindentation on Al[118].

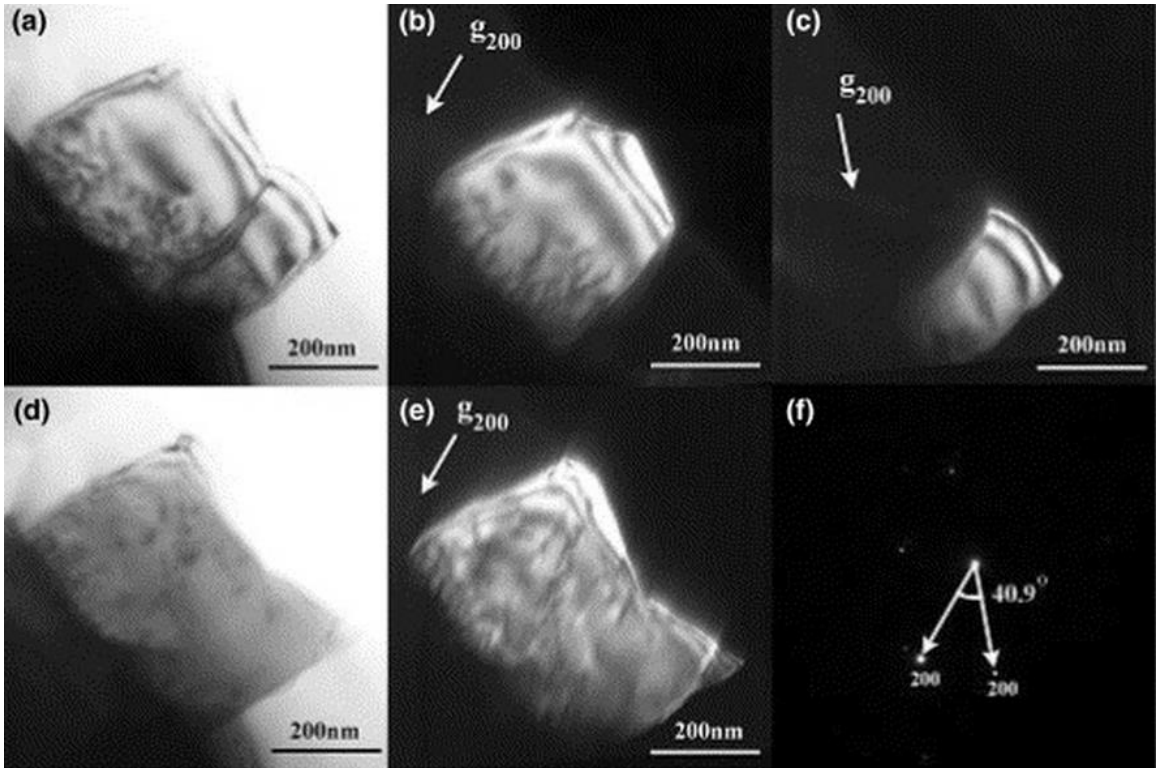

Figure 23 (a) Bright-field image before the indentation; (b) dark-field image of the larger grain before the indentation; (c) dark-field images of the smaller grain before the indentation; (d) bright-field image after the indentation; (e) dark-field image of the larger grain after the indentation, showing the larger grain grew by eliminating the smaller grain; (f) diffraction pattern before the indentation, showing the high angle grain boundary between the two grains [112].

Besides the *in situ* mechanical tests on thin film and bulk materials, Shan et al. demonstrated the strain hardening based on annihilation of dislocation in one dimensional single crystal nickel (Ni) pillar [114]. Minor et al., explored the theoretical strength of an ideal defect-free lattice by performing indentation on single crystalline Al pillar [113]. Kiener and his coworkers also compared the non-irradiated and irradiated single crystal Cu at various pillar size, where irradiated Cu shows size independent strengths [117]. Fig. 24 presents their studies on dislocation emission along with load drop during indentation on irradiated Cu.

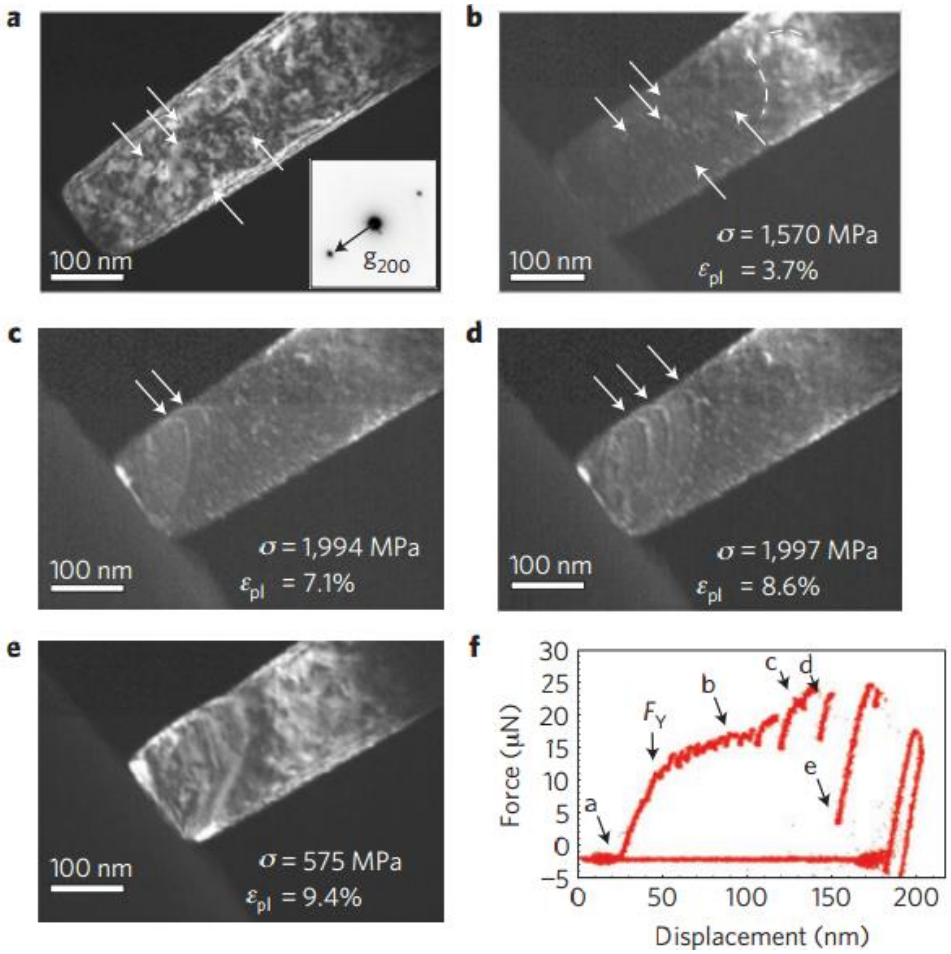

Figure 24 *In situ*TEM compression test of a (100)-oriented 118 nm diameter copper pillar irradiated to 0.8 dpa. Dark-field still images extracted from the video are shown in a–e with the measured load–displacement data in f. **a**, Before contact to the diamond punch, the pillar contains a high density of defects. **b**, After yield, deformation and hardening are governed by the bowing and exit of short dislocations, evidenced by gentle load drops in f. In **c** and **d** dislocations emitted from a spiral dislocation source extend across a slip plane and lead to significant load drops evident in f. **e**, The slip produced by this dislocation source operation leads to the formation of a large slip step, to which further deformation is confined [117].

There are several great studies on exploring dislocation-boundary interactions, such as dislocation-twin interaction, dislocation-interface interaction. Lee et al., have found the formation of Lomer-Cottrell lock when partial dislocations interacted with twin boundaries in polycrystalline Ni [115]. Fig. 25 shows the formation of the Lomer-Cottrell

at on-site of yielding and L-C lock-twin interaction after yielding. Additionally, Li et al. shows deformation behavior of thin film during the *in situ* nanoindentation with atomic resolution [53, 54, 119]. One of the novelties of these series work is observation of the dislocation under high resolution TEM. The interactions of dislocation-twin boundaries or dislocation-layer interfaces are studied in detail. For example, dislocation glide has been seen during dislocation-layer interface interaction in Al/Nb multilayer composites, as shown in Fig. 26. Moreover, dislocation multiplications are found when they interact with coherent twin boundary as shown in Fig. 27. The multiplication steps involves: 1) A lattice dislocation glides toward the twin boundary under stress applied during the indentation. 2) As the lattice dislocation going through the boundary, it can be dissociated into a sessile partial dislocation and mobile twin dislocation. 3) As the twin dislocation gliding along the twin boundary, lattices can be rearranged and finally, twin boundary could be migrated. 4) Then as the sessile dislocation dissociated into another full dislocation and twin dislocation, the deformation procedure could be repeated.

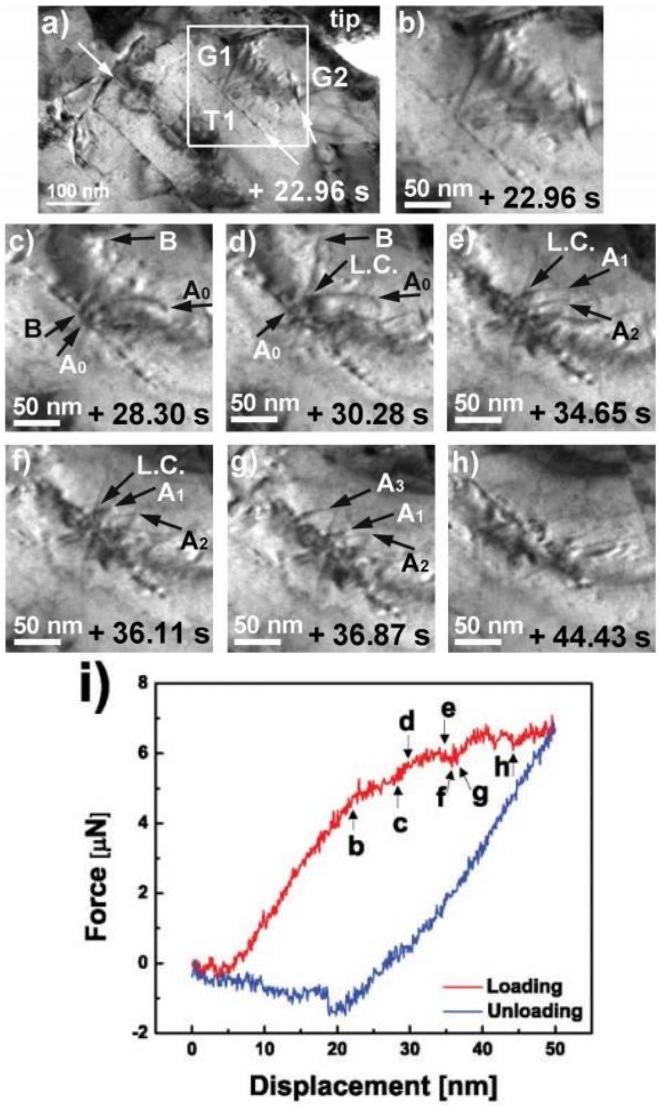

Figure 25 During the first indentation cycle, evident activity of dislocations (mainly screw or mixed dislocations) at the twin boundary was observed with formation of L-C lock (a) A snapshot shows the area of interest marked by a white box near TB1. And the enlarged series of movie frames show the interaction between dislocations and twin boundary at (b) yield point and (c-h) after yield point, with the corresponding (i) force displacement plot [115].

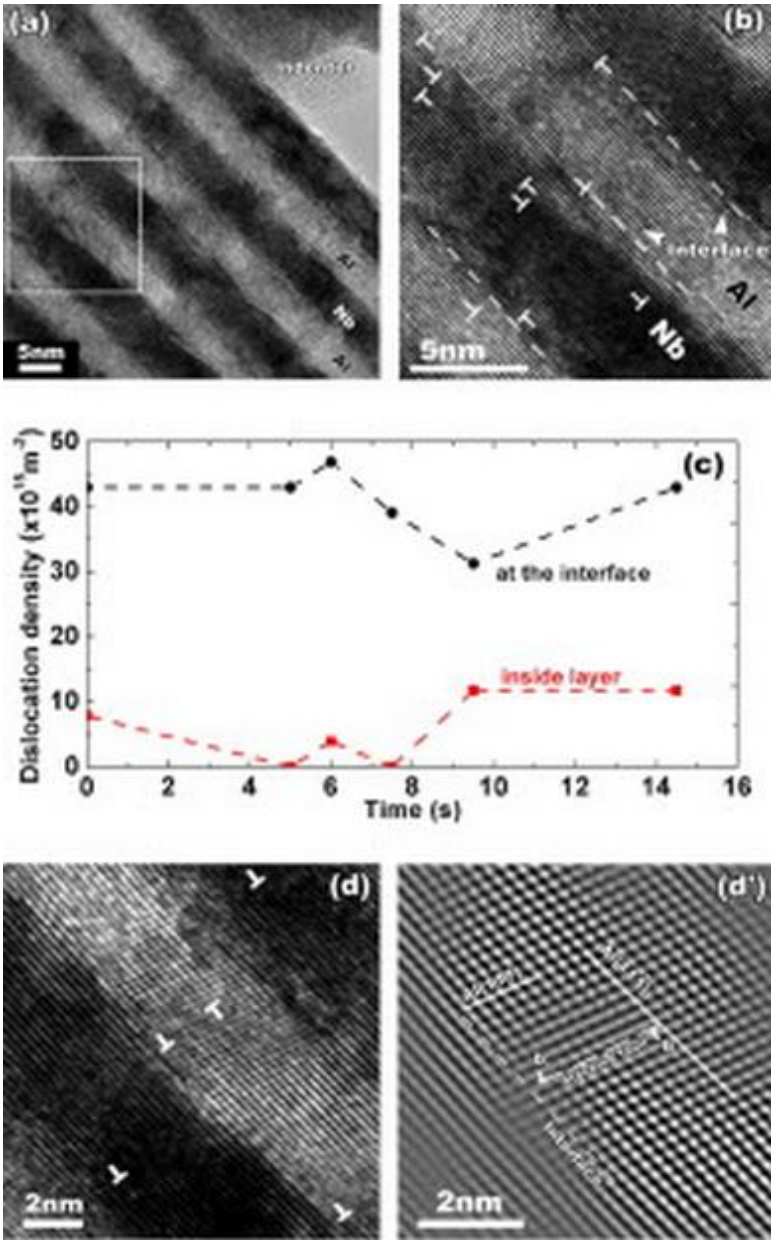

Figure 26 (a) X-TEM micrograph of the Al/Nb 5 nm film under the nanoindentor tip during the indentation experiment. (b) HR-TEM micrograph of the square box in (a) showing dislocations. Interfaces are delineated with dashed lines. (c) The evolution of dislocation densities both inside the layers and at the interfaces with time during indentation. (d) HR-TEM image of a stacking fault inside the Al layer and (d') the corresponding processed HR-TEM image at higher magnification. The stacking fault is bounded by a leading and trailing partial, labeled b_L and b_T. The trailing partial resides at the interface [119].

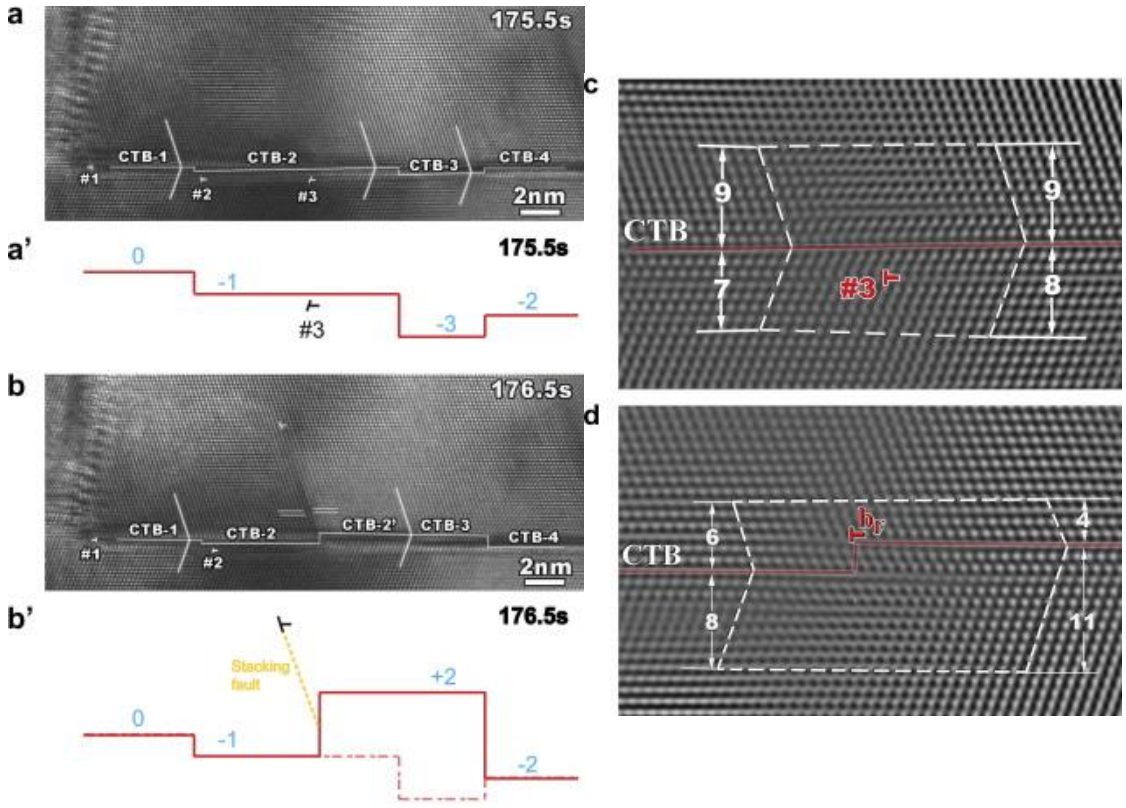

Figure 27 Interaction of lattice glide dislocation with a CTB. (a and b) HRTEM snapshots from *in situ* indentation showing the interaction of a lattice glide dislocation with the CTB. Dislocations 1 and 2 experienced no apparent displacement during the interaction process. Under applied stress the lattice dislocation 3 glided towards CTB-2 (a). After 1s dislocation 3 entered into CTB-2 (b). (a' and b') Schematic illustration of the steps on the CTB before and after the reaction. (c) A magnified inverse fast Fourier transform (IFFT) HRTEM image with Burgers circuit identifies dislocation 3 near the CTB. (d) An IFFT HRTEM snapshot taken during the multiplication process to show a sharp step with the height of three (111) interplanar distances [53].

This section reviewed recent studies on *in situ* nanoindentation, which is convinced as a powerful tool on exploring microstructural/property relation by applying mechanical test in TEM column.

I.7 Scope and Goals

The motivation of this research can divided into two major components. First is to study strengthening mechanisms of the interfaces such as twin boundaries, layer interfaces, as well as stacking faults in low stacking fault energy (SFE) metal Cobalt (Co) and Cu/Co multilayers. Second is to explore the mechanical properties including strain-rate sensitivity, and structure/property relation in nanotwinned Cu by applying advanced nanoindentation techniques, such as thermal drift controlled strain-rate sensitivity measurement and *in situ* nanoindentation under transmission electron microscope (TEM).

As mentioned previously, high density growth twins, stacking faults can be formed in low SFE metals. As one of the low SFE metals, Co has drawn little attention due to the complex coexistence of hexagonal close-packed (HCP) and face-centered cubic (FCC) structure. The scope of this study is to growth epitaxial HCP and FCC Co, respectively. Therefore, the strengthening mechanisms of these interfaces can be identified.

Cu/Co mulitilayers composites have broad applications based on their giant magnetron. This study provides two epitaxial Cu/Co multilayers systems: (100) and (111), respectively. The strengthening mechanisms at various different layer thicknesses are studied. The role of twin boundaries and stacking faults on strengthening are identified as well.

Traditional nanoindentation technique has large scattering because of thermal effect when determining the strain rate sensitivity (SRS) of materials. This study provides a new method that renders hardness insensitive to thermal drift. The new technique is

validated on nanocrystalline Ni and nanotwinned Cu films and returns expected values of SRS.

This study applied *in situ* nanoindentation to identify corresponding stress level of incoherent twin boundary (ITB) migration; dislocation nucleation; and dislocation penetration through coherent twin boundary (CTB) in one loading event on epitaxial nanotwinned Cu. We have observed the detwinning process triggered at ultra-low indentation stress level associate with stress plateau and drops before plastic yielding. The ITB migration of the thinner twin (~ 5 nm) occurs at very low stress at 0.1 GPa with about 15 nm/s velocity, whereas the thicker twin (~14 nm) can stand until 0.6 GPa. Furthermore, the dislocation nucleation and propagation before macroscopic yielding that corresponds to dislocation penetration through twin boundaries are captured

CHAPTER II

EXPERIMENTAL

II.1 Thin Films Fabrication by Magnetron Sputtering

Various thin film deposition techniques are applied in thin film research and development. Chemical vapor deposition (CVD) and physical vapor deposition (PVD) are two major categories that include most of the deposition techniques.

In a typical CVD process, reactants are transported to the deposition region. They are then absorbed on the substrate surface, where chemical reaction occurs. The deposition of byproducts is completed after the reaction. The useless byproducts are then removed from the surface by diffusion or transportation. As a basic CVD technique, Atmospheric CVD (APCVD) operates at normal atmospheric pressure and a high temperature in order to increase the deposition rate. Low pressure CVD (LPCVD) is a technique that processes at a low pressure and temperature. Reduced pressures tend to reduce unwanted gas-phase reactions and improve film uniformity. Plasma enhanced CVD (PECVD) is a CVD technique that utilizes plasma to enhance the chemical reaction rate of the precursors. It allows deposition at lower temperatures, which is significant in the manufacture of the semiconductor. These CVD techniques are popular in semiconductor industry due to their capability of a large yield of product (cheaper and higher deposition rate). One of the major drawbacks for these techniques is the thin film quality because of the difficulty of controlling chemical reactions. Some advanced CVD techniques overcome this issue, for example, atomic Layer CVD (ALCVD), also called atomic layer deposition (ALD) or Atomic layer epitaxy (ALE), is a specialized form of epitaxy growth that typically deposit alternating monolayers of two elements onto a

substrate. Metal organic CVD (MOCVD), a CVD process based on metal organic precursors, is operated under an ultra-high vacuum condition. These two techniques are widely used in semiconductor industry for device fabrication because of the high quality growth of thin films by maintaining high vacuum during deposition, which decrease deposition rate dramatically.

The PVD techniques are the other approaches that avoid any chemical reaction during deposition process. The typical PVD technique induces vapors from a source by physical excitation methods such as heating (evaporation) or ion bombardment (sputtering). Thermal and e-beam evaporation are typical evaporation methods where the target is heated by either thermos or electron beam. The atoms in the target are then stimulated and deposited on the substrate surface. The deposition rate and composition is dominated by evaporation flux. This is an equilibrium process from the heated target to the substrate but with low deposition kinetics, that is not sufficient to provide enough kinetic energy for deposition atoms to move to the perfect location, in order to form a better quality structure. Two decades ago, molecular beam epitaxy (MBE) was developed to deposit well-defined layer structure with precision at the atomic level by using an ultra-low deposition rate. However, due to ultra-low deposition rates and high cost on maintenance, MBE is less interested in current research and development. In comparison, non-equilibrium processes such as pulsed laser deposition (PLD), and magnetron sputtering have become more popular for providing high quality thin films at reasonable cost level. PLD is a PVD technique where a high power pulsed-laser beam strikes a target material inside a high vacuum chamber. The material is vaporized from the target and

then deposited on a substrate. Magnetron sputtering is a widely used method to produce high quality metal thin film with relative less cost.

In the magnetron sputtering process, the target atoms are scattered backward when the energetic particles such as accelerated ions bombard the solid target surface. This phenomenon is so-called sputtering. Surface or near-surface atoms are kinetically dislodged by the impact of the energetic particle to the target. These dislodged atoms have considerable kinetic energy by transferring from the initial particles. They move deeper into the target material and dislodge extra atoms. This knock-on process only stops when the energy in the projectile or displaced atoms is smaller than the displacement energy. The residual energy is absorbed to generate phonons and this raises the local temperature. These atoms on or near the surface may be dislodged by overcoming the surface binding energy due to enough energy transferred from the ions or other knock-on atoms, and are deposited on the substrate surface. These atoms are known as sputtered atoms and the process is called sputtering deposition.

The number of atoms (molecules) ejected from a target surface per incident ion is defined as sputtering yield, Y. The magnitude of sputtering yield depends on factors including the details of energy transfer between incident and target atoms, mass and energy of incident ion, type of discharge gas, mass and binding energy of target atom, and incident angle of the projectile. The sputter yield can be obtained either from the simulation such as SRIM in which collisions between the energetic ions and the paths are calculated by using collision potential. Normally, materials having higher melting temperature possess lower sputtering yield due to higher binding energy.

The sputter deposition is often practiced in plasma that is generated when a voltage applied across a cathode or an anode in the vacuum chamber. In most cases, the grounded chamber wall is treated as the anode, and the cathode is then biased negatively. The types of sources for sputtering deposition include direct current (DC) diodes and radio-frequency (RF) diodes. Sputter-deposition of thin films has a wide range of applications, including architectural glass, semiconductors, automobiles coatings and corrosion resistant coatings. The transverse magnetic field normal to the electric field is applied to increase the ionization efficiency of electrons by increasing their path length in the sputtering, which is so-called magnetron sputtering. During the magnetron sputtering process, secondary electrons close to the target will be trapped by a magnetic field, in order to enhance the deposition rate. The sputtered atoms are neutrally charged and so are unaffected by the magnetic trap. The working principle of the magnetron sputtering system is shown in Fig. 28.

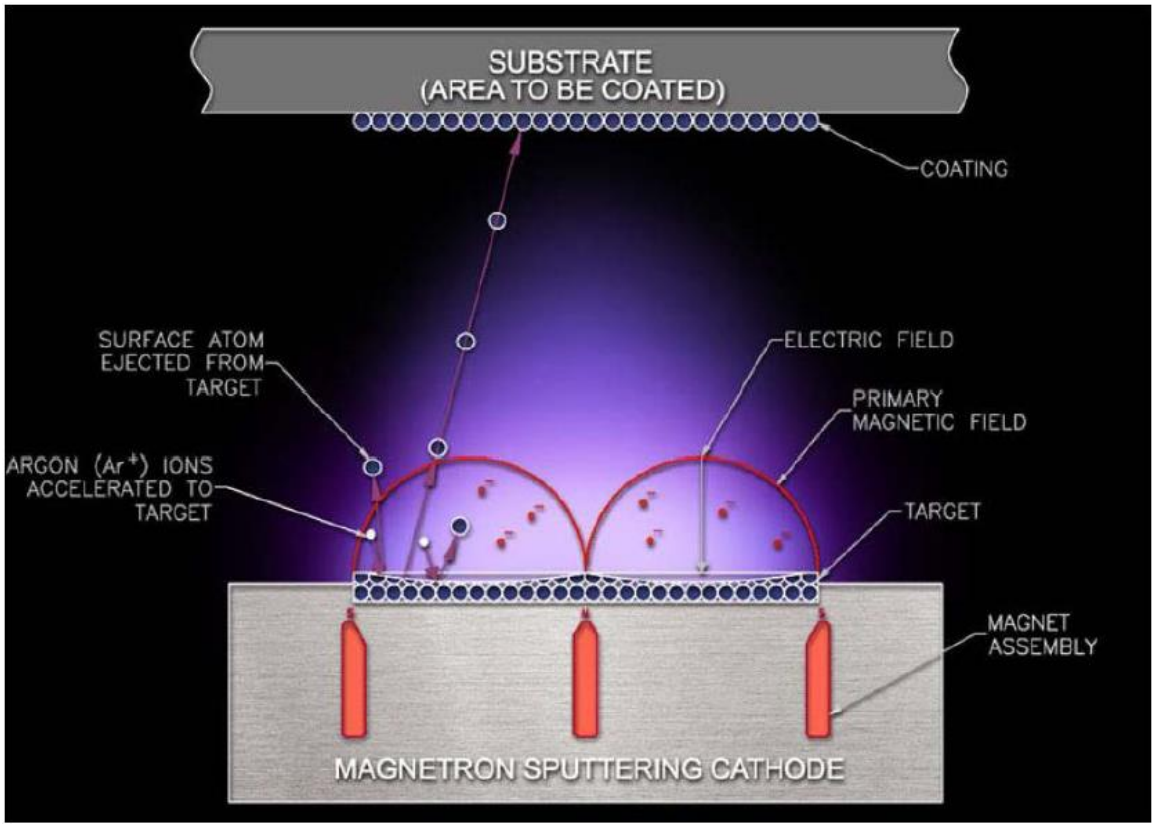

Figure 28 The working principle of the magnetron sputtering system

The advantages of magnetron sputtering are as follows: (1) There is almost no restriction on target material, including metals, semiconductors or insulators; (2) The sputtered films typically exhibit a better adhesion on the substrate than evaporated films because of the higher kinetic energy; and (3) Magnets in the magnetron enable lower pressures to be used. (4) When sputtering metals by using the DC magnetron sputtering technique, the high conductivity of metals guarantees a discharge-free sputtering of the targets.

Our research group (Zhang Nanometal Group at Texas A&M University) operates a custom-built magnetron sputtering system featured with four separate sputtering guns operating with either DC or RF power supplies. This system can reach a low base

chamber pressure 5 x 10^{-8} torr, which is sufficient to grow high-quality epitaxial films. Single crystal silicon wafers with various orientations are used as substrates throughout this work. Substrates are etched using HF acid prior to deposition to remove the oxide layer and allow epitaxial growth.

II.2 X-Ray Diffraction (XRD)

X-ray diffraction (XRD) is a non-destructive tool for the microstructure characterization. Since the magnetron sputtered thin films have a smooth surface, no sample preparation is required to apply this XRD technique. In this study, XRD was extensively utilized for the epitaxial growth characterization of as-deposited single layer or multilayer films.

In the XRD experiment, the thin films are exposed to a monochromatic beam of x-rays from a Cu-K_α source. The wavelength of these x-rays is of the same magnitude as interatomic spacing. Bragg's law [120] is usually applied to analyze the XRD results, the expression is showing as

Equation 23 $$\boldsymbol{n\lambda = 2dsin\theta}$$

where n is the order of diffraction, λ is the wavelength for the incident x-ray beam (Cu-K_α), d is the spacing between planes that contribute to diffraction, and θ is the angle between incident beam and the crystallographic plane. The schematic of the typical X-ray diffraction is shown in Fig. 29. An x-ray detector such as a Geiger counter or a scintillation counter, mounted on a movable arm, detects the diffracted beam. From the intensity and position of the diffracted beam, various interatomic spacing, crystal structure, and orientation of the thin film are determined. This is due to the periodic arrangement of atoms on specific crystallographic planes in the crystalline solid thin film.

The scattered x-rays mutually reinforce each other in certain interatomic spacing (d), where the diffracted intensity is stronger at certain corresponding angle (θ) following Bragg's law as above.

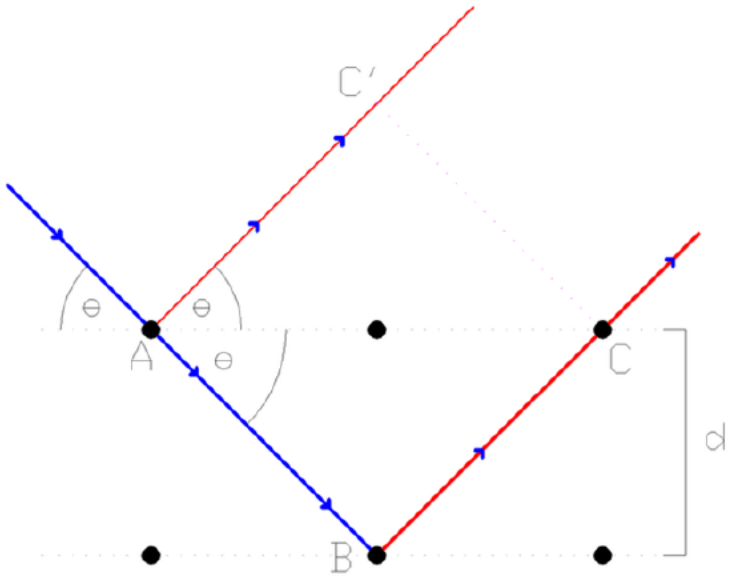

Figure 29 Schematic of the typical X-ray diffraction following to Bragg's Law

In this study, XRD was performed at the Texas A&M Department of Chemistry X-ray Diffraction Laboratory. A Bruker-AXS D8 Bragg-Brentano X-ray Diffractometer, using Cu-K_α source, can be used to collect θ-2θ scans from deposited films. Additional XRD may be performed by collaborators at the Center for Integrated Nanotechnologies, a U.S. Department of Energy and Office of Basic Energy Sciences user facility at Los Alamos National Laboratory; Texas A&M Department of Electrical Engineering Wang Thin Film Laboratory. The instruments used are PANalytical X'Pert PRO Materials Research Diffractometer, also operated using Cu-K_α radiation. This diffractometer can conduct both out-of-plane θ-2θ and in-plane phi scans.

II.3 Transmission Electron Microscopy (TEM)

Transmission electron microscopy (TEM) is critical in evaluation of microstructure, such as morphologies, textures and kinetics in sputtered single layer and multilayer films. TEM is a microscopy technique inwhich an electron beam is transmitted through an ultra-thin specimen (normally less than 100 nm). The electron beam passes through the specimen after the interaction. It magnifies and focuses on an imaging screen in order to discover the detailed structure information in the specimen. Decades ago, the images were captured by photographic films that have the best quality and most information. Nowadays, the advanced charge-coupled device (CCD) becomes more popular to capture both images and diffractions, due to the convenience and compatibility of imaging processing by using computers.

A classical TEM is composed of four major components: illumination, electromagnetic lens, sample stage, and imaging system. The illumination system provides the electron beam, which is generated by the electron source composed of a cathode and an anode. Usually a heated tungsten or LaB_6 filament emits electrons, which are then confined into a loosely focused beam by a negative cap. The positive anode accelerates the focused beam that passes through the tiny hole in the center of the anode to form a stream of monochromatic electrons. A series of condenser lenses and metal apertures are used to form one coherent electron beam. The first condenser lens determines the general spot size range that strikes the sample. The second condenser lens can adjust the size of the spot on the sample. The metal aperture, a thin disk with a small circular hole, is applied to restrict the electron beam and knock out high angle electrons

before they strike the specimen. Then the coherent beam strikes the specimen that is in the sample holder, and parts of the beam are transmitted.

The sample holder is a platform equipped with a mechanical arm for holding the specimen and controlling its position. After interaction between the electron beam and specimen, three types of transmitted electrons are collected to provide the sample information. The unscattered electrons are the incident electrons, which are transmitted through the thin specimen without any interaction with the specimen. The contrast generated by the unscattered electrons varies in terms of specimen thickness. Elastic scattered electrons are the incident electrons that are scattered in an elastic fashion without losing energy. The pattern generated by elastic scattered electrons can provide information regarding the orientation, atomic arrangements and phases because all electrons scattered by the same atomic spacing will be scattered by the same angle, which follows Bragg's Law as previously mentioned. Inelastic scattered electrons, which lose energy during the interaction, are incident electrons that interact with specimen atoms in an inelastic fashion. They can be used to acquire either electron energy loss spectroscopy (EELS) or Kirkuchi bands.

After transmitting the specimen, the electron beam is focused by the objective lens that consists of another electromagnetic lens system and a screen. In this electromagnetic lens system, the objective lens is used to re-focus the electrons after they pass through the specimen. The projective lens can enlarge the image and project it onto the screen with a phosphorescent plate. The objective aperture can enhance the contrast of the image by blocking out high-angle electrons, and the projective aperture offers several functions to examine the periodic diffraction of electrons.

Selected area diffraction (SAD) is determined by intermediate lens aperture size when parallel electrons are transmitted through a small area of the thin foil specimen. These electrons are diffracted according to Bragg's law. The SAD patterns of polycrystalline or nanocrystalline materials are composed of a transmitted beam and a number of rings. These patterns can explore the information on the periodicities in the lattice, and hence the atomic positions, such as amorphous or crystalline, crystallographic features, orientation relationship of the interface, etc.

Another type of TEM is a scanning transmission electron microscope (STEM). The electron beam is focused into a narrow spot which is scanned over the sample when the electrons pass through the specimen. The contrast of different materials in STEM is directly related to their atomic numbers. STEM is typically accompanied by chemical analysis techniques, such as mapping by energy dispersive X-ray (EDX) spectroscopy, electron energy loss spectroscopy (EELS), and annular dark field imaging (ADF). Images with atomic resolution can be obtained when applying a high-angle ADF detector into STEM, i

TEM and STEM were performed at the Texas A&M Microscopy and Imaging Center using several microscopes. The JEOL 2010 microscope has a LaB_6 filament and is operated at 200kV to achieve a point resolution of up to 0.23nm. Additional imaging may be performed using the FEI Tecnai G2 F20 ST. This microscope is a field emission instrument operated at 200kV. It is capable of conventional imaging, as well as high-angle annular dark field scanning transmission electron microscopy (HAADF-STEM), a technique which provides chemical composition information based on the atomic number of the investigated species.

II.4 Nanoindentation

The material's hardness indicates the resistance of a material to localized plastic deformation. The indentation hardness is normally 3 times greater than flow stress. The major advantage of using nanoindentation is to measure the mechanical properties of the thin film materials with small volume. Measuring hardness using nanoindentation involves two steps. At first, a hard indenter is pressed into the material with a certain load and the displacement is composed of elastic and plastic deformation. Secondly, during the retraction of the indenter, the elastic deformation is recovered and only the residual area, which is due to plastic deformation, can be measured. The indentation hardness (H_{IT}) is determined by equation 13 where P_{max} is the maximum applied force and A_c is the projected contact area between the indenter and the material surface. The hardness is defined by

Equation 24 $$\boldsymbol{H_{IT} = P_{max}/A_c}$$

A_c could not be measured directly. An area function, which describes the shape of the indenter tip, has to be expressed as a mathematic function relating to the contact depth of the indenter with h_c. The indentation hardness measurement is obtained from the load-displacement curve. However, they are sensitive to various analysis methods including elastic contact model [121], continuous stiffness method [122], and contact solution for spherical indenters. Among these, the analysis based on elastic contact model is the most commonly used method. It assumes: (1) deformation upon unloading is purely elastic; (2) the compliances of the samples and of the indenter tip can be combined as springs in series and (3) the contact can be modeled for contact between a rigid indenter of defined shape with a homogeneous isotropic elastic half space using the equation as shown below:

Equation 25 $$S = \frac{2E_r\sqrt{Ac}}{\sqrt{\pi}}$$

where S is the contact stiffness, and E_r is the reduced modulus.

Based on these assumptions, contact depth h_c can be expressed by

Equation 26 $$h_c = h_{max} - \varepsilon(h_{max} - h_i)$$

where h_{max} is the maximum depth of indentation, and h_i is the intercept depth of the maximum unloading indentation. The correction factor ε is a function of the shape of the indenter tip, for example, flat tip is 1, conical tip is 0.73, Berkovich tip, Vickers and spherical indenter are 0.75. Fig. 30 shows a cross-section view of an indented area with marked h_{max}, and h_i.

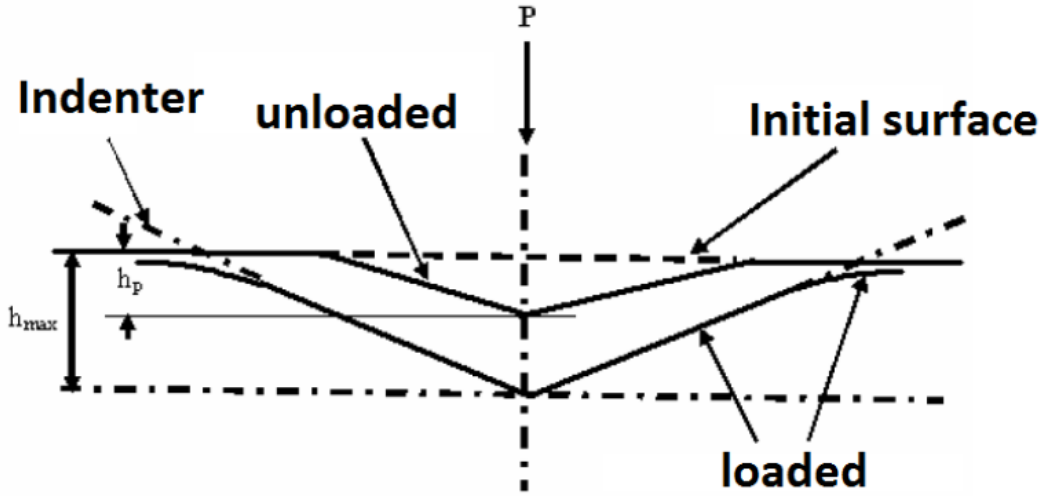

Figure 30 A cross-section view of an indented area

The procedure for data analysis to obtain indentation hardness is as follows: The slope of the tangent at P_{max} is used to obtain h_i, and h_{max} at P_{max} is acquired in the load-displacement curve. Correction factor ε is determined by the shape of the indenter tip. The contact depth h_c can be obtained by inputting h_i, h_{max} and ε. The project area A_c is a function of the indenter shape.

The elastic contact model assumes that the compliance of the samples and of the indenter tip can be combined as springs in series. Therefore,

$$\text{Equation 27} \quad \frac{1}{E_r} = \left(\frac{1-\nu_i^2}{E_i}\right) + \left(\frac{1-\nu^2}{E}\right)$$

where E_r is called reduced modulus, E_i is the modulus of indenter and E is modulus of the tested specimen, ν_i and ν are the Poisson's ratio of the indenter and the tested specimen, respectively. The reduced modulus is obtained by contact stiffness and projected area.

Hardness can be measured via an instrumented nanoindentation method performed using a Fischerscope HM2000XYp micro-/nano-indenter with a Vickers indenter tip. This instrument is operated by the Zhang Film and Nanolayer group. It is capable of providing force- or depth-controlled indentation. Additional nanoindentation may be performed by collaborators in Agilent Company. An Agilent G20 NanoIndenter with a berkvich indenter was used for all testing. The continuous stiffness measurement (CSM) option was also used in order to achieve hardness and elastic modulus as a continuous function of penetration depth. A comparison between hardness and depth analysis is typically performed, and a hardness plateau (i.e. proper depth to avoid erroneous hardening influences of both small indentation size and substrate effects) is typically observed. A minimum of 9-12 correct indentations are typically performed at each indentation depth to ensure enough data for reliable statistics.

II.5 *In Situ* Nanoindentation in TEM

Since Wall and Dahmen developed the *in situ* TEM nanoindnetation system in 1997, it has been widely used as a property/structure characterization technique. Especially for mechanical property of materials, *in situ* nanoindentation allows direct

observation of the deformation behavior during the indentation process in TEM column. Such a dynamic experiment can be achieved when a sharp diamond tip is mounted in the specimen holder and three dimensional motions of either tip or specimen are controlled by piezoelectric drivers. A pressure sensor that is equipped along the tip measures the load-displacement curve as same as the conventional nanoindentation system. Therefore, various valuable researches have been conducted on exploring materials property and microstructure relation. Among them, direct observation of dislocation activity and its correlation with grain and twin activities in the metallic system could provide clear evidence to either support or suspect the conventional theories. Additionally, discovery of new phenomenon via the *in situ* test could provide possibility for development of the advanced materials.

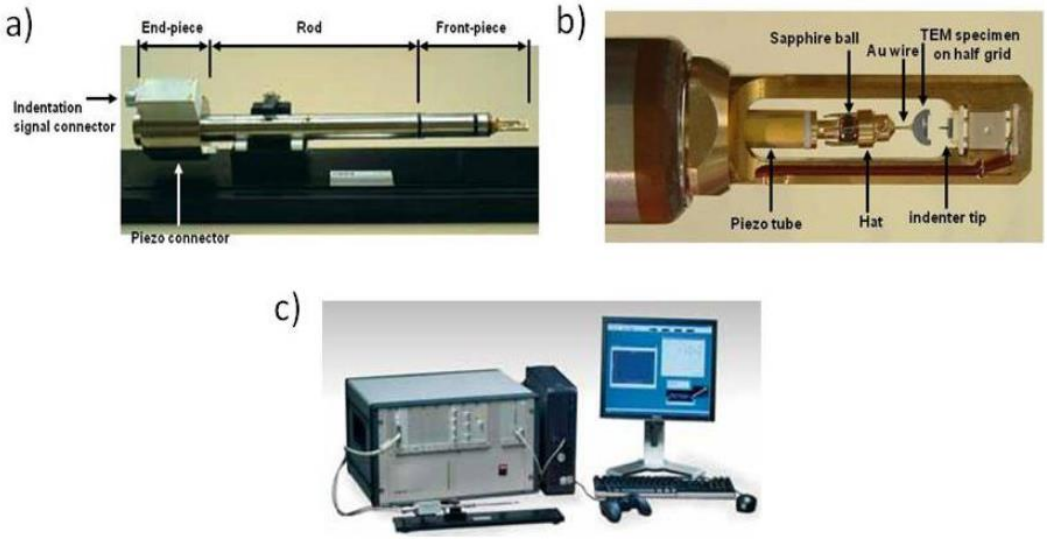

Figure 31 Two major components of *in situ* TEM nanoindentation: (a) *in situ* specimen holder, (b) The enlarged view of the front-piece of the specimen holder, and (c) control system

Our *In situ* TEM nanoindentation system is composed of two major components, *in situ* specimen holder and control system (as shown in Fig. 31). The *In situ* holder that includes TEM specimen and indenter sensor is mainly composed of three parts: a front-piece that is mainly in the TEM column, a rod and an end-piece. Unlike the conventional TEM specimen holder, the front and end pieces from the *in situ* holder require special design when considering the piezoelectric motion of the sample and indentation procedure. The TEM specimen on half grid should be mounted on the sapphire ball which is connected to piezoelectric tube for smoother motion of the specimen. The indenter sensor and tip are installed in the front area of the holder, which allows the direct contact with the specimen under the electron beam transmission in TEM. Finally, the end-piece of the holder transfers the indentation signal and piezoelectric signal to the control system.

Once the indentation process is initiated, the indenter tip is fixed while the sample moves toward the tip by a piezoelectric stage. For the movement of the sample, several parameters can be changed such as motion speed, maximum indentation depth and force, and holding time at the maximum depth. During the indentation, the loading process between the tip and specimen can be captured by a built-in CCD camera in the microscope. After the indentation, based on the data detected by the control system, force-displacement plot can be displayed on the computer.

Table 3 Calibrated *in situ* indenter parameters

Tip type	K [N/m]	P_0 [μm]	P_1 [μm]
Berkovich	450	1500±300	-5200±1500
Spherical	450	1400±300	-5500±1500
Vickers	900	3950±300	-15550±1500
Wedge	1400	2840	-5735
Punch	3400	5825	-13245

Similar to the conventional nanoindentation system, the *in situ* system also requires various kinds of indentation tips such as Berkovich, Conical and Vickers. Table 3 shows the corresponding sensor data for various tip after calibration by nanofactory instrument Inc. Unlike the conventional nanoindentation which is conducted on large dimension of surface, the *in situ* nanoindetation is conducted on very small surface area of the thin foil, which may lead to a slip between the tip and specimen. A wedge and punch shaped tips are currently widely used to ensure the better contact with the specimen. Because of the geometries differences of the tips, different parameters are required for tips' calibration.

Once the specimen and sensor of indenter tip is installed in the holder, the next step is to align between the tip and thin specimen before actually conducting the indentation. Since the *in situ* nanoindentation is conducted on the thin foil, the alignment of the specimen along the same height to the tip position is very critical. Typically, the alignment of the tip and specimen can be carried out based on adjusting their eucentric heights (z-height). The eucentric height of the tip is set by control panel in TEM, the z-

height of the specimen can be adjustable by the piezoelectric motion control from the motion control program.

Once the load-displacement curves are collected, the indentation stress can be calculated by two types of calculation methods. They are chosen when considering the real contact geometry of the indenter tips (either wedge or spherical tips as used in our *in situ* nanoindentation studies). If we estimate contact area based on wedge tip, the contact area *A* can be expressed as:

$$\text{Equation 28} \quad \boldsymbol{A \approx 2t\left[\frac{R}{\cos\left(\frac{\alpha}{2}\right)} + (D - R)\tan\left(\frac{\alpha}{2}\right)\right]}$$

$$\text{Equation 29} \quad \boldsymbol{\sigma = F/A}$$

where *D* is the indentation depth, *t* is the foil thickness, and *R* and *α* are the tip radius and angle, respectively. The indentation stress, *σ*, can be estimated by the load, *F*, divided by contact area *A*.

If we estimate projected area based on spherical tip geometry (Hertzian contact [123]), the contact radius is

$$\text{Equation 30} \quad \boldsymbol{a = \sqrt{2RD - D^2}}$$

The indentation stress can be calculated as

$$\text{Equation 31} \quad \boldsymbol{\sigma = \frac{F}{A} = \frac{F}{2at}}$$

In this study, we are using Hertzian estimation of spherical tip to calculate the indentation stress.

For instance, if the recorded load during nanoindentation is F = 1 μN, t = 30 nm, D = 30 nm, α = 70 nm; R = 100 nm, then the two methods yields $\sigma = 0.228\ GPa$ (method 1) and $\sigma = 0.233\ GPa$ (method 2). Thus, indentation stress, which

depends on the geometry of specimens and indentation depth, can be accurately determined by using both methods.

In this study, the *In situ* TEM analysis was performed on a JEOL2010 and Tecnai F20 ST analytical transmission electron microscope. Images and movies during indentation events were captured using a built-in CCD camera in the microscope. A standard *in situ* nanoindentation holder, manufactured by Nanofactory Inc., can reach a maximum load of 1000 μN and a maximum loading depth of 700 nm. For most of the experiments in the study, a maximum depth of 250 nm and a maximum load of 200 μN were set to avoid tip damage. The sharp conical-shape tip was used for performing nanoindentation on specific grains or positions in the sample. The *in situ* movies and TEM images were taken during the nanoindentation experiment. During the indentation experiment, the nanoindentation tip was stationary while the sample was driven closer to the tip by a piezoelectric stage in a precision movement as fine as 0.1 nm per step. During the loading process, a constant loading rate of 10 nm/s and a holding time of 15 ms were used for all the indentation experiments.

CHAPTER III

CONTROLLING MECHANICAL STRENGTH BY TAILORING VOLUME FRACTION OF STACKING FAULTS RIBBONS IN EPITAXIAL FCC (100) COBALT

III.1 Overview

We investigate the mechanical properties of sputtered, epitaxial Cobalt (Co) films with 1.2 μm thickness. By applying epitaxial Cu seed layer on Si substrates, epitaxial FCC (100) and HCP (0002) Co films can be achieved, respectively. High density stacking faults with an average spacing of a few nanometers are observed on (0002) Basel planes in HCP Co films. Compared to HCP Co, high density stacking faults intersecting ribbons are observed on different (111) planes. Furthermore, the volume fraction of these stacking faults intersecting ribbons in FCC Co can be controlled by deposition parameters of magnetron sputtering. The indentation hardness of the FCC Co rises from 4 to 5 GPa with increasing the volume fraction of the stacking faults. The formation and strengthening mechanisms of these stacking faults are discussed.

III.2 Introduction

As a low energy internal interfaces, twin boundaries have shown the effectiveness on blocking dislocation motion, and then contributed to the strengthening [32, 50, 69, 75]. Compared to the nanocrystalline metals, nanotwin metals show the combination of great strengthening and ductility [51, 56, 124]. There are several ways to introduce twin boundaries at room temperature. The most common is post-processed methods including severe plastic deformation, tensile deformation, and surface mechanical attrition treatment (SMAT) where large stress can be introduced [71, 85, 87-89]. Recently, high density nanotwins can be introduced by simple growth process, for example electro-deposition or physical vapor deposition [50, 78, 80]. Stacking fault energy, an intrinsic materials property, is often used to estimate the tendency to form high density growth twins in low stacking fault energy metals, such as Ag, Cu. Recently, another low energy internal interfaces, stacking faults, has shown the great strengthening as well [90, 93, 125]. The strengthening mechanisms of growth stacking faults have become an interesting topic.

Cobalt (Co) and Co-based alloys have various engineering applications based on their great wear and corrosion resistance, high mechanical strength and deformability, advanced magnetic properties, and great biomedical compatibility [126-129]. For mechanical properties, recent experimental studies showed high strength and tensile ductility in nanostructured Co, compared to polycrystalline Co [130, 131]. This might due to the effect of high density twins or stacking faults since the stacking fault energy of Co is less than 20 mJ/m^2 [132]. Molecular dynamics simulation predicted that deformation mechanisms of nanocrystalline Co are dominated by slip of partial

dislocations and stacking faults [133-135]. Thus, the strengthening mechanisms of stacking faults or twins in Co are highly interesting.

However, pure polycrystalline Co usually occurs as two phase mixture: hexagonal closed packed (HCP), and metastable face centered cubic (FCC). The coexistence of these two phases increases the complexity on identifying the role of twinning or stacking faults in strengthening mechanisms of Co [87, 88, 136]. For example, Wu et. al, have seen the both FCC (100) and HCP (0002) grains after SMAT on polycrystalline Co. Among these two types of grains, (111) stacking faults intersecting ribbons has been found in FCC grains, where parallel (0002) stacking faults are found in HCP Co. However, the mechanical properties of each type of stacking faults lacking due to the coexistence of the two phases [87, 88]. Therefore, the fabrication of single crystal FCC or HCP Co is clearly needed.

The epitaxial film growth by deposition sheds light on solving this problem. It has been found that the deposited Co film on single crystal Cu or Ni substrate is epitaxial FCC structure [40, 137]. However, these studies were focused on FCC-to-HCP phase transformation and magnetic properties in FCC Co with the film thickness less than 100 nm [138, 139]. To date, there is no report on mechanical properties of epitaxial FCC Co film at room temperature.

In this study, we investigate the mechanical properties of sputtered, epitaxial Co films with 1.2 μm thickness by using nanoindentation technique. By applying epitaxial Cu seed layer on Si substrates, epitaxial FCC (100) and HCP (0002) Co films can be successfully achieved, respectively. High density stacking faults with an average spacing of a few nanometers are observed on (0002) Basel planes in HCP Co films. Compared to

HCP Co, high density stacking faults intersecting ribbons are observed on different (111) planes.

By tailoring the deposition parameters, we can control the volume fraction of the stacking faults intersecting ribbons in FCC Co from 50% to 10%. The indentation hardnesses of the FCC Co are in the range of 4-5 GPa with different volume fraction of the stacking faults. Moreover, at the same volume fraction, the stacking fault intersecting ribbons in FCC Co is more effective on blocking dislocation compared to the parallel conventional stacking faults in HCP Co.

III.3 Experimental

Cu (99.995%) and Co (99.95%) targets were used to deposit 1.2 μm Co with 0.1 μm Cu seed layer on HF etched Si (100) and (110) substrates by dc magnetron sputtering. The base pressure of the sputter chamber was 6.7×10^{-6} Pa and Ar pressure was $\sim 2 \times 10^{-1}$ Pa during deposition. There was no heating or cooling on substrates during deposition. The deposition rate was ~0.5 nm/s for Cu. The deposition rate was varying from 0.1 nm/s to 0.55 nm/s for Co. X-ray diffraction (XRD) experiments were performed by using a Bruker D8 Discover X-ray powder diffractometer at room temperature. Transmission electron microscopy (TEM) was conducted on a JEOL 2010 microscope operated at 200 kV. High resolution TEM (HRTEM), scanning transmission electron microscopy (STEM) and energy dispersive X-ray (EDX) analysis were performed on an FEI Tecnai ST F20 microscope operated at 200 kV, equipped with a Fischione ultra-high resolution high-angle annular dark field (HAADF) detector and Oxford instruments' EDX detector with a spatial resolution of ~ 1 nm for chemical analysis. Hardnesses and elastic moduli of the

films were measured by a Fischerscope HM 2000XYp micro/nanoindentor with a Vickers diamond indenter tip. The maximum indentation depth was kept at 10~15% of total film thickness.

III.4 Results

XRD patterns of as-deposited 1.2 μm Co layer on the Si (100) and (110) substrates with 0.1 μm Cu seed layer in Fig. 32 reveal the epitaxial growth of FCC (200) and HCP (0002) Co, respectively. Consider FCC is metastalble phase in Co, a (110) phi scan on FCC (100) Co confirms the four-fold FCC symmetry with 45° in-plane rotation with Si (100) substrate. Furthermore, various deposition rates are applying during epitaxial growth of Co. The deposition rates can be tailored by several parameters such as deposition flux or deposition power. In this study, deposition rates are controlled by deposition power, which varies the atom kinetics during deposition. Table 4 shows the relation between deposition power and actually deposition rates. Fig. 33 shows XRD profile of FCC and HCP Co at various deposition rates. Higher deposition rate (0.55nm/s) leads to the strongest peak intensity in both systems, showing the better texture of the film. However, with decrease the deposition rates to 0.15 nm/s, the HCP peak intensity is about ~1/3, while FCC peak intensity is about ~ 1/50 if compared to their peaks at high deposition rates (0.55nm/s). Deposition kinetics may affect the structure in both textured epitaxial Co films.

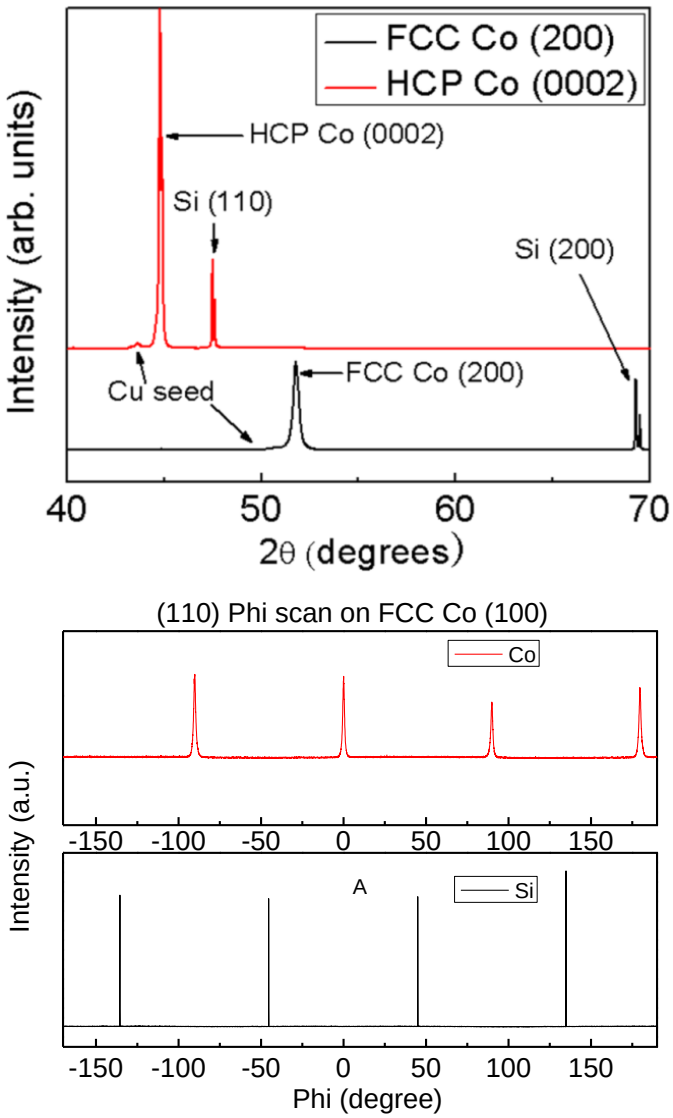

Figure 32 (a) XRD profiles shows the epitaxial growth of FCC (100) Co on Si (100) and HCP (0002) Co on Si (110) substrates. In both cases a Cu seed layer (~ 100 nm) was used. (b) (110) phi scan on FCC Co (100) confirms the epitaxial growth of FCC (100) Co with 45° in-plane rotation with Si (100) substrate.

Table 4 The relation between various deposition parameters during epitaxial growth of Co

Substrate/seed layer	Deposition power of Co (W)	Deposition flux of Co (sccm)	Deposition rates of Co (nm/s)
Si (100), Si (110)/Cu	100	40	0.15
Si (100), Si (110)/Cu	200	40	0.3
Si (100), Si (110)/Cu	400	40	0.55

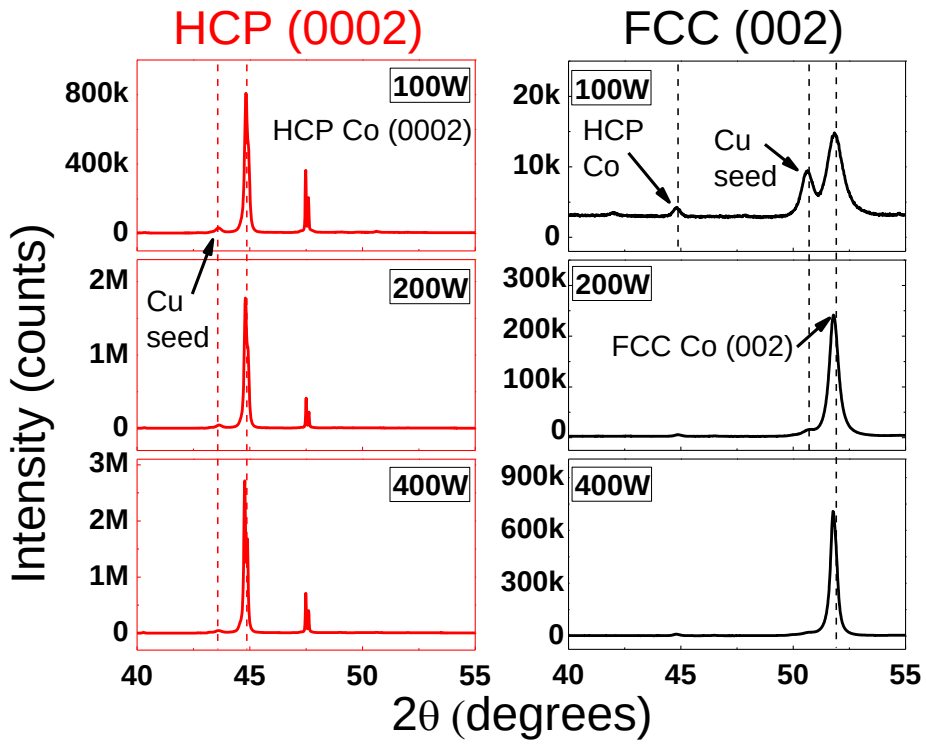

Figure 33 XRD profiles of FCC (100) and HCP (0002) Co deposited at three different deposition rates. Higher deposition rate (as indicated by deposition power) leads to stronger peak intensity in both systems, but clearly more in FCC Co.

Fig. 34 shows the low magnification bright field TEM micrographs in (a) HCP (0002) and (b) FCC (100) Co at the deposition rate 0.55nm/s. Inserted selected diffraction patterns reveal the in-plane epitaxial growth. High density parallel stacking faults (SFs) are formed in HCP Co, while (111) stacking faults intersecting ribbons are formed at different (111) planes in FCC Co. It is worth noting that, the stacking faults in HCP Co are parallel to the substrate (perpendicular to the growth direction). In comparison, the stacking faults are inclined to the substrate surface and growth direction in FCC Co. The details of these inclined stacking faults are examined by both high resolution (HR) TEM and Fast Fourier Transforms (FFT) in Fig.35 at (a) Cu/Co interface and (b) crossover area in Co layer. The inclined stacking faults are initiated right at the Cu/Co interface with a few nanometers spacing. They are then penetrated into Co layer during the film growth and crossover on different (111) planes.

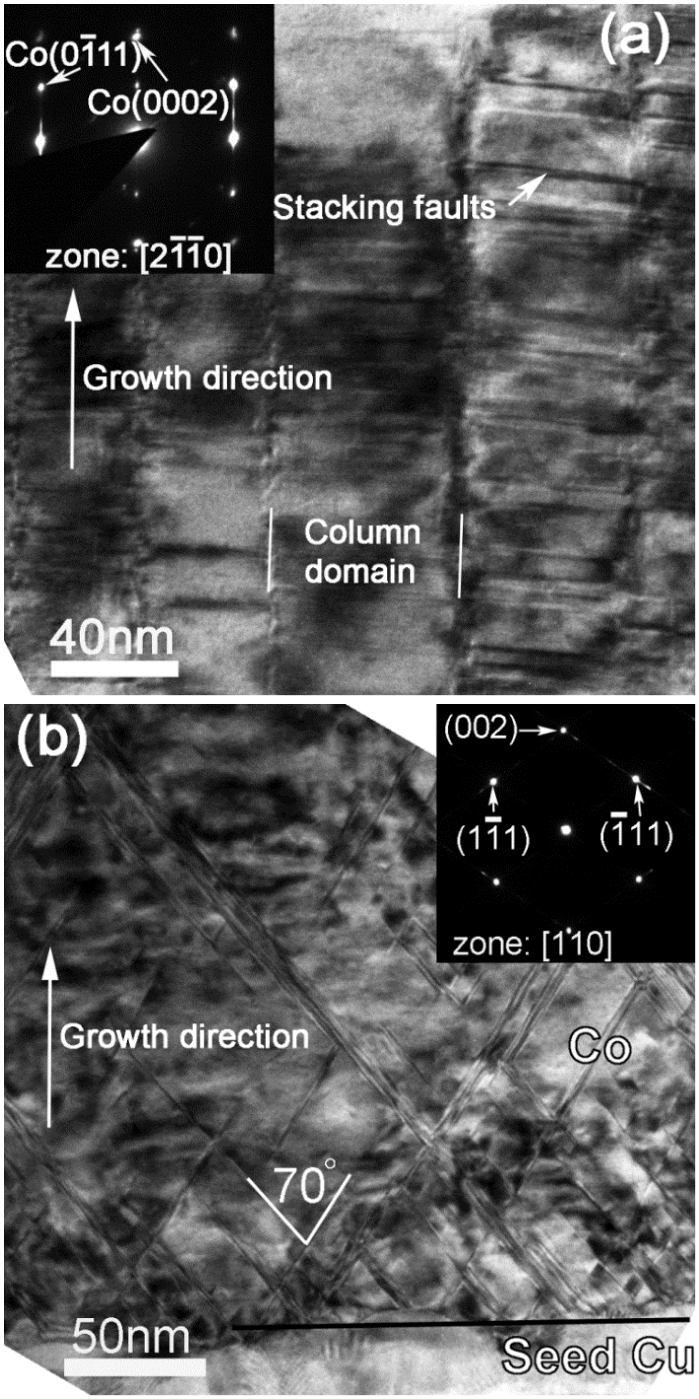

Figure 34 Low magnification bright field (BF) TEM micrographs show that (a) HCP (0002) Co grew epitaxially on Si (110) and contained a high density of parallel stacking faults (SFs) on (0002) Basel plane. (b) FCC (100) Co grew epitaxially on Si (100) and contained two (111) stacking faults intersecting ribbons with 70° angle with examining along [110] zone axis

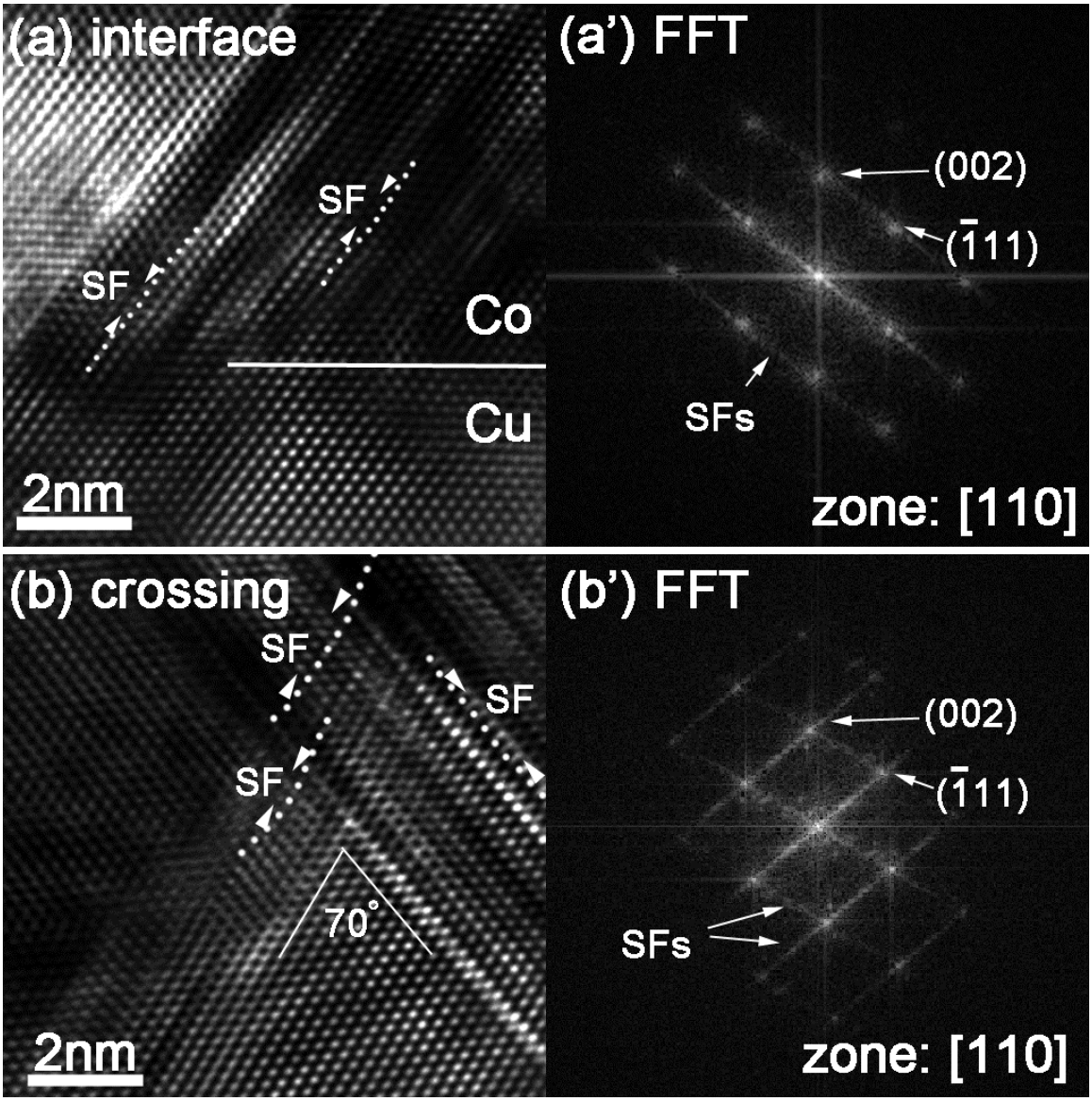

Figure 35 High resolution (HR) TEM micrographs of FCC (100) Co: (a) at Cu/Co interfaces and (b) in Co layer. Stacking faults (marked as SF or SFs) are initiated at Cu/Co interface due to mismatch strain. In Co layer, the intersecting SFs are formed on two (111) planes. FFTs at both locations (a' and b') show the SFs on one plane in (a') and two crossing planes in (b').

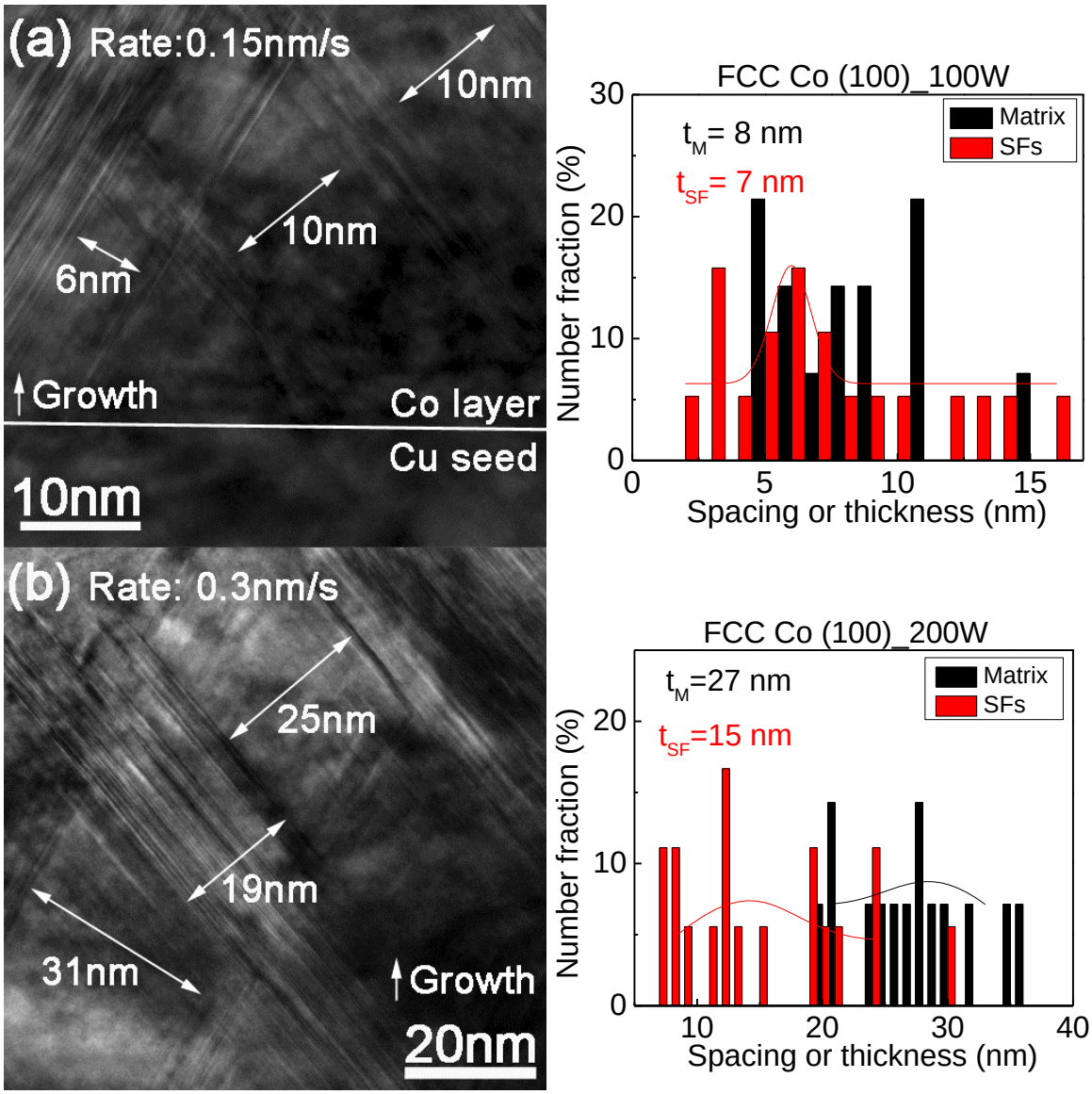

Figure 36 Thickness of SFs ribbon with deposition rates varying from 0.1 nm/s to 0.55 nm/s. (a-c) BF-TEM micrographs and statistical distribution reveal the variation of thickness of SFs and matrix with deposition rates in (a-c) FCC Co and (d) HCP Co. The SF density reduce with increasing deposition rates in FCC Co, and SF density are almost the same at various deposition rates in HCP Co.

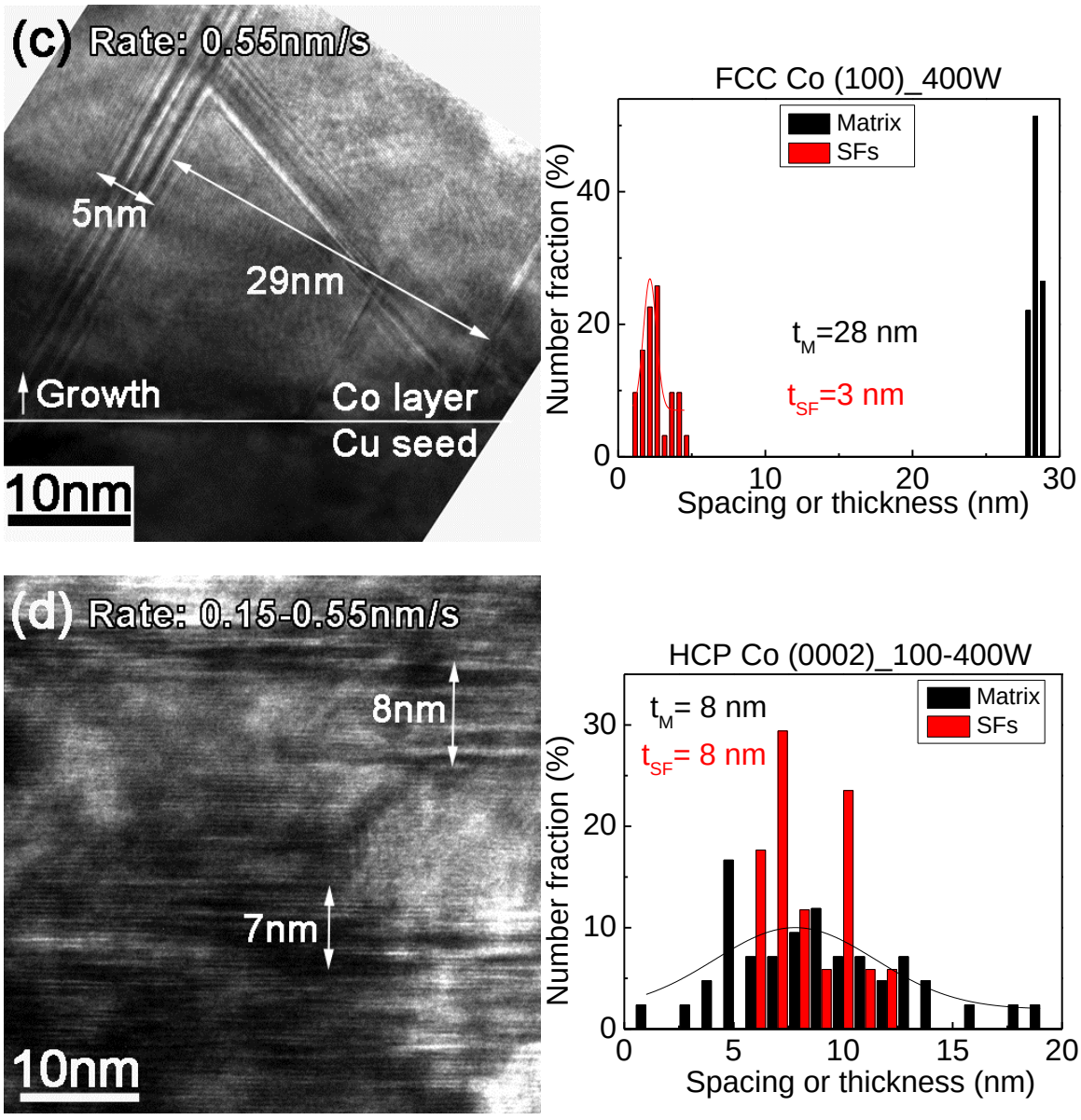

Figure 36 (continued)

Fig. 36 identifie dthe morphology of SFs at various deposition rates in FCC Co at (a) 0.1 nm/s, (b) 0.3 nm/s and (c) 0.55 nm/s. The corresponding statistical distribution

reveal the variation of thickness of SFs and matrix with deposition rates. However, in (d) HCP Co, SF density are almost similar at various deposition rates.

Fig. 37 shows the influence of the deposition rates on volume fraction on density and size of the SFs. (a) The thickness of SFs in HCP Co has literally no dependence on deposition rates over the range explored in this study. In comparison, in FCC Co, SFs spacing (matrix) increase with increase the deposition rates, while the SFs thickness first increase then decrease and reach the maximum at 0.3 nm/s. (b) The volume fraction of SFs decreased sharply with increasing deposition rates in FCC Co, whereas it remains 50% in HCP Co.

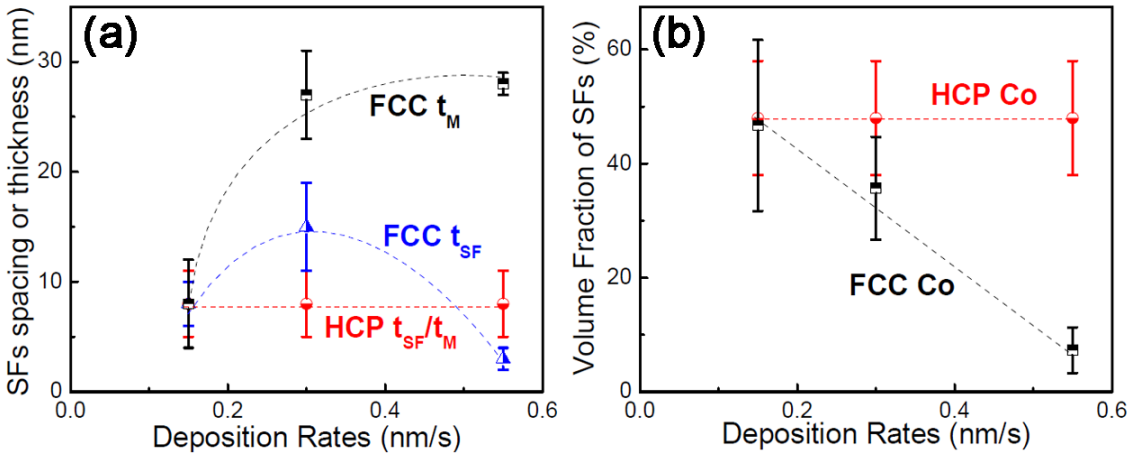

Figure 37 The influence of deposition rates on density and size of SFs. (a) The thickness of SFs in HCP Co has literally no dependence on deposition power over the range explored in this study. Conversely in FCC Co, the t_{SF} shows a maximum at 200 W, and t_M increased gradually with deposition power. (b) The volume fraction of SFs decreased sharply with increasing deposition power in FCC Co, whereas it remains 50% in HCP Co.

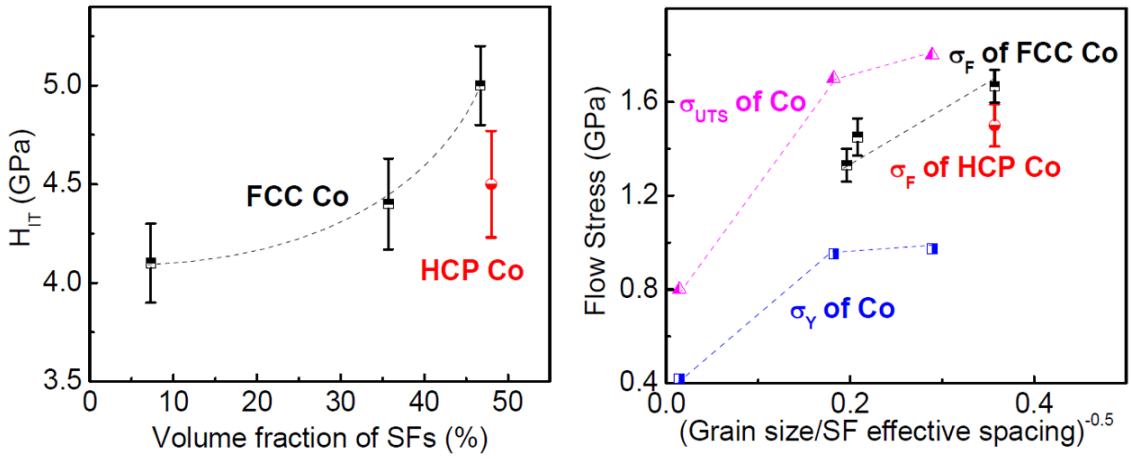

Figure 38 (a) Hardness vs. volume fraction of SFs; (b) hardness vs. average defect/grain size in the literature results

Indentation hardness of HCP and FCC Co film are ploted as a function of volume fraction of SFs as shown in Fig. 38(a). In order to better understand the strengthening mechanisms of these stacking faults, we estimate the effective SFs spacing, d_{eff} as

Equation 32 $$\boldsymbol{d_{eff} = t_{SF} \cdot V_{SF} + t_M \cdot V_M}$$

where t_{SF}/t_M are thickness of SFs and matrix, and V_{SF}/V_M are volume fraction of SFs and matrix, respectively. Fig. 38 (b) shows flow stress (1/3 of indentation hardness) vs. SFs effective spacing. The major observation are shown as below:

- In FCC Co, when volume fraction of SFs increases from ~ 10% to 50%, the indentation hardness increases from 4.2 GPa to 5 GPa.
- With similar volume fraction of SFs (50%), FCC Co is stronger than HCP Co
- Compared to tensile results of nanocrystalline Co with mixture of HCP and FCC Co [130, 131], both FCC and HCP Co in this study stay in the range between σ_y and σ_{UTS} with similar grain sizes.

III.5 Discussion

III.5.1 Epitaxial Growth via Small Lattice Mismatch

Since Cu can growth epitaxially on Si substrate, heteroepitaxial growth of Co on Si with 0.1 μm Cu seed layer can be successfully fabricated due to the small lattice mismatch. In FCC (100) Co, XRD results show that the lattice mismatch between Cu and Co is 2.6% (lattice spacing $d_{Cu(100)}$ 1.0 A , $d_{Co(100)}$ 1.75 A) Thus the critical thickness h_c to form perfect misfit dislocations can be calculated by

Equation 33 $$\boldsymbol{h_c = \frac{b}{8\pi f} \cdot \frac{1}{(1+\upsilon)} \cdot \left(ln\left(\frac{h_c}{b}\right) + 1 \right)}$$

where the magnitude of Burgers vector b is 0.255 nm, the mismatch strain f is 2.6%, the average Poisson's ratio υ is 0.3. The calculated h_c is ~ 1.8 nm when considering multilayer structure. However, as shown in Fig. 35, inclined SFs on (111) planes (bounded by groups of partial dislocations) can relieve a majority of mismatch induced elastic strain energy. Therefore, we assume that there exists a critical thickness to form partial dislocations (h_p); which can be calculated when elastic strain energy created by mismatch strain equals to the line tension of the partials:

Equation 34 $$\boldsymbol{\frac{1}{2} b_p^2 = f h_p b_p cos\lambda \cdot \frac{2(1+\nu)}{(1-\upsilon)}}$$

where the magnitude of Burgers vector of a partial dislocation b_p is 0.144 nm, f is 2.6%, υ is 0.3, λ is the angle between the slip plane and the film surface (λ 5 .7°) . The calculated h_p is ~ 2.6 nm when considering multilayer structure. These two assumptions estimates an upper and lower bound on critical thickness for form partials, which is about 2 nm as shown in Fig. 35(a).

In comparison, XRD results show that the lattice mismatch between (111) Cu and HCP (0002) Co is 1.8% (lattice spacing $d_{Cu(111)}$ 2.0 A , $d_{Co(111)}$ 2.0 A) This is small enough to have heteroepitaxial growth (<7%) of HCP Co.

III.5.2 Volume Fraction of Stacking Faults vs. Deposition Rates

Previous studies on growth nanotwinned Cu that have low stacking fault energy (γ_{sf}) has shown that the twin density increase with increase the deposition rates [76]. This can be explained as the competition between forming twin nuclei and perfect nuclei during growth process:

Equation 35 $$\gamma^*_{perfect} = \frac{\gamma}{\left(\frac{kT}{\Omega}\ln\left[\frac{J\sqrt{2\pi mkT}}{P_s}\right]\right)}$$

Equation 36 $$\gamma^*_{twin} = \frac{\gamma}{\left(\frac{kT}{\Omega}\ln\left[\frac{J\sqrt{2\pi mkT}}{P_s}\right]-\frac{\gamma_{sf}}{2h}\right)}$$

where k is the Boltzmann constant, T is the substrate temperature during deposition, Ω is the atomic volume, J is the deposition flux, P_s is the vapor-pressure above solid, m is the atomic mass of depositing species, γ_{sf} is the stacking fault energy, $\gamma^*_{perfect}$ and γ^*_{twin}. are the critical radius of perfect and twin nuclei, respectively. If the possibility of twinned nuclei formation is similar to that of perfect nuclei formation, twin boundary can be formed. It is worth noting that high deposition flux (J) contributes to the formation of nanoscale twins. Increase of deposition flux will decrease the critical twin nuclei size, and then increase the possibility to form twins. However, this is not universal relation for all the low stacking fault energy metals. If the metal with ultra-low SFE, such as Ag, γ_{sf} in Equation (36) become dominate factor. Thus γ^*_{twin} is invariable with changing deposition flux. This phenomenon has been seen in nanotwinned (111) Ag [75].

Thus, we can understand the unchanged volume fraction of parallel stacking faults in HCP Co at different deposition rates. Fig. 39 shows the critical radius between twin

and perfect nuclei in various low SFE metals at different deposition rate. The SFE energy of Co is as low as Ag, which is insulated to the deposition flux changes. Thus, it is natural to understand that HCP Co with parallel stacking faults is less effective to the deposition flux.

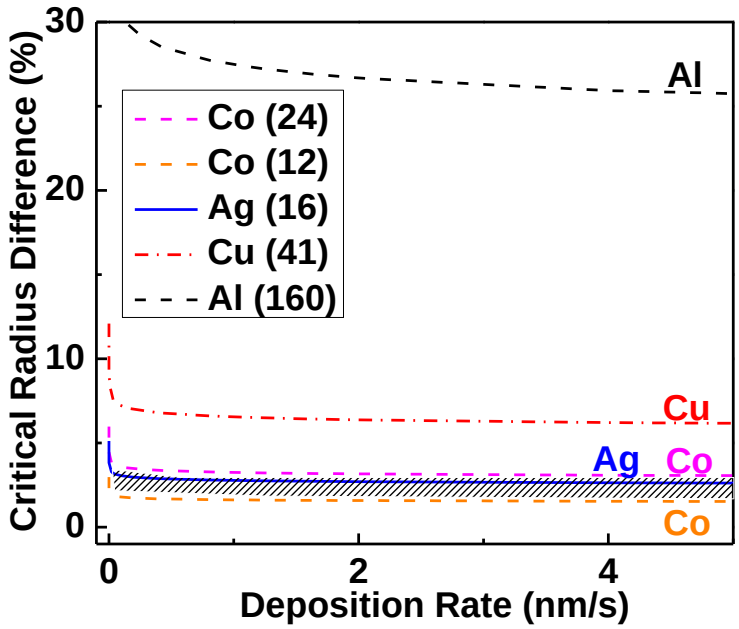

Figure 39 SFE effects on critical radius differences between twin and perfect nuclei at different deposition rate

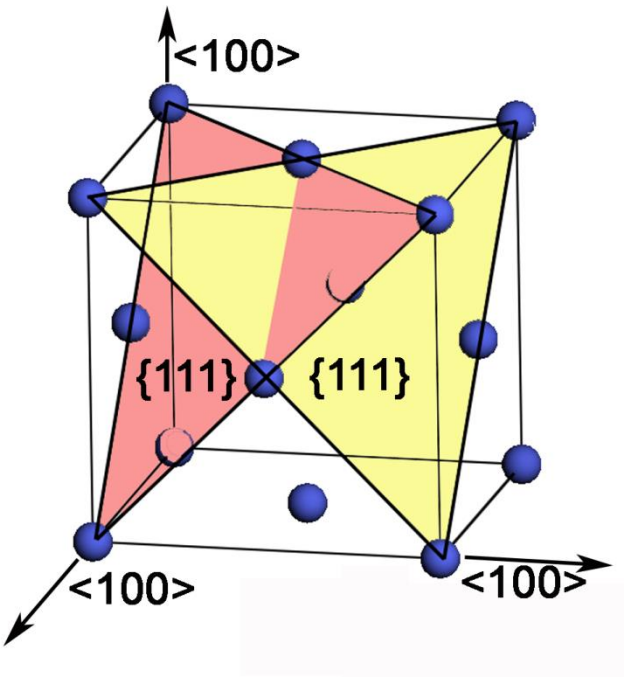

Figure 40 Schematic of (111) stacking fault intersecting ribbons in (100) Co

However, what is the formation mechanism of inclined stacking fault intersecting ribbons in FCC Co? Why deposition rates can largely affect the volume fraction of these SFs in FCC Co? Furthermore, the SFs volume fraction is inverse proportional with deposition rates, which is opposite than previous argument.

The formation of stacking faults that are inclined to the interfaces can relax misfit strain between Cu and Co as shown in schematic Fig. 40. Misfit inclined twins have been seen in Pd to relax the misfit strain between Pd and Ni [99]. Similar phenomenon has been seen in Cu/Co multilayer at large layer thicknesses. The average SFs thickness can be calculated by

$$\text{Equation 37} \quad \boldsymbol{f = \frac{b}{t_{SF}}}$$

where f is 2.6%, b is 0.25 nm. The stacking fault spacing is roughly estimated as 10 nm, which is similar to the t_{SF} at lowest deposition rates 0.15 nm/s as shown in Fig. 36(a).

As increasing deposition rates, the volume fraction of SFs decreases with increase the SFs spacing dramatically. Therefore, the first explanation is that higher deposition rate may somehow release the misfit strain. At high deposition rates, incoming atoms will squeeze with each other. The internal compressive stress increases. Meanwhile, the lattice parameter of Co is slightly smaller than Cu. Co will encounter the tensile stress when coherent interface forms between Cu and Co. This tensile stress can be partially relax by internal compressive stress that created by higher deposition flux. Thus higher deposition rates may help to release the misfit strains.

Another explanation is focused on atoms kinetics at different deposition power. At higher deposition power, the atoms have more kinetic energy to diffuse to their ideal lattice site. Therefore, inclined planar defect such as stacking faults are less likely to form in this sense. Base on the inclined SFs morphology, when atoms deposited on the substrate, they will tend to form layer by layer, instead of inclined manner which involved at least 3 atomic layers as shown in Fig. 40. Another evidence to support this argument is that inclined twins formed in (110) Ag have much less density compare to parallel (111) Ag at same deposition rate [75].

III.5.3 Strengthening Mechanisms of Stacking Faults

We now discuss the strengthening mechanisms of two different type of stacking faults. The SFs strengthening with various spacing have been reported in deformed Mg [90, 93]. In epitaxial Co, we have seen similar phenomenon that Co strength increase with increasing SFs density. Compared to nanocrystalline Co, both flow stresses of epitaxial HCP and FCC Co are 50% higher than yield strength of the nanocrystalline Co, and slightly lower than ultimate tensile strength.

It is worth noting that, at similar volume fraction of SFs, FCC Co is stronger than HCP Co. We think this is due to stacking fault intersecting ribbons are more effective barriers to block dislocation motions. As shown in Fig. 41, dislocations are largely confined in stacking faults intersecting ribbons, while dislocation could easily move along parallel stacking faults. Dislocations in some sense are much easier to be blocked by both directions in stacking faults intersecting ribbons. Thus FCC Co with stacking fault intersecting ribbons is stronger than HCP Co with parallel stacking faults.

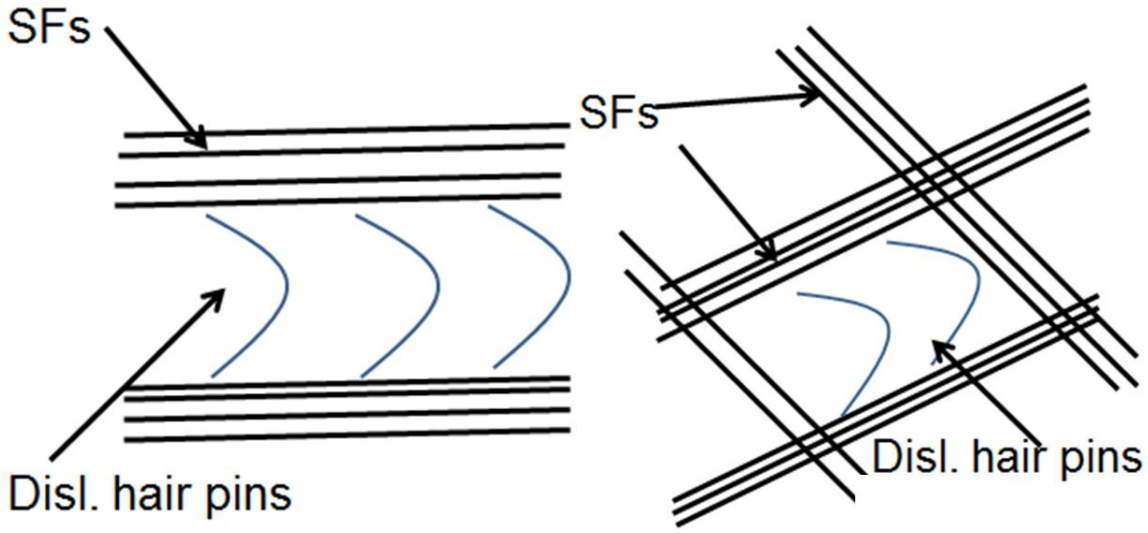

Figure 41 Dislocations interaction with (a) parallel stacking faults, and (b) stacking faults intersecting ribbons. In (a), dislocation hair pins could move along stacking faults under deformation, while dislocations hair pins are blocked by both directions in stacking faults intersecting ribbons in (b)

III.6 Conclusion

In sum, the mechanical properties of sputtered, epitaxial Cobalt (Co) films with 1.2 μm thickness are characterized. High density stacking faults with an average spacing of a few nanometers are observed on (0002) Basel planes in HCP Co films. In comparison, high density stacking faults intersecting ribbons are observed on different (111) planes. Furthermore, the volume fraction of these stacking faults intersecting ribbons in FCC Co can be controlled by deposition parameters of magnetron sputtering. The stacking faults intersecting ribbons are more effective on blocking dislocations compared to parallel stacking faults in HCP Co.

CHAPTER IV

STACKING FAULT AND PARTIAL DISLOCATION DOMINATED STRENGTHENING MECHANISMS IN HIGHLY TEXTURED CU/CO MULTILAYERS*

IV.1 Overview

We investigate the interfaces and mechanical properties of sputtered, highly (100) and (111) textured Cu/Co multilayers. In (100) Cu/Co multilayers, Co has primarily face-centered-cubic (FCC) structure and high density of inclined stacking faults (SFs). In contrast in (111) textured Cu/Co, dependent on layer thickness, high density SFs and twins parallel to layer interface are observed. When individual layer thickness, h, is a few nanometers, both systems have fully coherent FCC interface. (111) Cu/Co has similar size dependent strengthening and peak hardness compared to (111) Cu/Ni multilayers. The peak strength of (100) Cu/Co may be dominated by the transmission of partial dislocations across interface, and hence it is lower than the peak strength of (100) Cu/Ni, which is dictated by transmission of full dislocations across interfaces.

---

*This chapter reprinted with permission from "Stacking fault and partial dislocation dominated strengthening mechanisms in highly textured Cu/Co multilayers" by Y. Liu, Y. Chen, K.Y. Yu, H. Wang, J. Chen, X. Zhang; *International Journal of Plasticity*, Volume 49, pages 152-163, Copyright 2013 by Elsevier. [125]

IV.2 Introduction

Nanostructured metallic multilayers (NMM) have advanced properties, including giant-magnetron resistance [8, 9]; high mechanical strength and deformability [10-14]; and superior radiation tolerance [15-17], and hence may have various engineering applications. NMM often exhibit layer thickness dependent strengthening and near-theoretical strength at small layer thicknesses. The stiffness of layer interface has been shown to control the yield strength and strain hardening rate of NMM. [140-142]. When individual layer thickness h is greater than 50 nm, dislocations pile up against layer interfaces and size dependent strengthening behavior typically follows Hall-Petch (H-P) relation, that is hardness scales lineally with $h^{-1/2}$ [1, 2, 18-20]. When 50 nm > h > 10 nm, pile-up of dislocations becomes difficult and dislocation movement is confined within layers. Thus the corresponding strengthening mechanism can be described by the confined layer slip (CLS) model that considering bowing of dislocations [3, 21-23]. When h reduces to several nanometers, multilayers frequently achieve their maximum strength, which is determined by numerous factors including Koehler stress [24, 25], misfit dislocations, coherency stress [26-30], texture [31], twinning [32-35], and interface shear strength [36, 37]

Misfit dislocation and coherency stress originate from lattice mismatch between two materials [38, 39]. In coherent systems, the elastic strain energy builds up at greater h. When h exceeds critical thickness misfit dislocations form to release elastic strain energy [40-42, 80]. Koehler stress arises from the elastic modulus mismatch between neighboring layers and becomes significant when a large modulus difference exists [25]. In incoherent systems, a hardness plateau is typically observed at smaller h [3, 12, 18, 43,

44, 46, 141-143], wherein certain coherent systems, such as Cu/Ni, softening (the reduction of hardness at smaller h) occurs due to the formation of fully coherent interfaces [18, 21, 31, 32] or sometimes referred to as transparent interfaces, which are less effective barriers to the transmission of dislocations compared with incoherent (opaque) interfaces [45]. In incoherent systems, opaque interfaces retain slip discontinuity and remain strong barriers to the penetration of dislocations [46, 142]. Recently Zbib et al investigated the influence of both coherent and incoherent interface on the yield strength of Cu/Ni/Nb trilayers [144]. Using dislocation dynamics simulations, they show that size dependent strengthening in trilayers is controlled primarily by the weak Cu/Nb interfaces, which are dislocation sinks and the internal shear stress field activates cross-slip in adjacent Cu/Ni interfaces.

A majority of multilayer studies has focused on cubic systems, whereas multilayers consisted of at least one hexagonal closely packed (HCP) constituent received less attention. In Al/Ti multilayers, Ti showed HCP-to-FCC phase transition when h is a few tens nanometers, and the interface became fully coherent at a few nanometer layer thickness [145, 146]. In the same system, hardness rose with decreasing h but no softening was observed due to the formation of metastable phases at smaller h [147]. In Cu/Zr system with incoherent interface, however, softening has been observed due to intermixing between Cu and Zr [148]. Therefore, an immiscible system is necessary to elucidate phase stability and strengthening mechanisms in FCC/HCP multilayers. Cu/Co is one such immiscible system [149-151]. Furthermore the Cu/Co multilayers may have potential magnetic applications [152].

Meanwhile in Co, some issues remain unsolved. Polycrystalline Co usually has the combination of HCP and metastable FCC phase at room temperature, where the FCC-to-HCP phase transition occurs when strain is introduced [88, 136]. Experimental studies showed high strength and tensile ductility in nanostructured Co, wherein negative strain rate sensitivity was observed [131]. Molecular dynamics (MD) simulation and first-principle calculations predicted that deformation mechanisms of nanocrystalline Co are dominated by slip of partial dislocations and stacking faults followed by HCP-to-FCC phase transition, rather than by deformation twinning [134, 135]. The motivations of this study on Cu/Co multilayers include in the following aspects:

(1) Examine whether HCP-to-FCC phase transformation will occur in Co in Cu/Co multilayers.

(2) Compare strengthening mechanisms between Cu/Co and Cu/Ni. The facts that Koehler stress (due to modulus mismatch) and coherency stress (due to lattice mismatch) are comparable in both systems indicate that the size dependent strengthening and peak strength should be comparable in both systems.

(3) Examine if twins or high density SFs can be formed in Cu/Co system and the impact of these defects on strengthening mechanisms. Recently, our studies on (111) Cu/Ni multilayers show that high density nanotwins formed in fully coherent systems can further strengthen the multilayers and significantly reduce softening at smaller h [32].

IV.3 Experimental

Cu (99.995%) and Co (99.95%) targets were used to deposit Cu/Co multilayers on HF etched Si (100) and (110) substrates by dc magnetron sputtering. The base pressure of the sputter chamber was 6.7×10^{-6} Pa and Ar pressure was $\sim 2 \times 10^{-1}$ Pa during deposition. There was no heating or cooling on substrates during deposition. The deposition rate was ~0.5 nm/s for both Cu and Co. The individual layer thickness was identical for Cu and Co, and varied from 1 to 200 nm. Single layer (100) and (111) Cu and Co films were also deposited as references for mechanical testing. The thickness of single layer films is ~ 1.2 μm. X-ray diffraction (XRD) experiments were performed by using a Bruker D8 Discover X-ray powder diffractometer at room temperature. Transmission electron microscopy (TEM) was conducted on a JEOL 2010 microscope operated at 200 kV. High resolution TEM (HRTEM), scanning transmission electron microscopy (STEM) and energy dispersive X-ray (EDX) analysis were performed on an FEI Tecnai ST F20 microscope operated at 200 kV, equipped with a Fischione ultra-high resolution high-angle annular dark field (HAADF) detector and Oxford instruments' EDX detector with a spatial resolution of ~ 1 nm for chemical analysis. Hardnesses and elastic moduli of multilayer films were measured by a Fischerscope HM 2000XYp micro/nanoindentor with a Vickers diamond indenter tip. The maximum indentation depth was kept at 10~15% of total film thickness. The total thickness of multilayers was 1 μm when $h \leq 10$ nm, 1.5 μm when $10 \text{ nm} < h < 100$ nm, and μm when $h \geq 100$ nm, in order to avoid substrate effect and ensure that indentation experiments probe several to tens of bilayers.

IV.4 Results

XRD patterns of as-deposited Cu/Co multilayers on the Si (100) substrate in Fig. 42 reveal strong FCC (200) Co and Cu texture. When h is greater than 5 nm, the (200) Cu and Co peaks are clearly distinguishable. When h = 10 nm, the (200) Cu and Co peaks were accompanied by the first order satellite peaks. When h decreases to 5 nm, a diffraction peak corresponding to the average inter-planar spacing of Cu and Co ($d = \frac{1}{2}(d_{Cu(200)} + d_{Co(200)})$) appears. When $h \leq 2.5$ nm, the intensity of this peak becomes dominant, indicating the formation of fully coherent interface in FCC (100) Cu/Co multilayers. It is noted that XRD results indicate primarily out-of-plane coherency of multilayers, whereas the in-plane coherency is inferred from selected area diffraction (SAD) patterns of cross-sectional microstructures of multilayers that will be provided later.

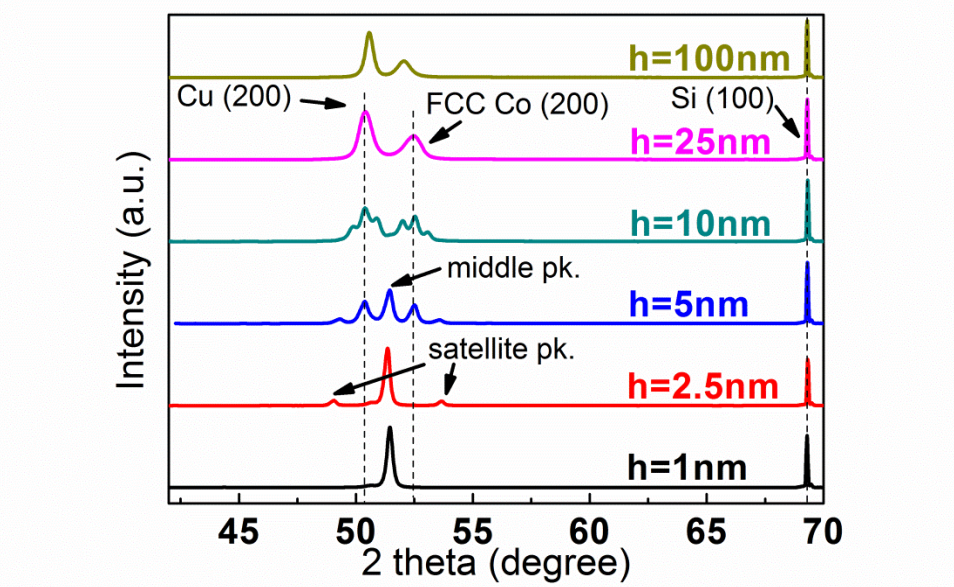

Figure 42 XRD patterns of (100) textured Cu/Co multilayers on Si (100) substrates show the formation of FCC Co when h varies from 1 to 100 nm. Satellite peaks appear when h < 10 nm. Interfaces became fully coherent when $h \leq 2.5$ nm.

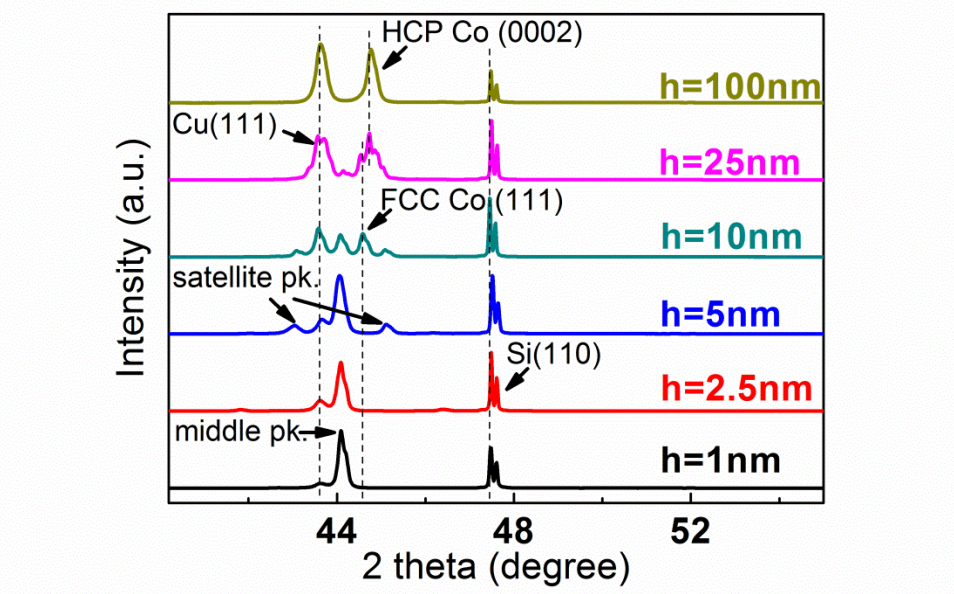

Figure 43 XRD patterns of (111) textured Cu/Co multilayers on Si (110) substrates exhibit FCC (111) Cu at all h, HCP (0002) Co at large h and FCC (111) Co at small h. The co-existence of HCP and FCC Co may occur when h = 10 or 5 nm. Satellite peaks appear when h < 25 nm. Interfaces became fully coherent when h < 5 nm and the middle peak that has the average d spacing of (111) Cu and FCC (111) Co dominates.

In comparison, Co with different phases formed in Cu/Co multilayers on Si (110) substrates as shown in XRD patterns in Fig. 43. When h ≥ 25 nm, strong textures of (111) Cu and HCP (0002) Co are evident. When h = 10 nm, three major peaks exist, corresponding to Cu, FCC (111) Co, and a middle peak with their average inter-planar spacing. It is likely that the HCP and FCC Co may coexist at this layer thickness, which becomes evident from TEM studies shown later. When h ≤ 5 nm the middle peak has the highest intensity, implying the formation of out-of-plane coherent FCC (111) type of interfaces. For simplicity these multilayers are referred to as (111) Cu/Co hereafter.

We now examine the cross-sectional microstructures of (111) Cu/Co by TEM. Fig. 44 shows SAD patterns of (111) Cu 5 nm / Co 5 nm multilayers (referred to as (111) Cu/Co 5 nm hereafter) grown on Si (110) substrate examined along two orthogonal

directions: FCC $[\bar{1}\bar{1}0]$ for Cu (HCP $[2\bar{1}\bar{1}0]$ for Co) in Fig. 44a, and FCC $[1\bar{1}2]$ (HCP $[01\bar{1}0]$) in Fig. 44b. High-resolution TEM (HRTEM) image in Fig. 44c shows that an FCC Co layer, ~ 3 nm in thickness, first formed in direct contact with Cu, and a 2 nm thick HCP Co grew thereafter. Schematics of orientation relations between FCC and HCP Co in Fig. 44d shows that FCC $[\bar{1}\bar{1}0]$ // HCP $[2\bar{1}\bar{1}0]$ and FCC (111) // HCP (0002), and FCC Co grew epitaxially on Cu.

The intensity of HCP Co diffraction dots in the SAD patterns of Cu/Co 100 nm is stronger than that of Cu/Co 5 nm as compared in Fig. 45a and 45b, implying that the volume fraction of HCP Co is greater when h increases. When h = 1 nm (Fig. 45c), fully coherent FCC Cu/Co interface formed as indicated by SAD pattern. When h = 100 nm, twins and SFs were observed in both Co and Cu layer, and the average twin spacing, t, is ~ 4 nm in Co and ~ 25 nm in Cu. When h = 5 nm, t in both layers is similar, ~ 4 nm. Finally ultra-high density of nanotwins formed with t of ~ 1 nm in Cu/Co 1 nm film, and HRTEM micrograph in Fig. 45d shows the formation of such high-density growth twins and SFs, which are outlined by horizontal lines. Thus in general, the average twin spacing in Cu/Co multilayers increased with h as shown in Fig. 46.

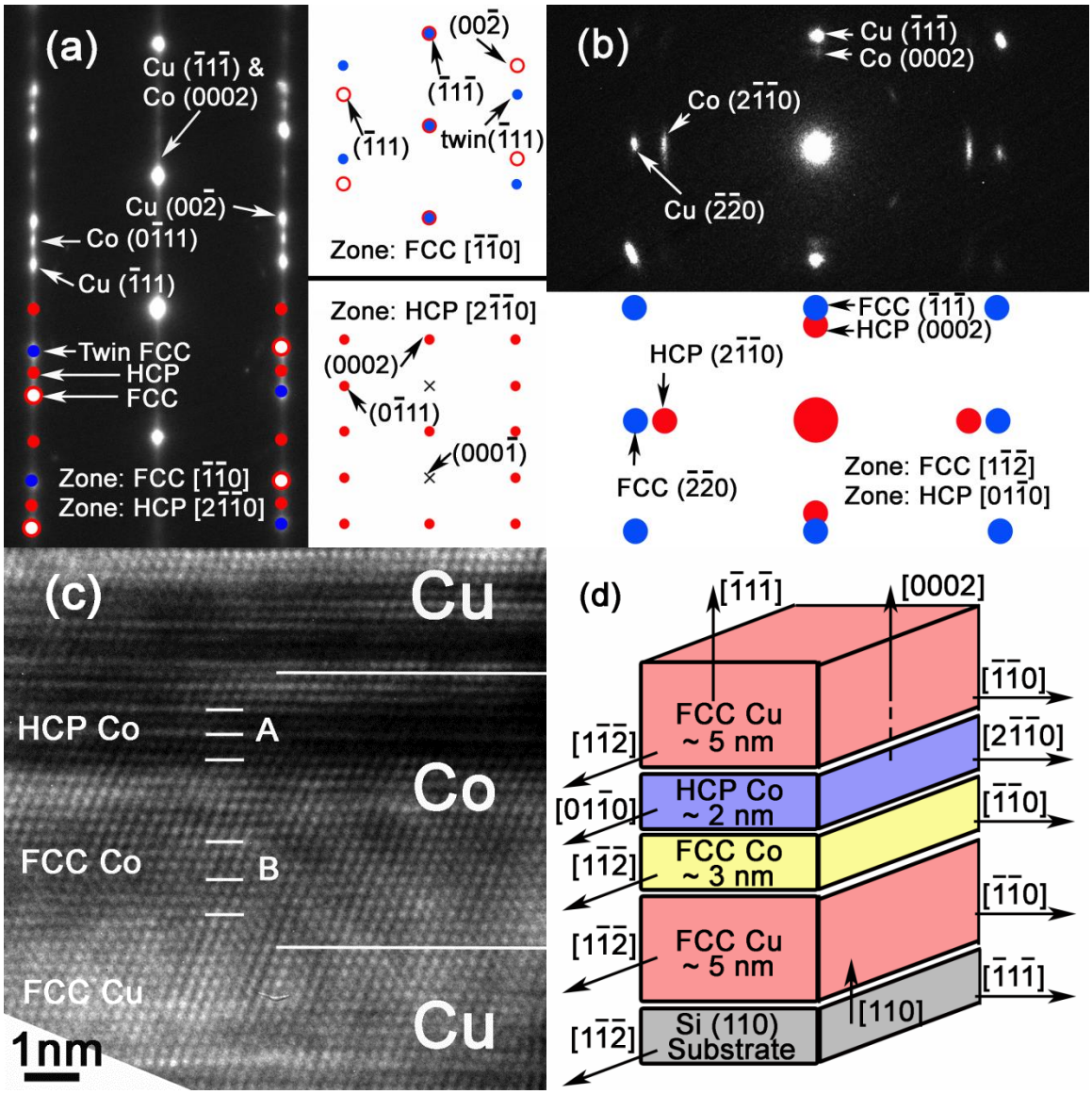

Figure 44 Selected area diffraction (SAD) patterns of (111) Cu/Co 5 nm along (a) FCC [$\bar{1}\bar{1}$0] & HCP [2$\bar{1}\bar{1}$0] zone axis; and examined along (b) FCC [11$\bar{2}$] & HCP [01$\bar{1}$0] zone axis. The SAD patterns from the two orthogonal zone axes confirmed the co-existence of FCC (111) Co and HCP (0002) Co. (c) HRTEM micrograph of (111) Cu/Co 5 nm film reveals the coexistence of HCP (marked by A) and FCC (marked by B) Co. (d) Schematics of (111) Cu/Co 5 nm shows the orientation relationship among FCC/HCP Co and FCC Cu in (111) Cu/Co multilayers on Si (110) substrate.

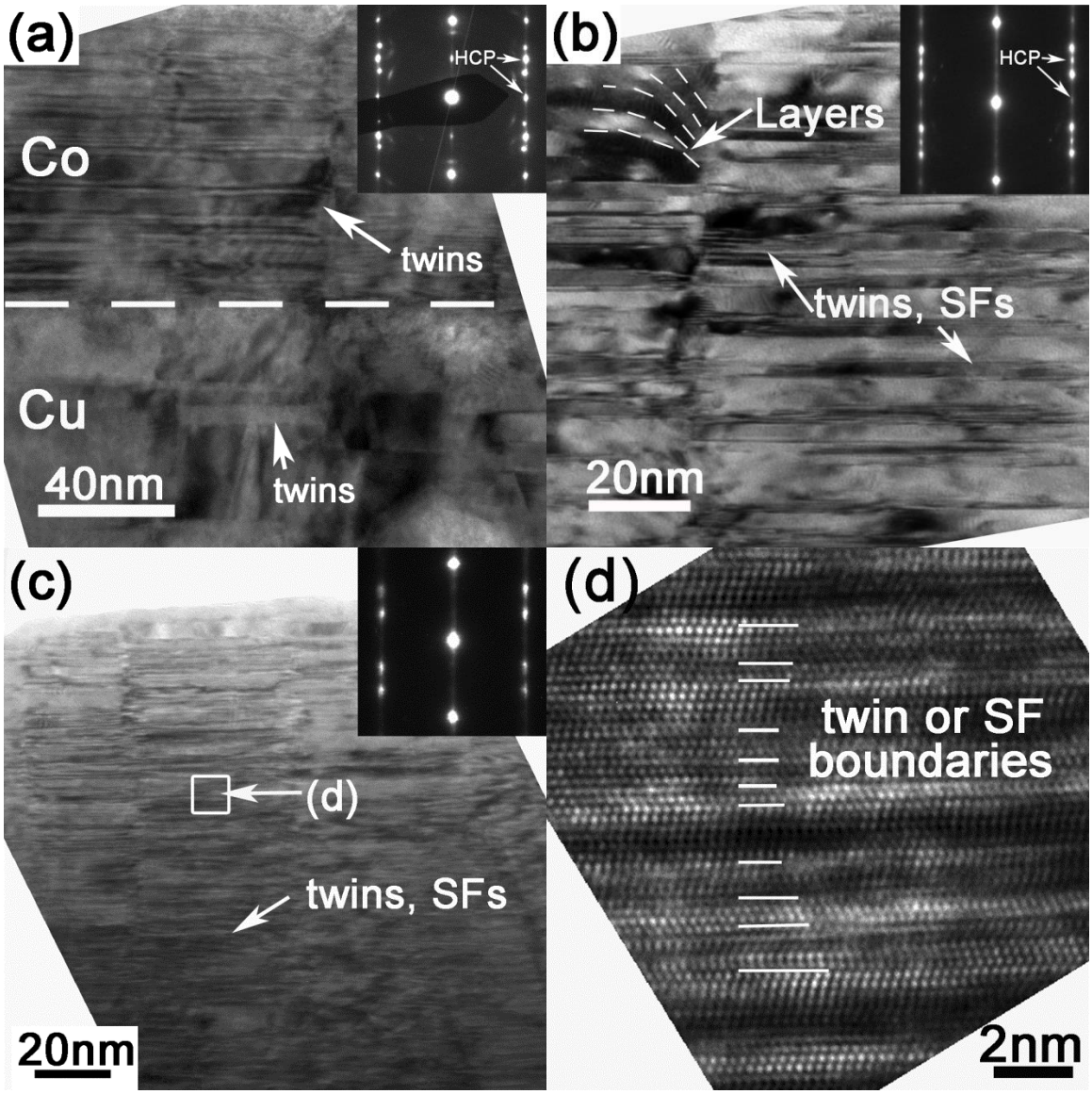

Figure 45 Bright field TEM image of (a) (111) Cu/Co 100 nm and (b) Cu/Co 5 nm multilayers on Si (110) substrates examined along Cu <110> zone axis. Cu/Co 100 nm film showed a higher density of twins and stacking faults in HCP Co than in FCC Cu layer, whereas twins of similar density was observed in Cu/Co 5 nm films The Inserted SAD patterns show the coexistence of FCC and HCP phase, and the intensity of HCP diffraction dots appeared weaker in Cu/Co 5 nm multilayers (c) TEM image of (111) Cu/Co 1 nm films on Si (110) substrate reveals the formation of ultra-high density of nanotwins. The inserted SAD pattern shows fully coherent FCC Cu/Co structure without the evidence of HCP phase. The HRTEM micrograph of the same specimen in (d) shows the average twin spacing is ~ 1 nm.

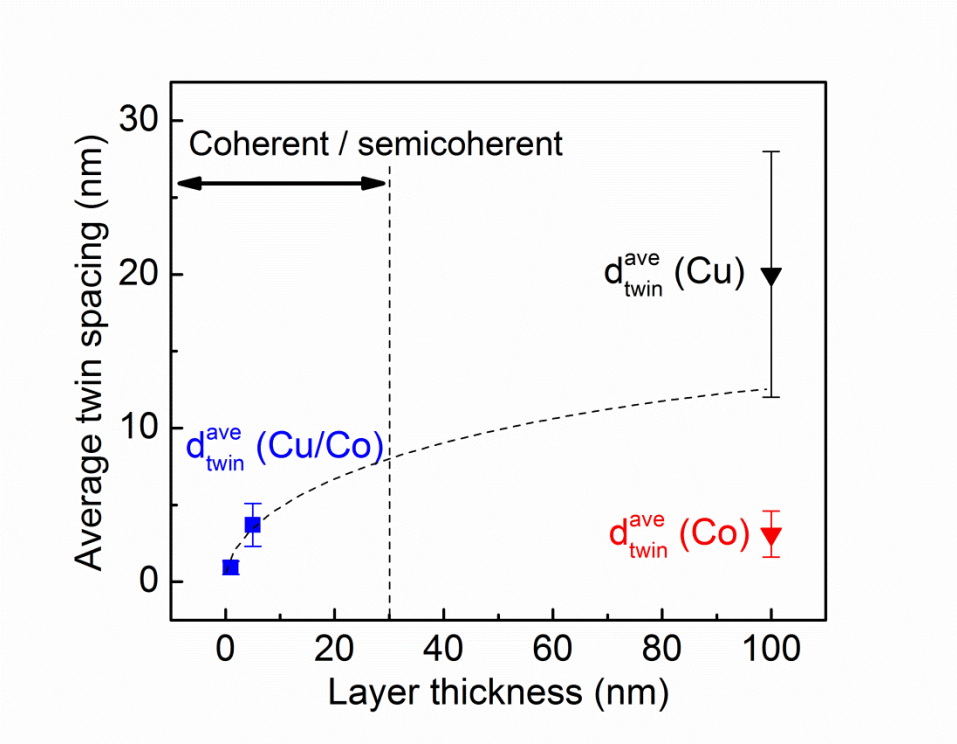

Figure 46 The average twin spacing increases with layer thickness (h) in (111) Cu/Co multilayers. When interface is coherent or semicoherent (h < 25 nm), twin density is similar in both layers. When interface is incoherent (h > 25 nm), there is a large difference in density of twin or SFs between Cu and Co layers.

The remaining TEM studies focus on (100) textured Cu/Co multilayers. Fig. 47a shows XTEM images of (100) Cu/Co 100 nm multilayer on Si (100) substrate. The inserted SAD pattern confirms the formation of highly (100) textured FCC Cu and Co. High density of SFs on inclined (111) planes formed in Co. Bright field (Fig. 47b) and centered dark field TEM image (Fig. 47c) reveal two sets of SFs that are perpendicular to each other. Inserted SAD pattern of Co in Fig. 47b shows satellite spots (arising from SFs) surrounding the (220) diffraction dots. Schematics in Fig. 47d illustrates two sets of orthogonal (111) planes when examined along FCC <100> zone axis. When h = 10 nm (Fig. 48a), the density of SFs in Co on inclined (111) planes is much less than that in

(100) Cu/Co 100 nm. Little SFs were observed when h ≤ 2.5 nm (Fig. 48b-c). Epitaxial growth of FCC Co was evidenced by SAD patterns and HRTEM micrograph in Fig. 48c. STEM micrograph and compositional line profiles of Cu/Co 2.5 nm in Fig. 48d shows chemically alternating layer structures indicating insignificant intermixing.

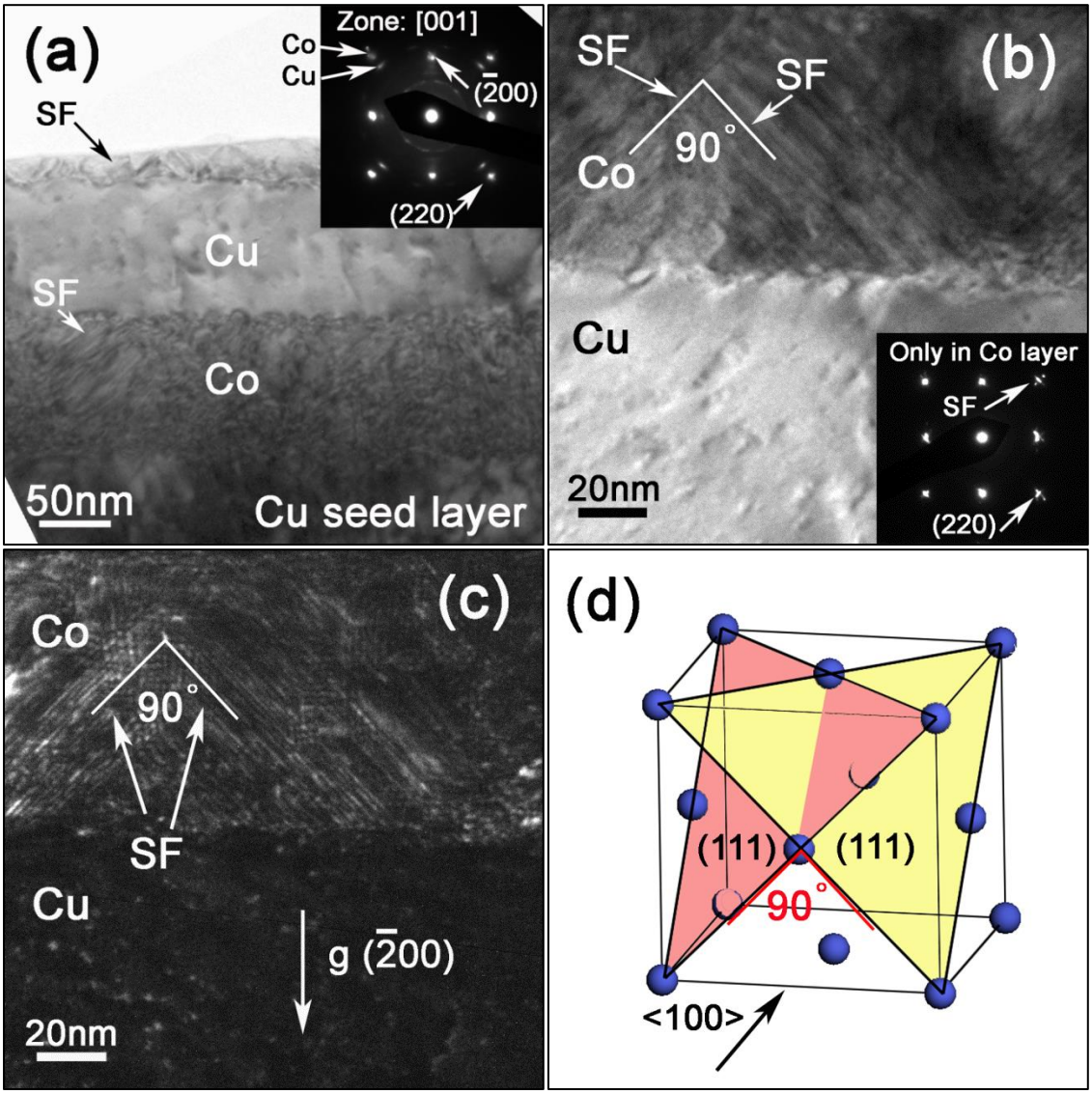

Figure 47 (a) Bright field TEM image of (100) Cu/Co 100 nm multilayer shows high density of inclined SFs in Co layer. The inserted SAD pattern shows the epitaxial growth of (100) Cu and FCC Co. At higher magnification, bright field (b) and dark field (c) TEM micrographs reveal two sets of (111) SFs that are perpendicular to each other. Schematic in (d) shows these two sets of orthogonal (111) planes when examined along <100> zone axis.

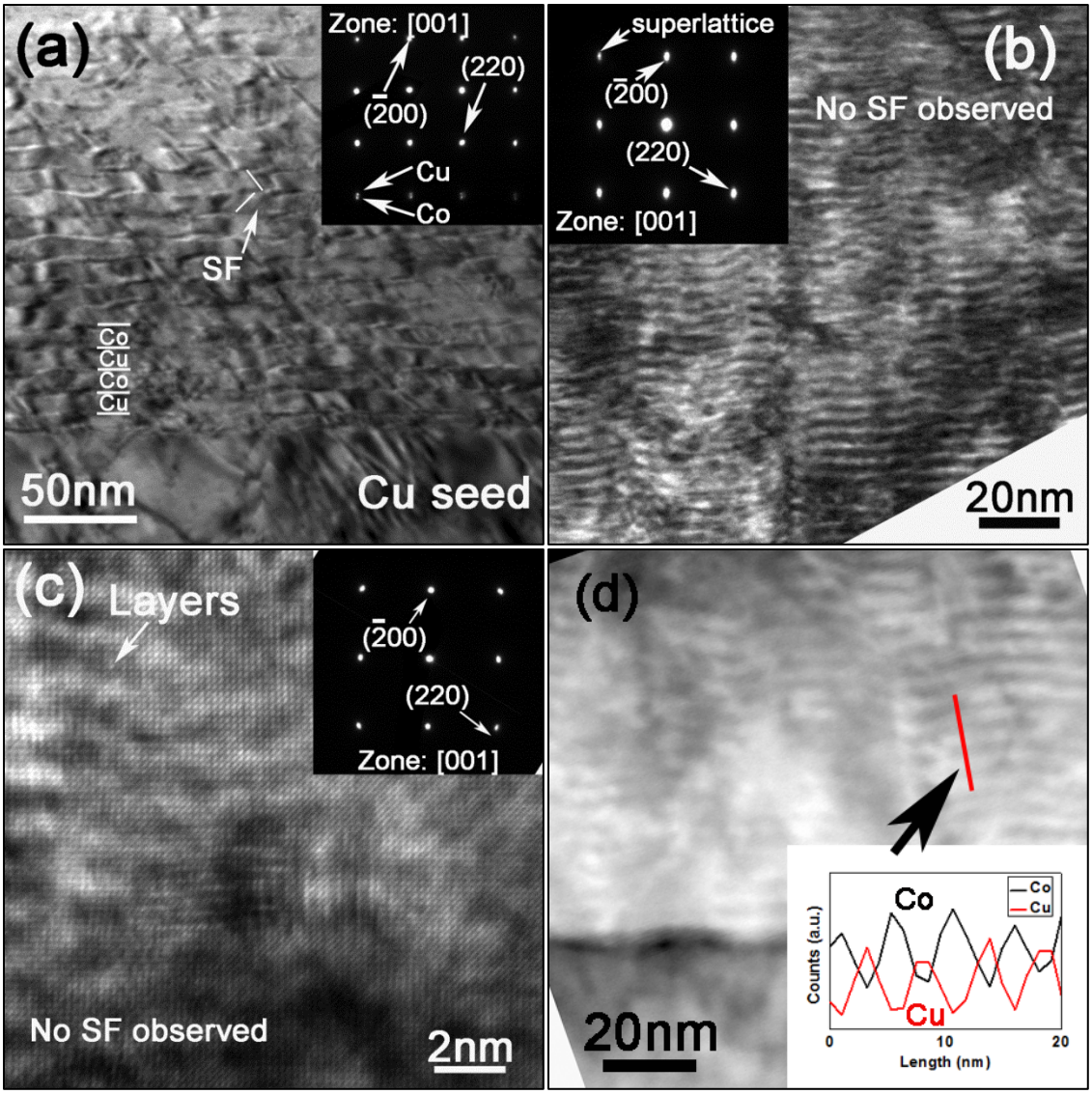

Figure 48 (a) From bright field TEM image of (100) Cu/Co 10 nm, inclined (111) SFs can be observed occasionally in Co layers. Inserted SAD pattern shows the epitaxial growth of (100) Cu and Co. In contrast, there is no stacking fault detectable in (b) (100) Cu/Co 2.5 nm and (c) (100) Cu/Co 1 nm. The inserted SAD patterns show that fully coherent interfaces can be formed when $h \leq 2.5$ nm. (d) STEM image of (100) Cu/Co 2.5 nm shows the distinguishable alternating multilayer structure. The inserted compositional profiles obtained from a line scan show chemically modulated layer structure.

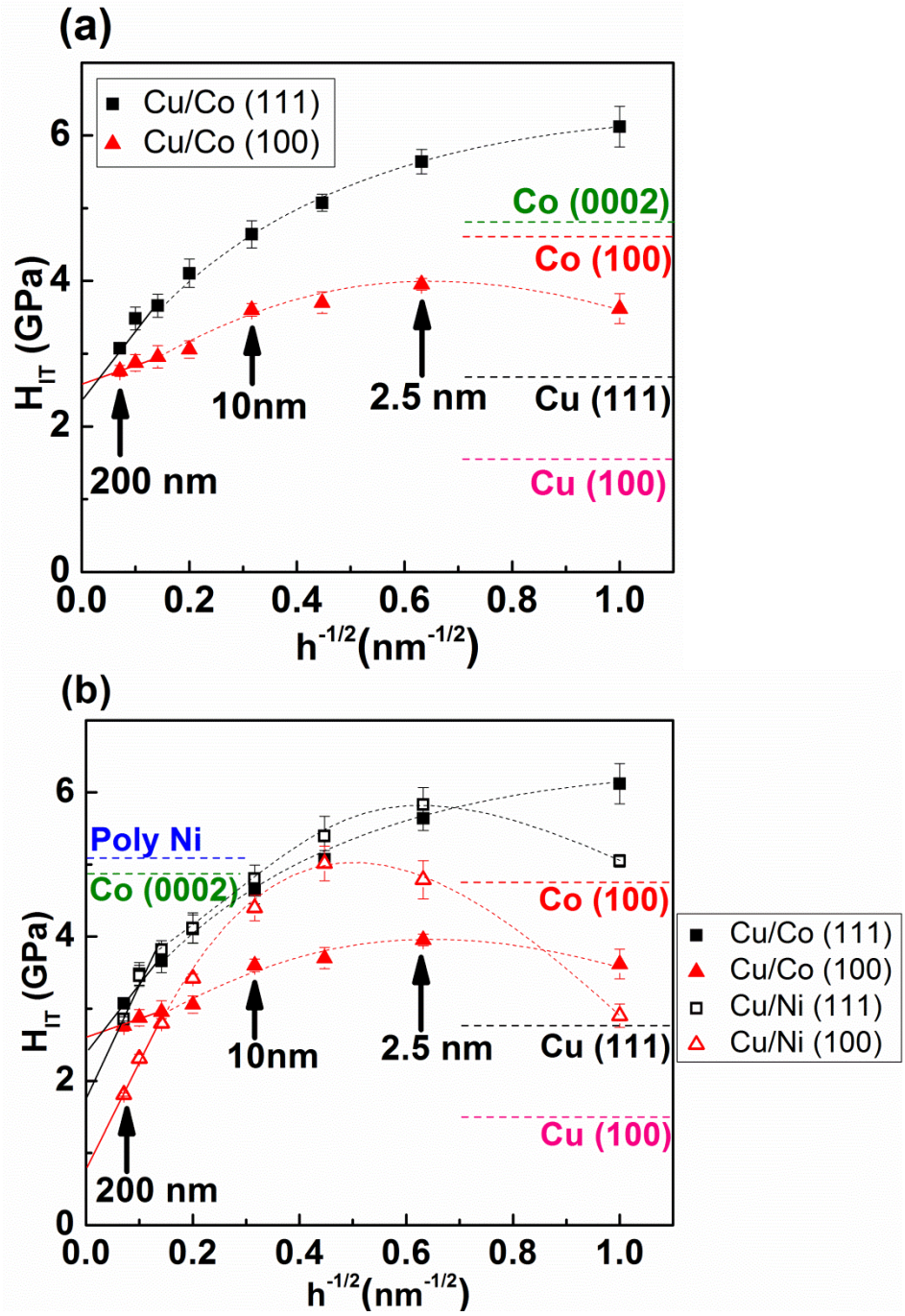

Figure 49 (a) Comparison of indentation hardness vs $h^{-1/2}$ of (100) and (111) Cu/Co multilayers. (b) Comparison of indentation hardness vs $h^{-1/2}$ among (100) and (111) Cu/Co and Cu/Ni multilayers. The hardness of (111) textured Cu/Co and Cu/Ni is comparable, whereas (100) textured Cu/Co multilayers has a much lower peak hardness than other systems. Softening was absent in the (111) Cu/Co multilayers.

Indentation hardnesses of (100) and (111) textured Cu/Co multilayers are plotted as a function of $h^{-1/2}$ in Fig. 49a. Hardnesses of single layer Cu and Co films are shown as horizontal dash lines in the same plot. Similar to Co in (100) and (111) textured Cu/Co 100 nm multilayers, (100) and (111) textured single layer Co exhibit inclined and parallel stacking faults, respectively. The following characteristics are noteworthy.

a. In general, hardnesses increased with decreasing h. The hardnesses of (111) Cu/Co multilayers were greater than those of (100) Cu/Co at all layer thickness.
b. When h ≥ 50 nm, a linear relation is identified. The H-P slopes were ~ 10.9 and 2.7 GPa $nm^{1/2}$ in (111) and (100) Cu/Co multilayers, respectively.
c. When h = 2.5 nm, the hardness of (100) Cu/Co multilayers reached a maximum and slightly decreased thereafter at smaller h.
d. When h = 1 nm, the hardness of (111) Cu/Co multilayers reached a maximum, ~ 6 GPa, the highest among all single layers and multilayers in this study. No softening was observed.

IV.5 Discussion

IV.5.1 Evolution of Microstructure with Layer Thickness

Highly (100) and (111) textured Cu/Co multilayers were synthesized. The degree of texture, epitaxy and coherency of multilayers increased with decreasing h. In (100) Cu/Co multilayers, XRD results show that the lattice mismatch between Cu and Co is 2.6% (lattice spacing $d_{\text{Cu (100)}} = 1.80\ \dot{A}$, $d_{\text{Co (100)}} = 1.754\ \dot{A}$). Thus the critical thickness h_c to form perfect misfit dislocations can be calculated by

Equation 38 $$\boldsymbol{h_c = \frac{b}{8\pi f} \cdot \frac{1}{(1+\upsilon)} \cdot \left(ln\left(\frac{h_c}{b}\right) + 1 \right)}$$

where the magnitude of Burgers vector b is 0.255 nm, the mismatch strain f is 2.6%, the average Poisson's ratio υ is 0.3. The calculated h_c is ~ 1.8 nm when considering multilayer structure. However, as shown in Fig. 47, inclined SFs on (111) planes (bounded by groups of partial dislocations) can relieve a majority of mismatch induced elastic strain energy. Therefore, we assume that there exists a critical thickness to form partial dislocations (h_p); which can be calculated when elastic strain energy created by mismatch strain equals to the line tension of the partials:

Equation 39 $$\frac{1}{2}b_p^2 = f h_p b_p cos\lambda \cdot \frac{2(1+\nu)}{(1-\nu)}$$

where the magnitude of Burgers vector of a partial dislocation b_p is 0.144 nm, f is 2.6%, υ is 0.3, λ is the angle between the slip plane and the film surface ($\lambda = 54.7°$). The calculated h_p is ~ 2.6 nm when considering multilayer structure. This estimation is consistent with experimental observations, which showed that SFs were rarely observed in (100) Cu/Co when h ≤ 2.5 nm. At greater h, the elastic strain energy is released through frequent formation of SFs and thus the density of inclined SFs in Co in (100) Cu/Co increased accordingly.

In (111) Cu/Co multilayers, XRD results show that the lattice mismatch between Cu and FCC Co is 1.8% (lattice spacing $d_{\text{Cu (111)}} = 2.084\ \dot{A}$, $d_{\text{Co (111)}} = 2.048\ \dot{A}$). The h_c for the formation of perfect misfit dislocations in this system is ~ 3 nm calculated by equation (1), wherein b is 0.255 nm. Twins in this system may also release misfit strain and increase h_c. We also estimate h_p at which a partial dislocation with glide plane parallel to layer interfaces can form by using equation (2), wherein λ is 0° and b_p is 0.144 nm. The calculated h_p is ~ 2.2 nm, consistent with experimental observation: when h < 2

nm, FCC (111) Co forms via epitaxial growth; and when h = 5 nm, misfit perfect or partial dislocations form to release the coherency strain.

IV.5.2 The Formation Mechanisms of High Density Twins in (111) Cu/Co Multilayers

When decreasing h, average twin spacing t in (111) Cu/Co decreased as shown in Fig. 46. When h = 1 nm, t is ~ 1 nm. In general, low SFE (γ_{SF} is 41 and 24 mJ/m^2 for Cu and Co [48, 49]) is necessary to form high density twins. However, our previous studies show the smallest t that can be achieved in sputtered single layer Cu, Co, Ag is 9, 5, and 7 nm, respectively [52, 75, 76]. Thus SFE alone cannot explain the formation of extremely fine twins in epitaxial (111) Cu/Co 1 nm multilayer. Our recent study shows that Cu/Ni multilayers can have the smallest average twin spacing of ~ 3 nm due to the existence of coherency stress [80]. We now explore the possible formation mechanisms of ultra-fine twins in epitaxial (111) Cu/Co 1 nm film. In this system, there is no misfit dislocation as interface is fully coherent and HCP Co phase does not exist.

First we estimate the critical stress τ_c necessary to nucleate Shockley partials from classical dislocation theory [153]

Equation 40 $$\boldsymbol{\tau_c = \frac{2\alpha\mu b_p}{D} + \frac{\gamma}{b_p}}$$

where α is 0.5 for edge and 1.5 for screw dislocations, μ is the shear modulus (μ is 48 GPa for Cu, 82 GPa for Co), γ is the SFE, D is the grain size, b_p is Burgers vector of a Shockley partial. D is ~ 40 nm as observed experimentally, thus τ_c is estimated to be ~ 0.46 GPa for both Cu and Co. This value may serve as an upper-bound estimation as MD simulation shows that the required shear stress for twinning in Cu is ~ 0.15 GPa [154]. Another MD simulation also shows that SFs instead of deformation twins were formed in deformed nanocrystalline Co [135].

Secondly, we estimate the driving force available to nucleate twins during growth of Cu/Co multilayers. Partial dislocations must form prior to the formation of twins. It follows that shear stress must exist to trigger the formation of partial dislocations. At the free surface of Co islands that grow epitaxially on Cu substrate, there is no stress. But residual stress in Co quickly develops in films when moving away from free surface. Thus to introduce coherency stress in Co, an interfacial shear stress is necessary along the Cu/Co interfaces close to the free surface. The shear stress, τ, can be estimated by [84]

Equation 41 $$\boldsymbol{\tau = \frac{fE_f}{1-\nu} \cdot \sqrt{\frac{E_s h_f}{2E_f \pi x}}}$$

where E_s and E_f are respective modulus of substrate and film; h_f is the film thickness; x is the distance from the island edge; f is mismatch stain. In Cu/Co multilayer systems, given f = 2%, E_{cu} = 120 GPa, E_{Co} = 210 GPa, ν = 0.3, τ is estimated to be 0.52 ~ 0.91 GPa when x = 1 ~ 3 h_f. This estimation shows that the shear stress is sufficient to nucleate partials in (111) Cu/Co multilayers.

IV.5.3 Strengthening Mechanisms

As shown in Fig. 49a, the indentation hardness of (111) Cu/Co is greater than its (100) counterpart at all h. Furthermore, there is a large discrepancy of maximum hardness between the two systems.

When h ≥ 50 nm, a large difference in H-P slope was measured between (111) and (100) Cu/Co. We can estimate the interface barrier stress τ^* by [18]

Equation 42 $$\boldsymbol{K'_{HP} = \sqrt{\frac{\tau^* \mu b}{\pi(1-\nu)}}}$$

where K'_{HP} is H-P slope, τ^* is the critical resolved shear stress for the transmission of dislocations (interface barrier strength), μ is the shear modulus of softer layer (μ = 48

GPa for Cu). By using b = 0.255 nm and ν of 0.3, and measured K'_{HP}, we obtain τ^* of 0.02 GPa and 0.33 GPa for (100) and (111) Cu/Co, respectively. The calculated peak hardness is then 0.16 GPa and 2.77 GPa by multiplying Schmidt (2.8) and Tabor factors (3). This is in large contrast to the measured peak hardness (4 GPa and 6.1 GPa) for (100) and (111) Cu/Co.

To understand the large discrepancy in size dependent strengthening mechanism in the two Cu/Co systems, it is important to compare them to the strength of the two Cu/Ni multilayers with similar texture. As shown in Fig. 49b, the size dependent variation of hardness of (111) textured Cu/Co and Cu/Ni is very close to each other except when h is 1 nm. However, there is a large difference in (100) textured Cu/Co and Cu/Ni. The strength of (100) Cu/Co is much greater than Cu/Ni system when h ≥ 50 nm. As shown in Fig. 47, high density inclined SFs were observed in Co when h ≥ 50 nm, whereas SFs or twins are largely absent in (100) Cu/Ni [80]. SFs are effective barriers to the transmission of dislocations and thus provide extra hardening in Cu/Co system. The effective feature size that determines the hardness of (100) Cu/Co system is no longer the layer thickness h. High density inclined SFs in Co lead to reduced effective feature size in (100) Cu/Co. Thus should the effective feature size be used, the H-P slope would be greater than that measured by using layer thickness alone. This observation also explains the large discrepancy between measured peak strength and the calculated value from the H-P slope as discussed previously.

When 50 > h > 10 nm, dislocation pile-up becomes increasingly difficult and bowing of single dislocation in the layers comes into operation. Based on the CLS model [3], the critical resolved shear stress τ_{cls} can be calculated as

Equation 43 $$\boldsymbol{\tau_{cls} = \frac{\mu b}{8\pi h'}\left(\frac{4-\nu}{1-\nu}\right)\cdot\left(ln\frac{h'}{b}\right)}$$

where h' is the distance between obstacles along the slip plane between adjacent interface. Using μ = 48 GPa, h' = 25 nm, b = 0.25 nm, τ_{cls} is calculated to be ~ 0.46 GPa, corresponding to a hardness value of ~ 3.8 GPa. This calculation fits experimental results ((111) Cu/Co 25 nm) well. We also noticed that the hardness of (100) Cu/Co in this range (h = 10-50 nm) is lower than those of (100) Cu/Ni and (111) Cu/Co. Mechanisms behind such a difference will become evident when we compare peak strength of these systems in the following section.

When h ≤ 5 nm, (100) Cu/Co multilayer reaches a maximum hardness, which is ~ 1 GPa less than that of single layer Co and (100) Cu/Ni, and ~ 2 GPa less than that of (111) Cu/Co and Cu/Ni. In (100) Co single layer, high-density inclined SFs exist with an average spacing of a few nanometers. These SFs lead to high strength in single layer Co. In comparison, no SFs were observed in (100) Cu/Co 2.5 nm.

We now analyze the large difference in peak strength between FCC (100) Cu/Co and (100) Cu/Ni systems. The interface barrier resistance τ_{int} can be expressed as

Equation 44 $$\boldsymbol{\tau_{int} = \tau_K + \tau_{ch} + \tau_d + \tau_{Ke} + \tau_{coh}}$$

where τ_K is Koehler stress originating from modulus mismatch, τ_{ch} is chemical interaction term related to SFE difference between layer constituents, τ_d is determined by misfit dislocations due to lattice mismatch, τ_{Ke} is the modification to Koehler stress due to the variation of elastic modulus in each layer [31], and τ_{coh} is derived from coherency stress. In coherent Cu/Co and Cu/Ni systems, the differences of contributions of the last three terms (in equation (7)) to strengthening between are insignificant, and hence it follows that

Equation 45 $$\boldsymbol{\tau_{int} \approx \tau_K + \tau_{ch} = \frac{\mu_1(\mu_2-\mu_1)b}{4\pi(\mu_2+\mu_1)l} + \frac{\gamma_2-\gamma_1}{b}}$$

where $\mu_2 - \mu_1$ is the modulus difference, l is dislocation core size 3-4 b [155, 156], and $\gamma_2 - \gamma_1$ is the SFE difference. By using the parameters from Table 5, τ_K and τ_{ch} can be calculated as shown in Table 6. τ_{int} is estimated as 0.76 and 0.57 GPa for (100) Cu/Ni and FCC (100) Cu/Co system, respectively. As shown in Table 6, τ_K and τ_{ch} terms are comparable, 0.43 vs. 0.33 GPa, in (100) Cu/Ni system, whereas in (100) Cu/Co systems, τ_{ch} is negligible (0.07 GPa) compared to τ_K (0.5 GPa). Thus the calculation shows Cu/Ni has higher peak hardness (by ~ 1.5 GPa) than Cu/Co system, compared well to experimental observations (~1.2 GPa). Therefore, the low intrinsic SFE of Co is one of the key factors that lead to reduced peak strength in FCC (100) Cu/Co multilayers. A similar level of peak hardness difference by 1.3 GPa is calculated (Table 6) for (111) textured Cu/Co and Cu/Ni. But such a calculated hardness difference is much higher than what is observed experimentally (insignificant difference). Such large discrepancy will be discussed later when the significance of nanotwins is considered.

Table 5 Material parameters of FCC Cu, Ni and Co.

Material	a $(\dot{A})$	μ (GPa)	γ_{SF} (mJ/m^2)
Cu	3.61	48	41
Co	3.53	82	24
Ni	3.52	76	125

Table 6 The influence of SFE difference on strengthening of FCC (100) and (111) textured Cu/Co and Cu/Ni systems. ΔH_{cal} is calculated hardness difference from τ_{int} by using Schmidt and Tabor factor, $\Delta H_{cal} = H_{cal}^{Cu/Ni} - H_{cal}^{Cu/Co}$. ΔH_{mea} is measured hardness difference from Fig. 49 (b), $\Delta H_{mea} = H_{mea}^{Cu/Ni} - H_{mea}^{Cu/Co}$.

Regime	Interface	$\tau_K\ (GPa)$	$\tau_{ch}(GPa)$	$\tau_{int}(GPa)$	ΔH_{cal} (GPa)	ΔH_{mea} (GPa)
Peak value h = 2.5~5 nm	Cu/Ni	~ 0. 43	~ 0.33	~ 0.76	1.5	1.2
	Cu/Co	~ 0. 5	~ 0.07	~ 0. 57		
Softening h = 1 nm	Cu/Ni	~ 0. 18	~ 0.33	~ 0.51	− 0.1	− 0.6
	Cu/Co	~ 0. 45	~ 0.07	~ 0.52		
Peak value (111) interface	Cu/Ni	~ 0.6	~ 0.33	~ 0.93	1.3	− 0.2
	Cu/Co	~ 0.7	~ 0.07	~ 0.77		

The influence of SFE on interface barrier resistance can be interpreted from hypothetical schematics in Fig. 50. In (100) textured Cu/Ni system, partials in Cu migrated toward layer interfaces. The transmission of partials across interfaces is difficult as Ni has much higher SFE than Cu. Consequently a full dislocation has to be nucleated in Ni to accommodate plastic deformation across interfaces. It is likely that constriction of partials may have occurred in Cu adjacent to interface as well. Unlike Cu/Ni interface, in FCC Cu/Co system, Co has even lower SFE than Cu, and hence the transmission of partials in Cu across interface is feasible (although there is resistance arising from Koehler stress). Meanwhile partials in Cu do not need to form a constriction when encountering the Cu/Co interface. The interface barrier resistance for transmission of partials (in Cu/Co) shall be much lower than that for the transmission of a full dislocation across the Cu/Ni interface. Therefore Cu/Ni system should have a higher peak hardness than Cu/Co.

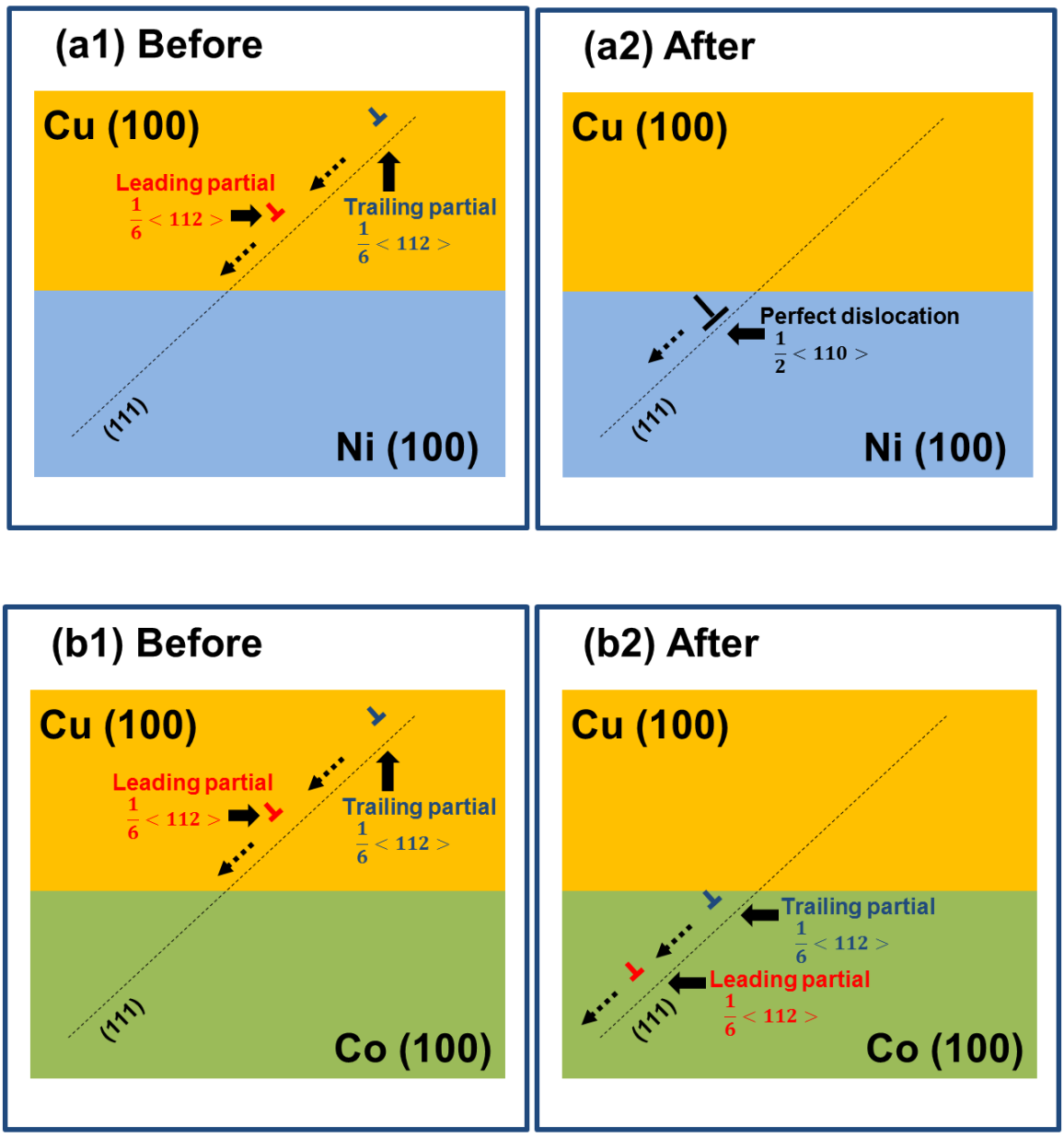

Figure 50 Hypothetical schematics illustrate the difference between dislocation transmissions across (100) Cu/Ni and (100) Cu/Co layer interfaces. (a) In (100) Cu/Ni, the high SFE of Ni prohibits the transmission of partial (from Cu) across interface. Instead, a full dislocation must be nucleated in Ni to accommodate plastic deformation. In contrast in (b) (100) Cu/Co system, due to the low SFE of Co, partials in Cu layer could penetrate across layer interface without forming a perfect dislocation.

Significant softening occurs in (100) Cu/Ni system. The hardness of Cu/Ni 1 nm films is ~ 2 GPa lower than Cu/Ni 2.5 nm films. In contrast softening in (100) Cu/Co system is insignificant. This may be related to difference in dislocation core size between partials and perfect dislocations. In (100) Cu/Ni system, the core spreading of dislocations is ~ 2.8 nm. Hence in (100) Cu/Ni 1 nm multilayers, the magnitude of Koehler stress decreases more than half, from 0.5 to ~ 0.18 GPa ([31]. In contrast, the maximum strength in (100) Cu/Co system is dominated by the transmission of partials across interface without constriction (shown in Fig. 50b). As the core size of Shockley partial is ~ 2b [31], the magnitude of core spreading (~ 1 nm or so) is also much less than that in Cu/Ni system. The narrower core of partials alleviates the rapid reduction of τ_K in Cu/Co system when h = 1 nm. Assuming that the magnitude of Koehler stress is only reduced by 10% in Cu/Co system when h = 1 nm, we arrive that the peak strength of (100) Cu/Co is ~ 0.52 GPa, comparable to 0.51 GPa in (100) Cu/Ni systems. Hence softening is much more pronounced in (100) Cu/Ni than that in Cu/Co system as shown in Table 6.

Should (100) Cu/Ni have a higher peak strength than (100) Cu/Co, one expects the same relation may be applicable in the (111) Cu/Ni and Cu/Co systems. However, the hardness of (111) Cu/Co multilayers is nearly identical to that of (111) Cu/Ni. High density twins and SFs were frequently observed in (111) Cu/Co. t in (111) Cu/Co 1 nm is ~ 1 nm, compared to t of ~ 6 nm in (111) Cu/Ni 1 nm multilayers [80]. These ultra-fine twins with smaller average twin spacing in Cu/Co provide extra hardening to the system, making its peak hardness comparable to that of Cu/Ni with similar h. MD simulations have shown that twin interfaces are effective barriers to the transmission of dislocations.

In Cu/Ni system for instance, a resolved shear stress of ~ 0.8 GPa is necessary for dislocations to penetrate layer interfaces [31]. In Ni, a resolved shear stress on the order of 1.7-3 GPa is required for dislocation to propagate across a coherent twin boundary [91, 157]. These nanotwins can compensate softening that is typically observed in fully coherent system. Additionally the coexistence of FCC and HCP Co in (111) Cu/Co 5 nm films may also increase the barrier resistance to the propagation of dislocations.

IV.6 Conclusion

Highly (100) and (111) textured Cu/Co multilayers with various individual layer thicknesses were synthesized by magnetron sputtering. In (100) textured systems, Co has primarily FCC structure, whereas in (111) texture system, Co has a mixture of FCC and HCP phase at large layer thickness and becomes FCC when $h < 2$ nm. Layer thickness dependent of parallel and inclined planer defect such as SFs and twins were observed in multilayers. Size dependent strengthening mechanisms in Cu/Co and Cu/Ni systems are closely tied to their microstructures.

(1) When $h > 50$ nm, the (100) Cu/Co multilayers have greater hardness than those of (100) Cu/Ni presumably due to the formation of extremely high density of inclined SFs in Co.

(2) When h is a few nanometers, the peak strength of (100) Cu/Co system is lower than that of (100) Cu/Ni. As both systems have nearly epitaxial microstructure, similar lattice mismatch and elastic modulus mismatch, the large difference in their peak strength implies that the interface barrier resistance to transmission of partials in Cu/Co may be lower than interface resistance to perfect dislocations in Cu/Ni system. Thus we

hypothesize the difference in SFE between layer constituents could contribute significantly to strengthening of multilayers.

(3) In (111) textured systems the peak strength of Cu/Co and Cu/Ni systems is very close to each other with the existence of a similarly high density of SFs and nanotwins in both systems.

CHAPTER V

A NEW METHOD FOR RELIABLE DETERMINATION OF STRAIN-RATE SENSITIVITY OF LOW-DIMENSIONAL METALLIC MATERIALS BY USING NANOINDENTATION*

V.1 Overview

Nanoindentation technique is increasingly used to determine the strain rate sensitivity (SRS) of materials with small volumes, such as nanocrystalline metallic thin films. However traditional data analysis yields large scattering and uncertainty due to the influence of thermal drift on displacements measured at low strain rates. In the present work, we use a new method that renders hardness insensitive to thermal drift. The method involves (a) directly measuring contact stiffness by means of a small dynamic oscillation and (b) calculating contact area from the measured contact stiffness and the elastic modulus, which is insensitive to strain rate. The new technique is validated on nanocrystalline Ni and nanotwinned Cu films and returns expected values of SRS.

---

*This chapter reprinted with permission from "A new method for reliable determination of strain-rate sensitivity of low-dimensional metallic materials by using nanoindentation" by Y. Liu, J. Hay, H. Wang, X. Zhang; 2014. *Scripta Materialia*, Volume 77, Page 5-8, Copyright 2014 by Elsevier [158]

V.2 Introduction

Strain-rate sensitivity (SRS) is an important material property to understand thermally activated plastic deformation in metallic materials under a certain applied stress, such as creep. In general, a high value of SRS typically implies enhanced ductility or deformability. For most metals, the value of SRS is in the range of 0.005-0.05 [102]. In certain materials that manifest superplasticity, SRS values in the range of 0.33 or greater has been observed [159-161]. For metals with face-centered-cubic (fcc) structure, SRS typically increases with decreasing grain sizes, whereas the opposite holds for metals with body-centered-cubic (bcc) structure [102]. The dislocation-mediated plastic deformation of metals is a thermally assisted process, wherein the strain rate ($\dot{\varepsilon}$) and steady-state creep rate ($\dot{\varepsilon}_c$) are expressed as [100, 101]

$$\text{Equation 46} \quad \dot{\boldsymbol{\varepsilon}}_{\boldsymbol{c}} = \boldsymbol{A}\,\mathbf{exp}\left(-\frac{\boldsymbol{Q_c}}{\boldsymbol{kT}}\right)\boldsymbol{\sigma}^{\boldsymbol{n}}, \text{ and}$$

$$\text{Equation 47} \quad \dot{\boldsymbol{\varepsilon}} = \boldsymbol{B}\,\mathbf{exp}\left(-\frac{\boldsymbol{\Delta G}}{\boldsymbol{kT}}\right)\boldsymbol{\sigma},$$

respectively, where, *A* and *B* are constants which depend largely on microstructure, $\boldsymbol{\sigma}$ is the applied uniaxial stress, $\boldsymbol{n}$ is the stress exponent, $\boldsymbol{Q_c}$is the activation energy for creep, $\boldsymbol{\Delta G}$ is the activation energy for the rate-controlling process, $\boldsymbol{k}$ is the Boltzmann constant and $\boldsymbol{T}$ is the absolute temperature.

The value of SRS, *m*, is defined as

$$\text{Equation 48} \quad \boldsymbol{m} = \left(\frac{\boldsymbol{\partial ln\sigma}}{\boldsymbol{\partial ln\dot{\varepsilon}}}\right).$$

In turn, the stress-driven dislocation activation volume, $\boldsymbol{v}^*$, is calculated as

$$\text{Equation 49} \quad \boldsymbol{v}^* = -\frac{\boldsymbol{d(\Delta G)}}{\boldsymbol{\tau}} = \frac{\boldsymbol{\sqrt{3}kT}}{\boldsymbol{\sigma}}\left(\frac{\boldsymbol{\partial ln\dot{\varepsilon}}}{\boldsymbol{\partial ln\sigma}}\right) = \frac{\boldsymbol{\sqrt{3}kT}}{\boldsymbol{\sigma m}}$$

where τ is the shear stress ($\boldsymbol{\tau = \sigma/\sqrt{3}}$).

For bulk metallic materials, values of SRS (m) and stress exponent (n) are typically determined by means of uniaxial tension [162-167] or compression tests [168, 169] on samples with uniform cross section. Tensile strain-rate-jump tests are frequently applied to determine m values by switching strain rates instantaneously during a single tensile test [170-173]. Recently significant interest arises to determine m values for nanocrystalline (nc) metallic materials. As a majority of these materials have low dimensions in form of thin foils or very often thin films, there is an increasing need to accurately determine m value by using a reliable technique. Under this context, nanoindentation is the best way to evaluate SRS (m) [174-176]. In a nanoindentation experiment, the strain rate ($\dot{\varepsilon}_i$) is defined as the indenter displacement rate ($\dot{h}$) divided by the displacement of the indenter into the surface (h) [177]:

$$\text{Equation 50} \quad \dot{\boldsymbol{\varepsilon}}_{\boldsymbol{i}} = \frac{\dot{\boldsymbol{h}}}{\boldsymbol{h}}.$$

Under many practical circumstances, $\dot{\boldsymbol{\varepsilon}}_{\boldsymbol{i}}$ may also be expressed in terms of the applied indentation force rate ($\dot{\boldsymbol{P}}$) and the indentation force ($\boldsymbol{P}$) [178]

$$\text{Equation 51} \quad \dot{\boldsymbol{\varepsilon}}_{\boldsymbol{i}} = \frac{\dot{\boldsymbol{P}}}{\boldsymbol{P}},$$

which is experimentally advantageous for nanoindentation systems that are fundamentally force-controlled.

"Conventional" method to determine SRS by nanoindentation was developed by Lucas and Oliver, who measured hardness at a series of constant strain rates. [178]. Their method works well for moderate-to-high strain rates, but faces experimental difficulties at low strain rates, because the measured indenter displacement tends to be substantially affected by thermal drift. Normal procedures for accounting and compensating for

thermal drift are inappropriate for materials which creep over a long period of test time at low strain rates [121, 179].

To mitigate the thermal drift problem, Maier et al. proposed an indentation strain-rate-jump test for measuring *m* [176]. In this method, the strain rate is abruptly changed for several times as the indenter proceeds into the material, and the value of hardness at each new strain rate is recorded in order to determine *m*. The influence of thermal drift is alleviated by applying the highest strain rates first and the lowest strain rates last (when the indentation displacement is large). This method has been applied to ultra-fine grained aluminum and nanocrystalline nickel. But this technique, in general, requires a minimum accumulative indentation depth of 500 nm or greater. Thus it is not appropriate for thin metal films with a total thickness of 1-2 μm, where the maximum indentation depth must be limited to 200-300 nm to avoid substrate effects. Recently, Maier et al. resurrected an alternate technique for accurately measuring creep properties at very low strain rates [180]. The technique was first proposed by Weihs and Pethica [181], but never substantially developed. It involves measuring contact stiffness by dynamically oscillating the indenter and inferring the contact area from this contact stiffness.

In this study, we apply two analytical methods to determine SRS (*m*) of thin nanotwinned (nt) Cu and nc Ni films deposited on silicon. The conventional method (described by Lucas and Oliver) measures displacement directly, and our new method calculates displacement from continuous stiffness measured by nanoindentation. Mechanical properties, such as hardness and elastic modulus, calculated by the new method are consistent with literature values by significantly suppressing thermal drift induced uncertainty. Most notably, new method significantly reduces data scattering and

improve accuracy for the determination of SRS values as validated in nc Ni and nt Cu films. This simple new method significantly increases the fidelity of using nanoindentation technique to determine mechanical properties at low strain rate and acquire reliable SRS values for metallic materials in small dimensions in general.

V.3 Experimental

Two metallic films were tested in this study: epitaxial nt Cu and nc Ni (majority (111) texture) deposited on Si substrates by DC magnetron sputtering at room temperature. The thicknesses of Cu and Ni films were 1500 and 800 nm, respectively. An Agilent G200 NanoIndenter with a Berkovich indenter tip was used for all tests. The continuous stiffness measurement (CSM) option was also used in order to continuously measure elastic contact stiffness, *S*, throughout the experiment [121, 179]. At least twelve tests were performed on each sample to a depth limit of 200 nm using three different strain rates: 0.05/sec, 0.01/sec. and 0.002/sec. The same test results are interpreted by conventional indentation analysis ("conventional") and the new method (referred to as "modified" hereafter). The average grain sizes of thin films were determined by transmission electron microscopy (TEM) experiments that were performed on a JEOL 2010 microscope operated at 200 kV.

V.4 Analysis

We now briefly explain the two analysis methods used for this study, conventional vs. modified methods, with the goal to highlight their major difference. Fig. 51 is a flowchart that illustrates the two analyses side by side. For both analyses,

Sneddon's stiffness equation [182] as commonly expressed for interpreting indentation data [121, 183] provides the foundational relationship between the reduced elastic modulus (E_r), contact stiffness (S) and contact area (A):

$$\text{Equation 52} \quad \boldsymbol{E_r = \frac{\sqrt{\pi}}{2}\frac{S}{\sqrt{A}}}$$

In turn, the reduced modulus depends on the elastic modulus and Poisson's ratio of sample (E, $\boldsymbol{\nu}$) and indenter (E_i, $\boldsymbol{\nu_i}$):

$$\text{Equation 53} \quad \boldsymbol{\frac{1}{E_r} = \frac{1-\nu^2}{E} + \frac{1-\nu_i^2}{E_i}}.$$

Further, both analyses define hardness (H) as load (P) divided by contact area (A):

$$\text{Equation 54} \quad \boldsymbol{H = P/A},$$

where P is indentation force.

The two analyses differ primarily in the way through which contact area is calculated. The conventional analysis uses the direct measurements of force (P), displacement (h), and contact stiffness (S) to determine contact area, A. First, the contact depth, h_c, is calculated as

$$\text{Equation 55} \quad \boldsymbol{h_c = h - 0.75P/S},$$

where the term $3P/(4S)$ expresses the deflection of the surface outside the contact area [121]. Then, contact area is calculated as an empirical function of contact depth:

$$\text{Equation 56} \quad \boldsymbol{A = m_0 h_c^2 + m_1 h_c},$$

where the values of $\boldsymbol{m_0}$ and $\boldsymbol{m_1}$ are determined through a calibration process that involves indenting a material of known elastic properties—typically fused silica [121].

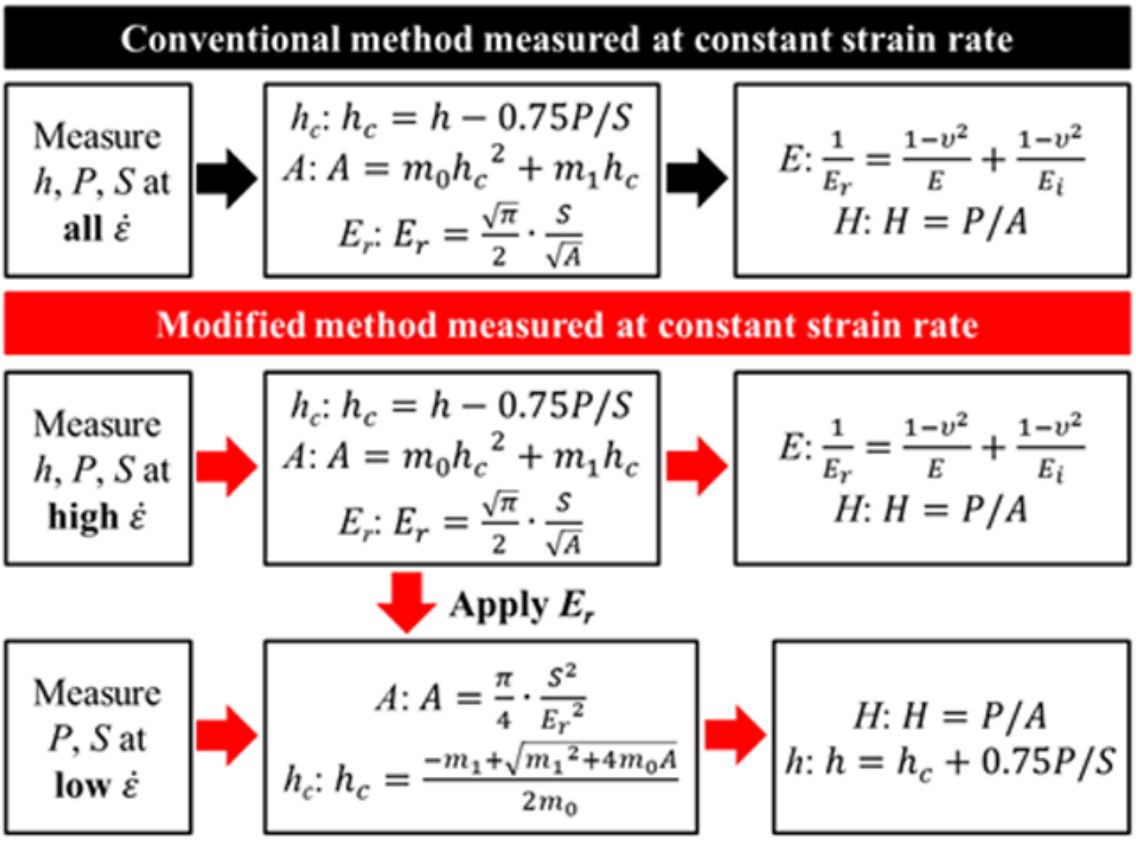

Figure 51 Flow charts explaining differences between conventional and modified analytical methods. (a) The conventional methodology that measures displacement (h), load (P), and contact stiffness (S) at different strain rate ($\dot{\boldsymbol{\varepsilon}}$). The contact depth ($h_c$), contact area ($A$), reduced elastic modulus (E_r), hardness (H), and sample modulus (E) can be derived. (b) The modified methodology firstly determines E_r at high $\dot{\boldsymbol{\varepsilon}}$, then applies E_r as known parameter to lower $\dot{\boldsymbol{\varepsilon}}$ measurement. The h measurement at low $\dot{\boldsymbol{\varepsilon}}$ can be calculated instead of direct measurement, in order to reduce the thermal drift effects on displacement measurement.

The modified analysis actually begins by executing the conventional analysis for indentation data acquired at a high strain rate (as shown in Fig. 51) in order to achieve an accurate measure of reduced modulus by means of Eqs. 7, 10, and 11. But for lower strain rates, the directly measured displacements are presumed to be inaccurate due to thermal drift. However, the direct measurements of force and stiffness remain valid and can be used to calculate contact area by rearranging Equation 7 as

Equation 57 $$\boldsymbol{A = \frac{\pi}{4}\frac{S^2}{E_r^2}},$$

where E_r is the value of reduced modulus calculated at a high strain rate according to conventional analysis. The modified analysis calculates contact depth by inverting Equation 11:

Equation 58 $$\boldsymbol{h_c = \frac{-m_1+\sqrt{m_1^2+4m_0A}}{2m_0}},$$

where A can be determined from Equation 12. Finally, the modified analysis calculates the indenter displacement (the direct measurement of which was erroneous at low strain rate or over a prolonged period of time) as

Equation 59 $$\boldsymbol{h = h_c + 0.75P/S},$$

where h_c is that determined by Equation 13. At this point, we note that the calculations of contact depth and displacement according to Eqs. 13 and 14 are not strictly necessary, because Equation 12 provides the only missing piece for determining reduced modulus and hardness by Eqs. 7 and 9 when displacement is not reliable. However, displacement calculated according to Equation 14 is useful for presenting data and controlling the real-time progress of the physical nanoindentation test. For example, we terminated the loading process when the displacements *as calculated by Equation 14* reach our target displacement of 200nm.

It is clear from the above "modified" analysis that the dynamic measurement of stiffness by oscillating the indenter is an essential aspect of this method as contact stiffness is barely affected by thermal drift. Without this oscillation, there would be no instantaneous measurement of stiffness, and thus no reliable determination of contact area or hardness.

V.5 Results

In order to validate this modified method, we selected two systems, nt Cu and nc Ni with a respective total film thickness of 1500 and 800 nm prepared by magnetron sputtering. The plan-view TEM micrograph of the nc Ni in Fig. 52a shows numerous grains and the statistical grain size distribution analysis yields an average grain size of ~54 nm. The inserted selected diffraction (SAD) pattern displays a strong (111) texture of the film. The plan-view TEM micrograph of the nt Cu film and corresponding SAD pattern in Fig. 52b present an epitaxial (111) single-crystal-like film with a number of grains, and the average grain size (shown from the underneath grain size distribution chart) is ~ 68 nm. A cross-section TEM micrograph (Fig. 52c) of the same Cu specimen (examined along Cu <110> zone axis) shows the epitaxial (111) Cu film contains an extremely high density of nanotwins. The average twin spacing is ~ 10 nm.

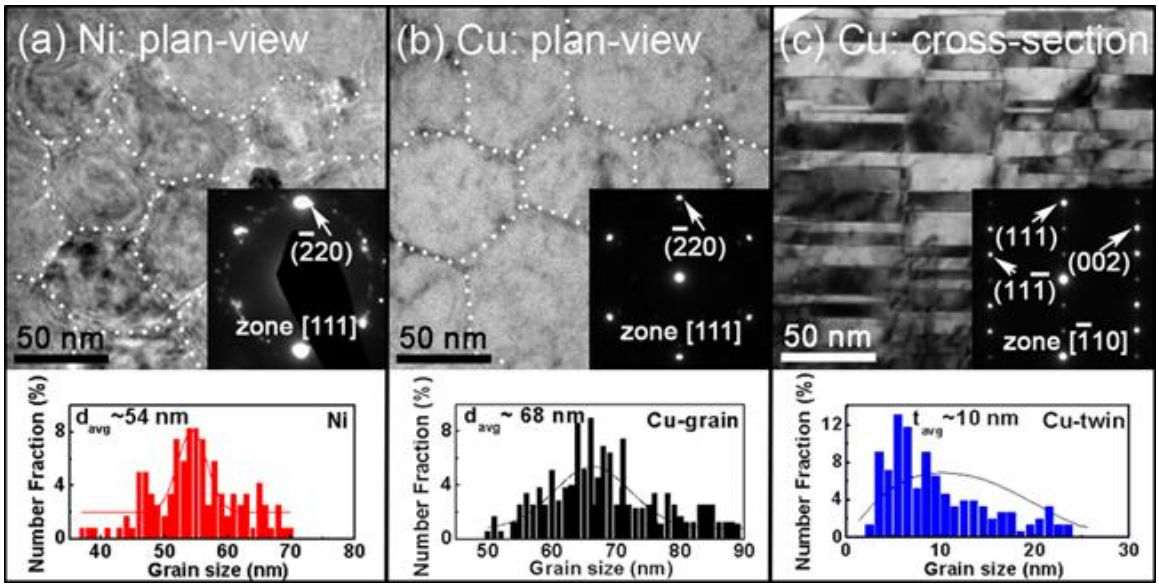

Figure 52 Plan-view TEM micrographs of (a) sputter-deposited nanocrystalline (nc) Ni (111) and (b) epitaxial nanotwinned (nt) Cu (111) films. Statistical analysis shows that the average grain size d_{ave} for nc Ni is ~54 nm, and the d_{ave} for nt Cu is ~68 nm. (c) Cross-section TEM micrograph of the epitaxial nt Cu displays high density growth twins with an average twin spacing of ~ 10 nm as evidenced by the corresponding statistical study.

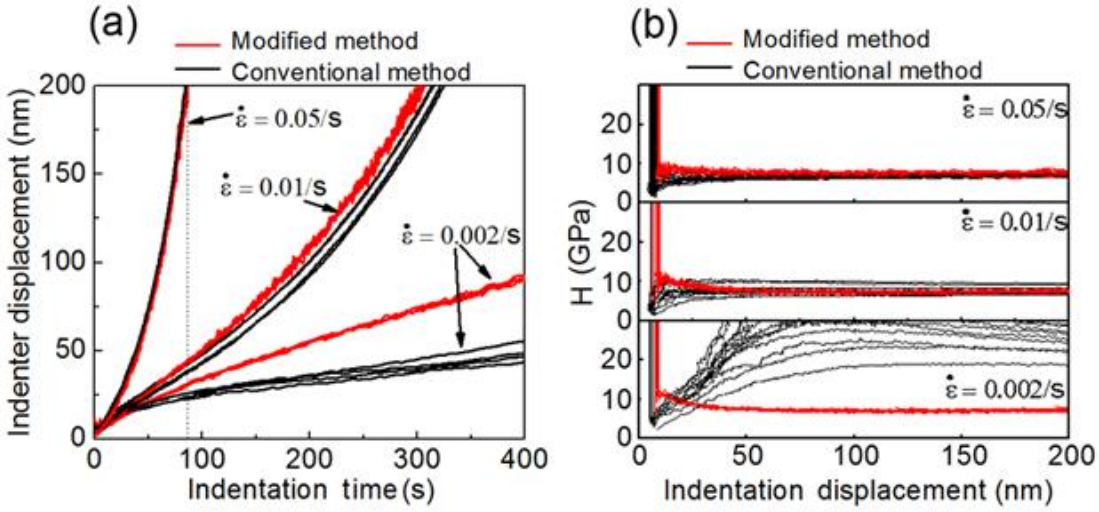

Figure 53 Comparison of nanoindentation results obtained from conventional (black) and modified (red) analytical methods using the same sets of indentation data on nc Ni film. (a) Displacement vs. indentation time obtained at strain rates of 0.002, 0.01, and 0.05/s. The conventional technique has substantial scattering at lower strain rate, whereas the modified method leads to tight convergence of different sets of data. (b) Calculated indentation hardness (H) vs. displacement plotted at different strain rate. At a high strain rate (0.05/s), the indentation hardnesses calculated from both techniques are similar. However at low strain rate (0.01/s), the conventional analysis leads to prominent scattering in hardness, and unacceptable results at a lower strain rate 0.002/s. In comparison, convergent and consistent hardness results were obtained from the modified method. (For interpretation of the colored figure legend, the reader is referred to the web version of this article).

In Fig. 53, we compare the nanoindentation results at various strain rates obtained by using two different analytical methods from the same sets of indentation result on nc Ni film. As shown in the indentation displacement vs. time plots in Fig. 53a, obtained at strain rates of 0.002, 0.01, and 0.05/s, the conventional technique has substantial scattering at lower strain rate, whereas the modified method leads to tight convergence of different sets of data at all strain rates. The calculated indentation hardness vs. indentation displacement in Fig. 53b exhibits the following characteristics. First the indentation hardnesses calculated from both techniques are similar at a high strain rate

(0.05/s), ~ 7.5 GPa. Second, at the intermediate strain rate (0.01/s), the conventional analysis (black traces) leads to prominent scattering in hardness, 7.9 ± 1 GPa, in comparison to 7.4 ± 0.1 GPa obtained from the modified method (red traces). Third, when a lower strain rate 0.002/s was applied, significant scattering results in unacceptable hardness, 22 ± 7 GPa obtained from the conventional method. Conversely, the hardness results derived from modified method has substantially improved convergence and reliability, 7.2 ± 0.1 GPa. Finally, the values of *E* determined by conventional method at low strain rate (0.002/s) is unreliable, ~ 500 GPa, comparing to the bulk (literature) value of 220 GPa for Ni. Table 7 summarizes the values of hardness and elastic modulus of Ni and Cu determined from two different techniques.

Table 7 Comparison of mechanical properties of nt Cu and nc Ni determined from the conventional and modified methods by using the same sets of data.

nt Cu	**Conventional method**		**Modified method**	
	Modulus (GPa)	**Hardness (GPa)**	**Modulus (GPa)**	**Hardness (GPa)**
$\dot{\varepsilon}$ **= 0.05 /s**	157 ± 4	2.35 ± 0.06	157±4	2.33 ± 0.04
$\dot{\varepsilon}$ **= 0.01 /s**	149 ± 6	2.03 ± 0.13	157±4	2.22 ± 0.04
$\dot{\varepsilon}$ **= 0.002 /s**	190 ± 27	3.06 ± 0.70	157±4	2.19 ± 0.04

nc Ni	**Conventional method**		**Modified method**	
	Modulus (GPa)	**Hardness (GPa)**	**Modulus (GPa)**	**Hardness (GPa)**
$\dot{\varepsilon}$ **= 0.05 /s**	220 ± 5	7.55 + 0.18	220 ± 5	7.51 ± 0.15
$\dot{\varepsilon}$**=0.01 /s**	233 ± 11	7.89 ± 0.94	220 ± 5	7.37 ± 0.06
$\dot{\varepsilon}$**=0.002 /s**	494 ± 54	25.25 ± 4.21	220 ± 5	7.19 ± 0.07

Fig. 54 compares the SRS values calculated from strain-rate-dependent hardness values obtained by the two different analytical methods for nt Cu and nc Ni films. The conventional analysis (open squares) yields erroneous results, as indicated by negative large SRS values for both specimens. However, the modified method (solid circles) yields a reasonable positive SRS value for nc Ni: $m = 0.016 \pm 0.002$ (Fig. 54a), and for nt Cu: $m = 0.020 \pm 0.002$ (shown in Fig. 54b). We will compare these results with those reported in literature in the next section.

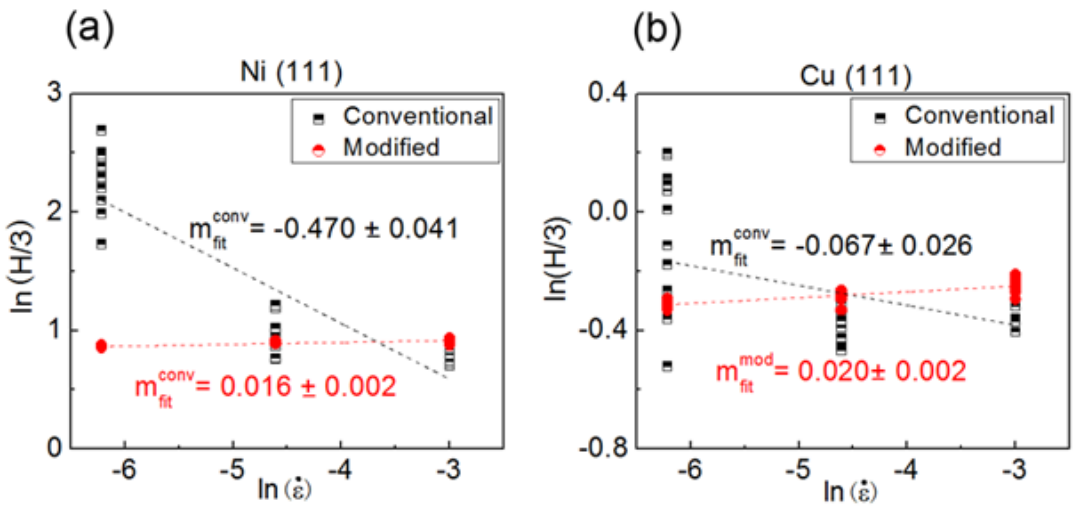

Figure 54 Comparison of strain-rate sensitivity (SRS) calculated from two methods for nt Cu and nc Ni films as examples. SRS is calculated from the slope of *ln (H/3)* vs. *ln* $(\dot{\varepsilon})$ plots. The conventional analysis (half-filled black squares) yields erroneous results, as indicated by a negative SRS values. In contrast, the modified method (shown by solid red circles) produces a reliable positive SRS value: $m = 0.016 \pm 0.002$ for nc Ni and $m = 0.020 \pm 0.002$ for nt Cu.

V.6 Discussion

V.6.1 Advantage of the Modified Technique over Conventional Method

The key difference between modified and conventional method lies in the determination of contact area. In the conventional method, contact area is calculated based on direct measurement of indenter displacement and the indenter geometry. This technique is widely adopted to determine hardness and elastic modulus of thin films. A majority of measurements that yield consistent results were performed at an intermediate-to-high strain rate, 0.01-0.05/s or greater. Such strain rates are typically recommended by the manufacturer to reduce indentation time (for practical applications), and more importantly to minimize the impact of thermal drift. Although modern technologies enable substantial thermal-drift mitigation, such techniques are not appropriate for materials which manifest substantial creep. Thus, thermal drift is significant when specimens are tested at low strain rates in an attempt to determine, for instance, strain-rate sensitivity. The net effect of thermal drift is inaccurate measurements of hardness and Young's modulus. As shown in Fig. 53 and Table 7, the hardness values of nc Ni exceeds 20 GPa, and elastic modulus reaches a bizarre value of 500 GPa.

At low strain rate, to minimize the impact of thermal drift, we employ the modified method to analyze the same sets of indentation data. Here the directly measured indentation displacements are not used. Instead contact area is calculated directly based on directly measured contact stiffness and Elastic modulus, which was determined previously at high strain rate to avoid the adverse influence from thermal-drift. Such a simple strategy works exceptionally well. The modified method not only leads to convergence of scattered data (as shown by using the conventional technique), but also is

very practical, as the same sets of data can be used without the need for significant modification of instrumentation and indentation method.

V.6.2 Grain Size Dependent SRS Values in nc Metals – Validation of the Modified Methodology

In order to validate this modified method, we compare our SRS results to values obtained by generally accepted techniques, such as uniaxial tensile, compression, or indentation jump test for bulk specimens and in some cases, thin films. A comprehensive plot of *m* vs grain size was used because there is increasing evidence that *m* is grain-size dependent. In this study, the average grain size is determined to be ~ 55 and ~ 70 nm in nc Ni and nt Cu, respectively. Compiled plots for the *m* values for specimens tested by uniaxial tension, compression, and indentation jump test [164-167, 170, 172, 176, 184-191] are shown in Fig. 55 for Ni and Cu, respectively. It is evident that the results obtained from the modified method (solid circle) agree well with the general trend reported in the literature, whereas the results from conventional analytical method (solid squares) is radically different from previous studies due primarily to significant thermal drift at low strain rates. The consistency of results produced by modified analytical method thus lends confidence on the reliability and accuracy of this new method.

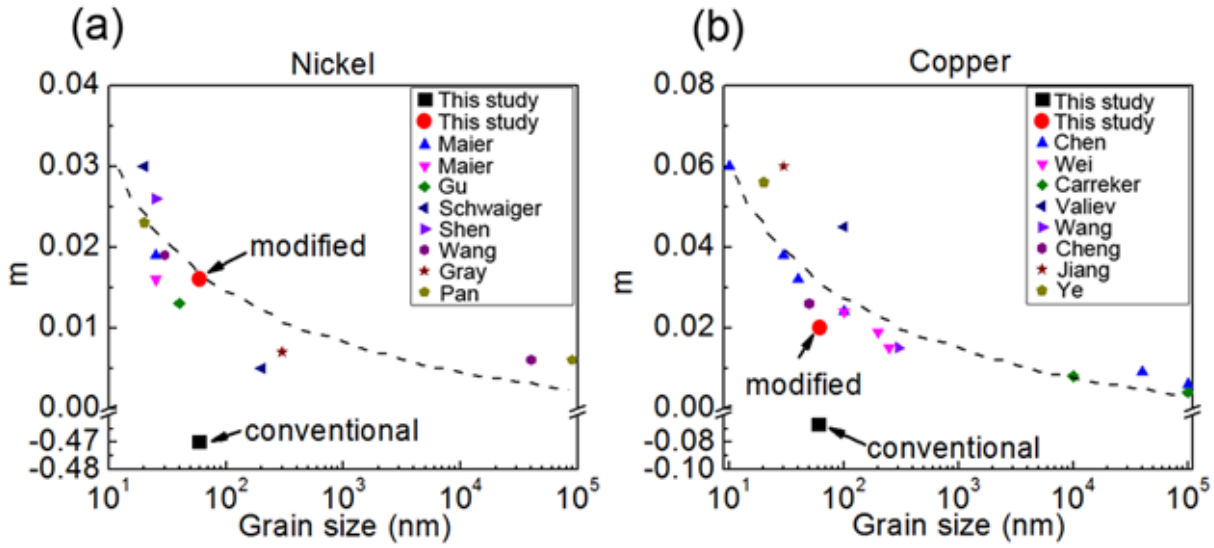

Figure 55 Compiled plots of the SRS values (m) vs. grain sizes obtained from various techniques, including indentation jump, tensile and compression tests for (a) Ni and (b) Cu. The results obtained from the modified analysis technique are consistent with the general trend reported in literature, whereas the results from conventional analytical method are radically different from previous studies due primarily to significant thermal drift of specimens at low strain rate.

The dependence of *m* values on grain size has been well studied in the literature. In general for monolithic metals with fcc structure, the *m* value is typically found to increase with decreasing grain sizes, whereas the opposite holds true for metals with bcc structure [102]. For nc and ultra-fined grained fcc metals, the SRS can de described by [102]

Equation 60 $$\boldsymbol{m = \frac{kT}{\xi b} \cdot \frac{1}{\chi(\alpha \mu b\sqrt{\rho} d)+\beta\sqrt{d}}},$$

where $\boldsymbol{\xi}$ is the distance swept out by a glide dislocation during a activation event, *b* is the magnitude of theBurgers vector, $\boldsymbol{\mu}$ is the shear modulus, *d* is the grain size, α, β, χ, are proportional factors. It follows that qualitatively, *m* will increase with decreasing grain sizes for nc and ultra-fine grained metals. We also notice that the *m* value for nt Cu is ~

0.02, consistent with what has been reported in the literature. The activation volume $\boldsymbol{v}^*$ can be described by [192]

Equation 61 $$\boldsymbol{v}^* = \boldsymbol{b} \cdot \boldsymbol{\xi} \cdot \boldsymbol{l}^*$$

where l^* is the length of dislocation segment involved in thermal activation. For nc, or ultra-fine grained metals, l^* can be described by [166]

Equation 62 $$\boldsymbol{l}^* = \boldsymbol{\chi d}$$

For nt Cu, although the average twin spacing is smaller than d, there remains abundant dislocation activities within twins. As revealed by *in situ* nanoindentation studies on nt Cu, dislocations, such as Shockley partials, can propagate along twin boundaries until they encounter grain boundaries [53, 54]. Hence, the average grain size may remain the deterministic dimension for m value in this sputtered nt Cu film.

V.7 Conclusion

We developed a modified method for reliable determination of SRS values of thin metal films. The analysis overcomes thermal-drift problems associated with long testing times at low strain rates. In particular the modified analysis does not use the directly measured indentation depth, which is increasingly erroneous as strain rate decreases. Instead the modified analysis uses the elastic modulus (measured at a relatively high strain rate) to reliably calculate contact area. The modified analysis circumvents the influence of thermal drift, and correctly returns accurate hardness, which in turn, leads to accurate values of SRS. The SRS values we obtained for nc Ni and nt Cu, agree well with the values obtained from tensile tests.

CHAPTER VI

DISLOCATION AND TWIN BOUNDARY INTERACTION IN EPITAXIAL NANOTWINNED CU BY *IN SITU* NANOINDENTATION STUDIES

VI.1 Overview

In this letter, we report the first *in situ* evidence to identify the phenomenon and corresponding stress level of incoherent twin boundary (ITB) migration; dislocation nucleation; and dislocation penetration through coherent twin boundary (CTB) in one loading event on epitaxial nanotwinned Cu. We have observed the detwinning process triggered at ultra-low indentation stress level associate with stress plateau and drops before plastic yielding. We found that ITB migration of the thinner twin (~ 5 nm) occurs at very low stress at 0.1 GPa with about 15 nm/s velocity, whereas the thicker twin (~14 nm) can stand until 0.6 GPa. Furthermore, we have captured dislocation nucleation and propagation before macroscopic yielding, which corresponds to dislocation penetration through twin boundaries.

VI.2 Introduction

Nanocrystalline (nc) metals have been well known of the great strengthening because of the resistance of grain boundaries to the transmission of dislocations [4-6, 124, 193]. Similarly, nanotwinned (nt) metals exhibit the high strength as well due to (111) coherent twin boundaries (CTB) can provide great strengthening by resisting dislocation slip transfers[55-60]. Furthermore, nt materials show better ductility[51, 61, 62], thermal stability[63-65], creep and fatigue resistance[66-68], and electrical resistance[50, 69, 70] compare to nc metals. Both experimental and simulation studies have contributed the insight of the dislocation interaction with CTB on the mechanisms, kinetics and energetics of dislocations transmit across the CTB[91, 194-197]. Therefore, it is reasonable to speculate that materials performance can be further improved by increase the CTB density, or decrease the average twin spacing.

However, recent studies revealed that twin is less stable when the average twin spacing is a few nanometers. Lu et al., reported that electro-deposited nt Cu reaches its maximum strength with average twin spacing ~ 15 nm, not ~ 4 nm[51]. Anderoglu et al., revealed that most of fine twins (~ 5 nm spacing) are removed after plastic rolling on sputtered nt Cu foil[52]. The recent studies on (112) incoherent twin boundaries (ITB) have shown that ITB can migrate or slide during interaction with the dislocations[47, 54, 198, 199], which may lead to the removal of the CTB, so called detwinning. Particularly, Wang et al., found in both experiment and molecular dynamics (MD) simulation, that ITB has more tendency to migrate in thinner twins[200]. Another detwinning mechanism has been reported by Li et al.,[53] and Zhu el al.,[201] in 2011 that partial or perfect dislocation could interact with twin dislocations and trigger the detwinning process.

Since there are few studies on combining stress and microstructural analysis, some major issues remain poorly understood: (1) what is the stress level when ITB migrate? (2) what is the stress level when dislocation interact with CTB? (3) does load drops occur at these events? Techniques such as *in situ* deformation in a transmission electron microscopy (TEM) can be used to directly quantify the microstructure-stress relationship [113-115, 117].

In this letter, *in situ* nanoindentation is performed on epitaxial nanotwinned Cu along <111> direction (perpendicular to coherent (111) twin boundary). We report the first *in situ* evidence to identify the phenomenon and corresponding stress level of ITB migration; dislocation nucleation; and dislocation penetration into CTB in one loading event. We also observed the indentation stress drops associate with detwinning process, and dislocation penetration process evident by *in situ* nanoindentation. Furthermore, we found that detwinning is layer thickness dependent by comparing the performance between a 14 nm thick twin (T1) and a ~ 5nm fine twin (T2). The result show that the ITB migration of T2 occurs at very low stress with about 15 nm/s migration velocity, whereas T1 can stand even after plastic yielding.

VI.3 Experimental

Epitaxial (111) Cu films with 1.5 μm thickness were magnetron sputtered on HF etched Si (110) substrate[69]. The base pressure was 5×10^{-8} torr. The deposition rate was about 5 $\dot{A}$/s. *In situ* nanoindentation was performed by using a special holder manufactured by NanoFactory Inc. *In situ* TEM analyses were conducted within a JEOL 2010 TEM with a point-to-point resolution of 0.23 nm. During *in situ* nanoindentation, a

wedge shape nanoindentor tip was used with known geometry. Alternatively we used Hertzian spherical contact estimation on true stress, marked as indentation stress at here, based on TEM observation of the contact geometry [123]. TEM foil thickness was ~ 30 nm, measured by using conventional convergent beam electron diffraction (CBED) technique.

VI.4 Results

Fig. 56a shows the indentation stress vs. displacement (and time) with loading (red, color online) and unloading (blue color online) curve. Before 20s, a clear stress plateau along with the stress drop was observed between 8s ~ 17s, which reveals ITB migration as shown in Fig. 57. The yield strength is 0.5 GPa at 31 s, which is also confirmed by bright field (BF) TEM snapshots in Fig. 58 where the dislocations nucleate. The detail of two load drops in plastic regime (30 ~ 53s) will discuss in Fig. 58 when dislocation propagate and penetrate through CTBs. Based on Hertzian spherical contact estimation, the strain is proportional of calculated contact area/ tip radius. Therefore, the work hardening exponent can be roughly estimated qualitatively. As shown in Fig. 56b, stress-strain behaviors of nt Cu exhibits the similar elastic modulus (slope) but much higher yield strength compare with Cu without twins. Furthermore, work hardening exponent of nt Cu at different sections (n_1 and n_2) are smaller than no twin Cu (n_0).

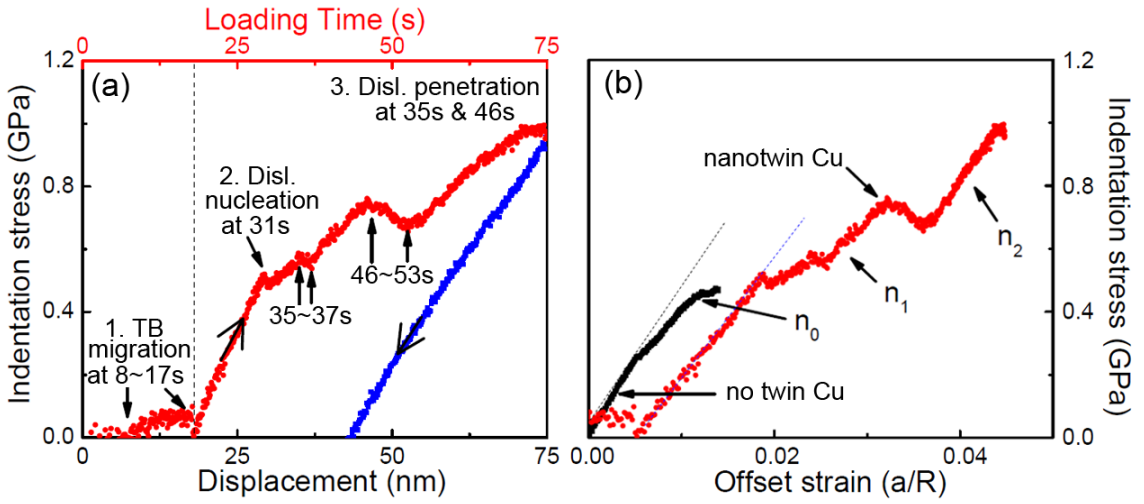

Figure 56 *In situ* nanoindentation study that shows the elastic and plastic deformation of epitaxial nanotwinned (nt) Cu indented along <111> direction. (a) Indentation stress vs. displacement plots during loading (red, color online) and unloading (blue color online) process. A clear stress plateau along with the stress drop was observed between 8s ~ 17s. Yielding occurred at 31 s (0.5 GPa). A prominent load drop event was also observed (46-53 s). (b) Comparison of stress-strain behavior between Cu without twins and nt Cu. Work hardening exponent n_0, n_1 and n_2 are labeled at different sections. Hertzian spherical contact was used to estimate strain.

Fig. 57 presents sequential *in situ* TEM snapshots that the ITB migrates along with stress plateau and stress drop corresponding 8-17s in Fig. 56 (see suppl. video 1 for detail). Two nanotwins (marked as T1 and T2) are focused with thickness 14 nm and 5 nm, respectively. A clear ITB is marked as dash line in (b), and the rest as reference. During deformation, thinner twin (T2) migrates from 12s to 13s, and 16s to 17s. The two migration distance is both 15 nm. Thus, the migration speed is estimated as 15nm/s.

Fig. 58 shows the sequential *in situ* TEM snapshots that reveal the dislocation nucleation and penetration corresponding to yielding and two stresses drops from 29 to 53s in work-hardening regime as indicated in Fig. 56 (see suppl. video 2 for detail). As shown in a-c from 29s to 31s, dislocations start nucleating and the density increase rapidly leads to the on-site yielding at 31s. As shown in d-f, dislocations network

propagates and expands quickly that result in another load drop at 35-37s. After that, the work-hardening are majority contributed by the interaction between CTB and dislocations. As shown in g-i, via dislocation penetration of CTB, the large load drop occurs from 46s to 53s as shown in Fig. 56.

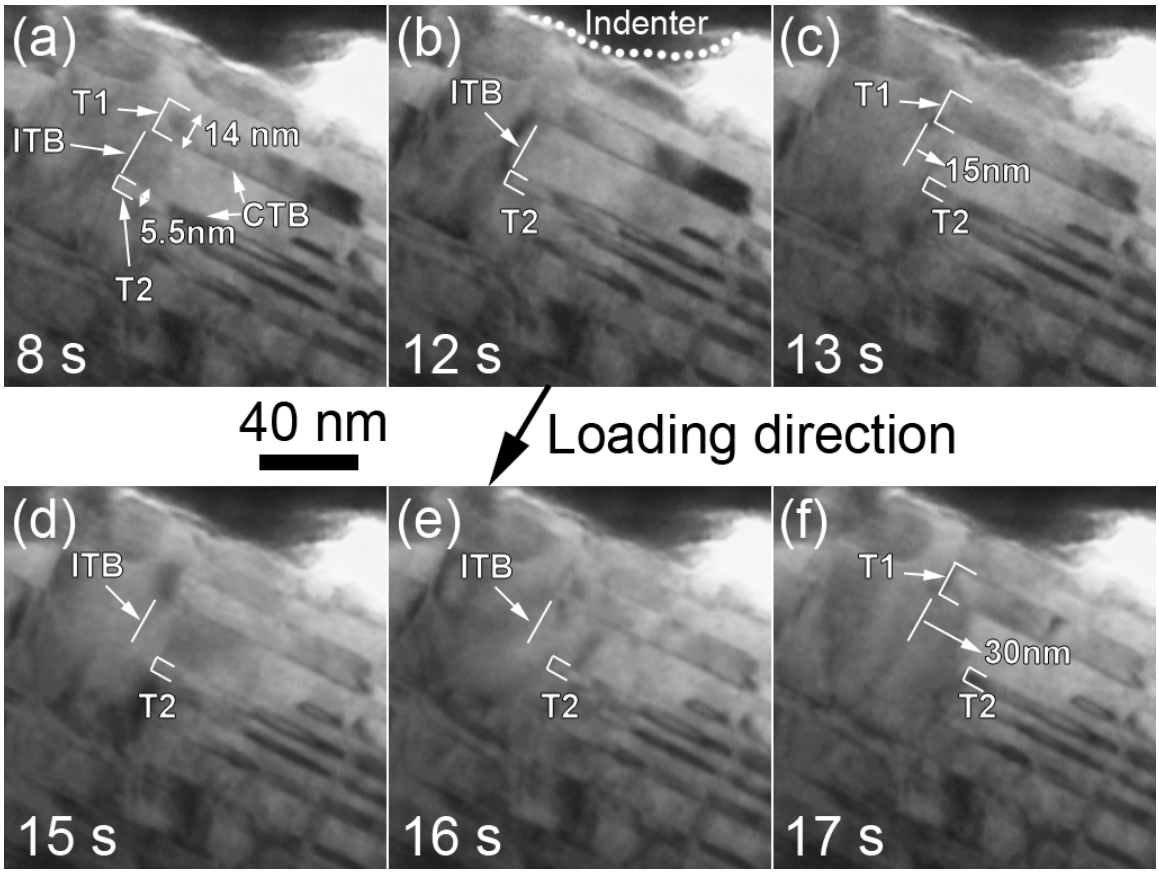

Figure 57 Sequential *in situ* TEM snapshots revealing the migration of incoherent twin boundary (ITB) during 8-17 s, corresponding to stress plateau in the ultra-low stress regime as indicated in Fig. 56 (see Suppl. video 1 for detail). (a) Two nanotwins, T1 and T2, were identified with thickness 14 and 5 nm, respectively. (b) A dotted line that marked at the ITB location was highlighted as a reference after 12 s. (c) By 13 s, during deformation, the thinner twin T2 migrated by 15 nm. Continuous deformation did not lead to obvious ITB migration in (d-e) during 15-16 s, until at 17 s (f) another prominent ITB migration event by 15 nm was captured. The peripheral of indenter tip is marked in (b).

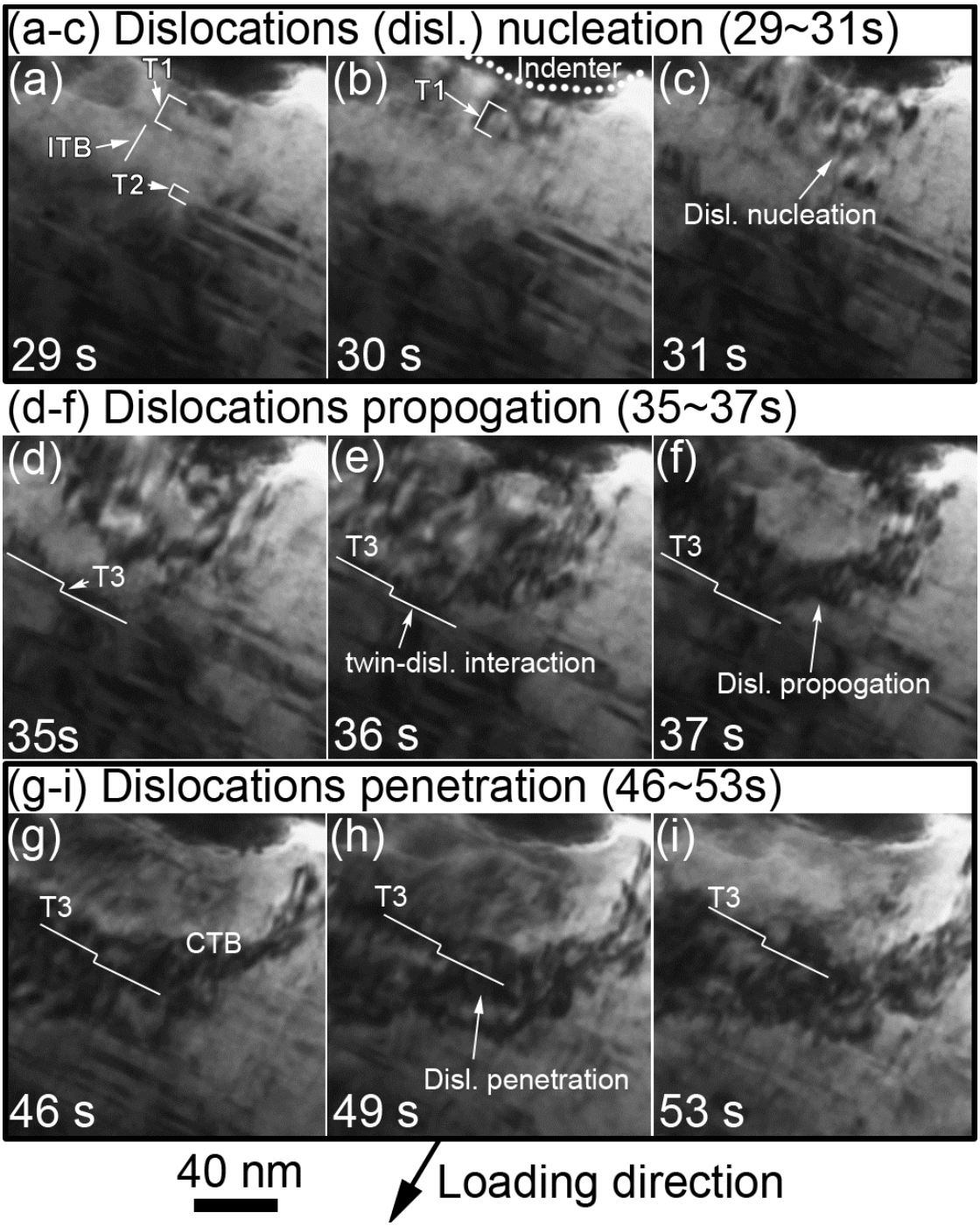

Figure 58 Sequential *in situ* TEM snapshots reveal the dislocation nucleation and penetration corresponding to stresses drops indicated in Fig. 56 (see Suppl. video 2 for detail). As shown in (b), dislocations started to nucleate at 30 s, and a substantial nucleation of multiple dislocations was captured at 31 s (c) corresponding to the load drop at 31s in Fig. 56. (d-f) During 35-37s, the group of dislocations propagated rapidly towards T3. The migration of dislocations was hindered by TBs at T3. Simultaneously a large dislocation loop consisting of a band of dislocations formed along the TBs. (g-i) During 46-53 s, the band of dislocations penetrated through TBs, corresponding to the large load drip revealed in Fig. 56.

VI.5 Discussion

In order to better understand the phenomenon. A schematic of the phenomenon and the stress level of the ITB migration; dislocation nucleation; and dislocation penetration into twin boundaries is shown in Fig. 59. ITB migration of the fine nanotwins occurs at very low stress level (~ 0.1 GPa) before yielding. There is no evidence of ITB migration of the thick nanotwins prior to dislocation nucleation (~0.5 GPa). Once dislocation networks form, they will then interact with twin boundaries and penetrates through CTBs at higher stress level (0.6-0.8 GPa).

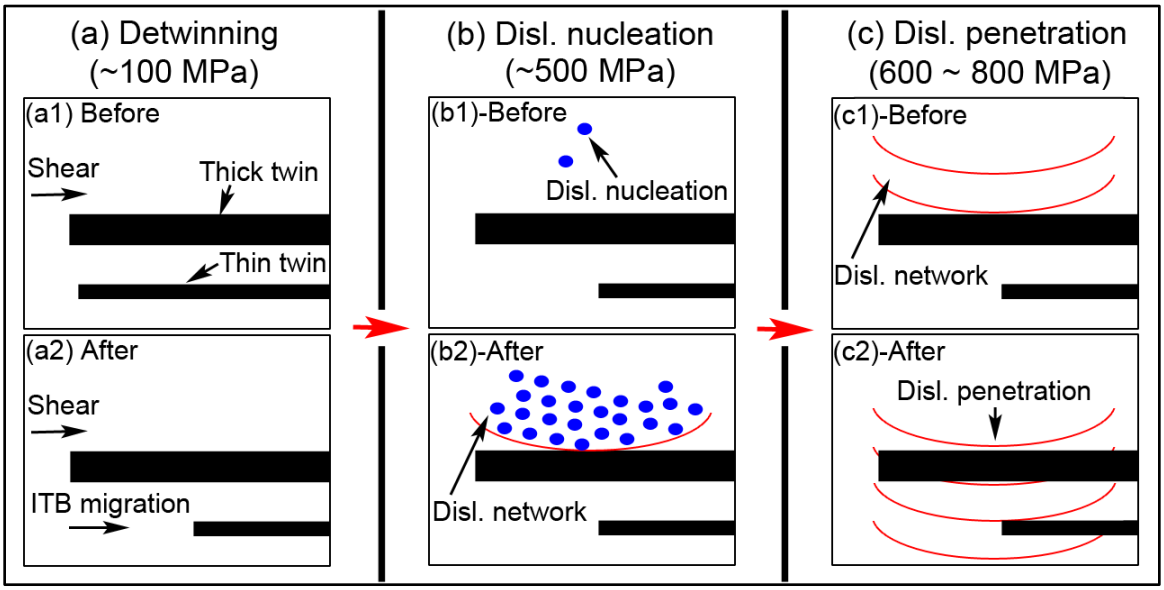

Figure 59 Schematic of stress induced evolution of microstructures during *in situ* nanoindentation. Three distinct stages are identified: TB migration (detwinning), dislocation nucleation, and dislocation penetration across TBs. (a) ITB migration of the fine nanotwins occurs at very low stress level (~ 100 MPa) in the elastic regime. There is no evidence of ITB migration of the thick nanotwins prior to the onset of dislocation nucleation. (b) Dislocation nucleation occurs at ~ 500 MPa, dislocation networks are form when multiple dislocation combined together (c) Once dislocation networks form, they interact with TBs and penetrate TBs at higher stress level (600-800 MPa).

At first, we examined dislocation nucleate when indentation stress at 0.5 GPa in this study. Previous studies on tensile test of pure Cu with similar average twin thickness revealed yield strength from 0.5 to 0.6 GPa [51, 202]. Our indentation stress measurement and tip geometric calculation shows accurate reflection to bulk deformation behavior. This comparison ensures the solid contact and stress recording during this indentation process. Therefore, the ultra-low stress level (~ 0.1 GPa) of ITB migration is a striking observation, because this phenomenon occurs before plastic yielding, or even dislocations nucleation in this study. However, ITB migration is clearly not elastic deformation since these ITBs does not revert back after the migration. Also, this may not qualifier for plastic deformation as dislocation has not been nucleated thus no dislocation interaction is observed at this regime.

Recent studies revealed that twin is less stable when the average twin spacing is a few nanometers [51, 52]. Wang et al. [200] reported 0.3 GPa shear stress is sufficient for ITB migration of 2 nm twinned Cu crystal using MD simulation. Furthermore, low stress triggers deformation twins in Cu have been seen in several studies both experimentally and theoretically [154, 203]. Their estimated Cu twin formation shear stress is ~ 0.12 GPa. Our study first evident the ITB migration of 5 nm thick twin could occurs at theoretical twin formation shear stress ~ 0.1GPa, where no dislocation interaction has been captured. This leads to a major question, what is the mechanism of ITB migration?

A typical ITB boundaries is 3 atomic layer repeating structure, marked as $\sum 3(112)$ [47], where the sets of partials stay together due to the net Burgers vector is zero. Therefore, when applied shear stress is enough to destroy the $\sum 3(112)$ boundary, ITB migration occurs due to non-zero net Burgers vector. This mechanism is supported by the

observation of load plateau and load drop. First, the loss of energy providing by shear stress when destroying the ∑3(112) boundary leads to the load plateau from -17s. Then, the fine twins has migrated to lower shear stress regime that shear stress is insufficient to trigger more ITB migration. After that, the measured indentation stress drops to nearly zero at 18s, which corresponds to the regeneration of shear stress field. Therefore, we think ITB migration is a non-dislocation interaction, non-revertible process, which is neither elastic nor plastic deformation.

It worth noticing that the ITB migration speed is estimated as 15 nm/s, which is much smaller than simulation results (>5m/s [200]). This is due to large loading rate differences between simulation and experimental results, where shock loading rate in simulation results is several magnitudes faster than our experimental results.

We then discuss the dislocation-twin boundary interaction in the plastic regime. As shown in Fig. 56 and Fig.58, three events can be clearly identified: dislocation nucleation at ~31s; dislocations propagation at ~35s; and dislocation penetration through twin boundaries at 46s. The general understanding of macroscopic plastic yielding is dislocation penetrate through grain boundaries. Therefore, we clearly captured the stress levels of dislocation nucleation and propagation before macroscopic plastic yielding, which corresponds to the dislocation penetration through twin boundaries.

Right at dislocations nucleation occurs at 31s, the area underneath the indenter is almost twinned free and a large number of dislocations nucleate and combine as a network almost immediately. The dislocation density increases from almost 0 to 5.4×10^{11} cm^2 in less than 1s. This leads to the large work-hardening from 31s to 35s, where a first load drop occurs corresponds to dislocation network expanding and propagating at the

twin boundaries as shown in Fig. 58. After 37s, dislocations accumulated and piled-up on the twin boundaries, which maintained large work-hardening. They penetrate through the twin boundaries with larger load drop after 46s. This is clearly the combination of dislocation-network itself interaction, and dislocation-twin interaction. The work-hardening exponents of nt Cu (n_1 and n_2) is comparable with Cu without twins (n_0) as shown in Fig. 56b. This shows coherent twin boundaries can indeed provide strong resistant on dislocation pile-up, and then contribute to the strength.

VI.6 Conclusion

In summary, we report the first *in situ* evidence to identify the phenomenon and corresponding stress level of ITB migration; dislocation nucleation; and dislocation penetration into CTB in one loading event on nanotwinned Cu. We identified the indentation stress drops associate with ITB migration at 0.1 GPa, and dislocation penetration at 0.6-0.8 GPa. In ITB migration regime, twin with 5 nm thickness moves easily than twin with 14 nm thickness. The result show that the ITB migration of the thinner twin occurs at very low stress at 0.1 GPa with about 15 nm/s velocity, whereas the thicker twin can stand even after plastic yielding at 0.6 GPa. In work hardening regime, dislocations nucleation and penetration into twin boundaries are recorded. Dislocation network shows greater work-hardening exponent, where a clear stress drop was evident when dislocation penetrating into twin boundaries. This may corresponds to the plastic yielding captured macroscopically.

CHAPTER VII

SUMMARY

First, we investigate the mechanical properties of sputtered, epitaxial Cobalt (Co) films with 1.2 μm thickness. By applying epitaxial Cu seed layer on Si substrates, epitaxial FCC (100) and HCP (0002) Co films can be achieved, respectively. High density stacking faults with an average spacing of a few nanometers are observed on (0002) Basel planes in HCP Co films. Compared to HCP Co, high density stacking faults intersecting ribbons are observed on different (111) planes. Furthermore, the volume fraction of these stacking faults intersecting ribbons in FCC Co can be controlled by deposition parameters of magnetron sputtering. The indentation hardness of the FCC Co rises from 4 GPa to 5 GPa with increasing the volume fraction of the stacking faults. The formation and strengthening mechanisms of these stacking faults are discussed.

Second, we investigate the interfaces and mechanical properties of sputtered, highly (100) and (111) textured Cu/Co multilayers. In (100) Cu/Co multilayers, Co has primarily face-centered-cubic (FCC) structure and high density of inclined stacking faults (SFs). In contrast in (111) textured Cu/Co, dependent on layer thickness, high density SFs and twins parallel to layer interface are observed. When individual layer thickness, h, is a few nanometers, both systems have fully coherent FCC interface. (111) Cu/Co has similar size dependent strengthening and peak hardness compared to (111) Cu/Ni multilayers. The peak strength of (100) Cu/Co may be dominated by the transmission of partial dislocations across interface, and hence it is lower than the peak strength of (100) Cu/Ni, which is dictated by transmission of full dislocations across interfaces.

Third, nanoindentation technique is increasingly used to determine the strain rate sensitivity (SRS) of materials with small volumes, such as nanocrystalline metallic thin films. However traditional data analysis yields large scattering and uncertainty due to the influence of thermal drift on displacements measured at low strain rates. In the present work, we use a new method that renders hardness insensitive to thermal drift. The method involves (a) directly measuring contact stiffness by means of a small dynamic oscillation and (b) calculating contact area from the measured contact stiffness and the elastic modulus, which is insensitive to strain rate. The new technique is validated on nanocrystalline Ni and nanotwinned Cu films and returns expected values of SRS.

Fourth, we report the first *in situ* evidence to identify the phenomenon and corresponding stress level of incoherent twin boundary (ITB) migration; dislocation nucleation; and dislocation penetration through coherent twin boundary (CTB) in one loading event on epitaxial nanotwinned Cu. We have observed the detwinning process triggered at ultra-low indentation stress level associate with stress plateau and drops before plastic yielding. We found that ITB migration of the thinner twin (~ 5 nm) occurs at very low stress at 0.1 GPa with about 15 nm/s velocity, whereas the thicker twin (~14 nm) can stand until 0.6 GPa. Furthermore, we have captured dislocation nucleation and propagation before macroscopic yielding, which corresponds to dislocation penetration through twin boundaries.

REFERENCES

[1] Hall EO. The deformation and ageing of mild steel: III discussion of results. Proc Phys Soc B 1951;64:747.

[2] Petch NJ. The cleavage strength of polycrystals. J Iron Steel Inst Lond 1953;173:4.

[3] Misra A, Hirth JP, Hoagland RG. Length-scale-dependent deformation mechanisms in incoherent metallic multilayered composites. Acta Mater 2005;53:4817.

[4] Gleiter H. Nanocrystalline materials. Progress in Materials Science 1989;33:223.

[5] Kumar KS, Van Swygenhoven H, Suresh S. Mechanical behavior of nanocrystalline metals and alloys. Acta Mater 2003;51:5743.

[6] Meyers MA, Mishra A, Benson DJ. Mechanical properties of nanocrystalline materials. Progress in Materials Science 2006;51:427.

[7] Chokshi AH, Rosen A, Karch J, Gleiter H. On the validity of the hall-petch relationship in nanocrystalline materials. Scripta Matall 1989;23:1679.

[8] Bakonyi I, Péter L. Electrodeposited multilayer films with giant magnetoresistance (GMR): Progress and problems. Progress in Materials Science 2010;55:107.

[9] Egelhoff WF, Jr., Kief MT. Antiferromagnetic coupling in Fe/Cu/Fe and Co/Cu/Co multilayers on Cu(111). Phys Rev B 1992;45:7795.

[10] Misra A, Kung H. Deformation behavior of nanostructured metallic multilayers. Adv Eng Mater 2001;3:217.

[11] Misra A, Hirth JP, Hoagland RG, Embury JD, Kung H. Dislocation mechanisms and symmetric slip in rolled nano-scale metallic multilayers. Acta Mater 2004;52:2387.

[12] Fu EG, Li N, Misra A, Hoagland RG, Wang H, Zhang X. Mechanical properties of sputtered Cu/V and Al/Nb multilayer films. Mater Sci Eng A 2008;493:283.

[13] Li YP, Zhang GP. On plasticity and fracture of nanostructured Cu/X (X;Au, Cr) multilayers: The effects of length scale and interface/boundary. Acta Mater 2010;58:3877.

[14] Zhang JY, Zhang X, Wang RH, Lei SY, Zhang P, Niu JJ, Liu G, Zhang GJ, Sun J. Length-scale-dependent deformation and fracture behavior of Cu/X (X;Nb, Zr) multilayers: The constraining effects of the ductile phase on the brittle phase. Acta Mater 2011;59:7368.

[15] Demkowicz MJ, Hoagland RG, Hirth JP. Interface structure and radiation damage resistance in Cu-Nb multilayer nanocomposites. Phys Rev Lett 2008;100:136102.

[16] Li N, Nastasi M, Misra A. Defect structures and hardening mechanisms in high dose helium ion implanted Cu and Cu/Nb multilayer thin films. Int J Plast 2012;32–33:1.

[17] Misra A, Demkowicz M, Zhang X, Hoagland R. The radiation damage tolerance of ultra-high strength nanolayered composites. JOM 2007;59:62.

[18] Misra A, Verdier M, Lu YC, Kung H, Mitchell TE, Nastasi M, Embury JD. Structure and mechanical properties of Cu-X (X = Nb,Cr,Ni) nanolayered composites. Scripta Mater 1998;39:555.

[19] Anderson PM, Li C. Hall-Petch relations for multilayered materials. Nanostruct Mater 1995;5:349.

[20] Counts WA, Braginsky MV, Battaile CC, Holm EA. Predicting the Hall–Petch effect in fcc metals using non-local crystal plasticity. Int J Plast 2008;24:1243.

[21] Anderson PM, Carpenter JS. Estimates of interfacial properties in Cu/Ni multilayer thin films using hardness data. Scripta Mater 2010;62:325.

[22] Embury JD, Hirth JP. On dislocation storage and the mechanical response of fine scale microstructures. Acta Metall Mater 1994;42:2051.

[23] Misra A, Hirth JP, Kung H. Single-dislocation-based strengthening mechanisms in nanoscale metallic multilayers. Phil Mag A 2002;82:2935.

[24] Bacon DJ, Barnett DM, Scattergood RO. On the anisotropic elastic field of a dislocation segment in three dimensions. Phil Mag A 1979;39:231.

[25] Koehler JS. Attempt to design a strong solid. Phys Rev B 1970;2:547.

[26] Hoagland RG, Mitchell TE, Hirth JP, Kung H. On the strengthening effects of interfaces in multilayer fcc metallic composites. Phil Mag A 2002;82:643.

[27] Shoykhet B, Grinfeld MA, Hazzledine PM. Internal stresses and strains in coherent multilayers. Acta Mater 1998;46:3761.

[28] McKeown J, Misra A, Kung H, Hoagland RG, Nastasi M. Microstructures and strength of nanoscale Cu–Ag multilayers. Scripta Mater 2002;46:593.

[29] Hull R, Bean JC. Misfit dislocations in lattice-mismatched epitaxial films. Crit Rev Solid State Mater Sci 1992;17:507

[30] Li Q, Anderson PM. Dislocation-based modeling of the mechanical behavior of epitaxial metallic multilayer thin films. Acta Mater 2005;53:1121.

[31] Rao SI, Hazzledine PM. Atomistic simulations of dislocation-interface interactions in the Cu-Ni multilayer system. Phil Mag A 2000;80:2011.

[32] Liu Y, Bufford D, Wang H, Sun C, Zhang X. Mechanical properties of highly textured Cu/Ni multilayers. Acta Mater 2011;59:1924.

[33] Zhang X, Misra A, Wang H, Shen TD, Nastasi M, Mitchell TE, Hirth JP, Hoagland RG, Embury JD. Enhanced hardening in Cu/330 stainless steel multilayers by nanoscale twinning. Acta Mater 2004;52:995.

[34] Beyerlein IJ, Mara NA, Bhattacharyya D, Alexander DJ, Necker CT. Texture evolution via combined slip and deformation twinning in rolled silver–copper cast eutectic nanocomposite. Int J Plast 2011;27:121.

[35] Wang B, Idrissi H, Galceran M, Colla MS, Turner S, Hui S, Raskin JP, Pardoen T, Godet S, Schryvers D. Advanced TEM investigation of the plasticity mechanisms in nanocrystalline freestanding palladium films with nanoscale twins. Int J Plast 2012;37:140.

[36] Wang J, Misra A, Hoagland RG, Hirth JP. Slip transmission across fcc/bcc interfaces with varying interface shear strengths. Acta Mater 2012;60:1503.

[37] Li N, Mara NA, Wang J, Dickerson P, Huang JY, Misra A. Ex situ and in situ measurements of the shear strength of interfaces in metallic multilayers. Scripta Mater 2012;67:479.

[38] Frank FC, van der Merwe JH. One-dimensional dislocations. II. misfitting monolayers and oriented overgrowth. Proc Roy Soc Lond 1949;198:216.

[39] Frank FC, van der Merwe JH. One-dimensional dislocations. I. static theory. Proc Roy Soc Lond 1949;198:205.

[40] Jesser WA, Matthews JW. Pseudomorphic deposits of cobalt on copper. Phil Mag 1968;17:461.

[41] Matthews JW, Blakeslee AE. Defects in epitaxial multilayers. I. Misfit dislocations. J Cryst Growth 1974;27:118.

[42] Tu KN, Mayer JW, Feldman LC. Electronic thin film science: for electrical engineers and materials scientists: Macmillan, 1992.

[43] Li N, Yu KY, Lee J, Wang H, Zhang X. Size dependent strengthening mechanisms in sputtered Fe/W multilayers. J Appl Phys 2010;107:093503 (7 pp.).

[44] Hoagland RG, Kurtz RJ, Henager Jr CH. Slip resistance of interfaces and the strength of metallic multilayer composites. Scripta Mater 2004;50:775.

[45] Misra A, Demkowicz MJ, Wang J, Hoagland RG. The multiscale modeling of plastic deformation in metallic nanolayered composites. JOM 2008;60:39.

[46] Wang J, Hoagland RG, Hirth JP, Misra A. Atomistic simulations of the shear strength and sliding mechanisms of copper-niobium interfaces. Acta Mater 2008;56:3109.

[47] Wang J, Anderoglu O, Hirth JP, Misra A, Zhang X. Dislocation structures of Sigma 3 {112} twin boundaries in face centered cubic metals. Appl Phys Lett 2009;95:021908.

[48] Murr LE. Interfacial phenomena in metals and alloys, 1975.

[49] Hirth JP, Lothe J. Theory of dislocations. New York: Wiley, 1982.

[50] Lu L, Shen Y, Chen X, Qian L, Lu K. Ultrahigh strength and high electrical conductivity in copper. Science 2004;304:422.

[51] Lu L, Chen X, Huang X, Lu K. Revealing the maximum strength in nanotwinned copper. Science 2009;323:607.

[52] Anderoglu O, Misra A, Wang J, Hoagland RG, Hirth JP, Zhang X. Plastic flow stability of nanotwinned Cu foils. Int J Plast 2010;26:875.

[53] Li N, Wang J, Misra A, Zhang X, Huang JY, Hirth JP. Twinning dislocation multiplication at a coherent twin boundary. Acta Mater 2011;59:5989.

[54] Li N, Wang J, Huang JY, Misra A, Zhang X. Influence of slip transmission on the migration of incoherent twin boundaries in epitaxial nanotwinned Cu. Scripta Mater 2011;64:149.

[55] Christian JW, Mahajan S. Deformation twinning. Progress in Materials Science 1995;39:1.

[56] Zhu YT, Liao XZ, Wu XL. Deformation twinning in nanocrystalline materials. Progress in Materials Science 2012;57:1.

[57] Zhang X, Wang H, Chen XH, Lu L, Lu K, Hoagland RG, Misra A. High-strength sputter-deposited Cu foils with preferred orientation of nanoscale growth twins. Appl Phys Lett 2006;88:173116.

[58] Wang YM, Sansoz F, LaGrange T, Ott RT, Marian J, Barbee Jr TW, Hamza AV. Defective twin boundaries in nanotwinned metals. Nature Materials 2013;12:697.

[59] Afanasyev KA, Sansoz F. Strengthening in gold nanopillars with nanoscale twins. Nano Letters 2007;7:2056.

[60] Lu K, Lu L, Suresh S. Strengthening materials by engineering coherent internal boundaries at the nanoscale. Science 2009;324:349.

[61] Hodge AM, Furnish TA, Navid AA, Barbee Jr TW. Shear band formation and ductility in nanotwinned Cu. Scripta Mater 2011;65:1006.

[62] Ma E. Eight routes to improve the tensile ductility of bulk nanostructured metals and alloys. JOM 2006;58:49.

[63] Zhang X, Misra A. Superior thermal stability of coherent twin boundaries in nanotwinned metals. Scripta Mater 2012;66:860.

[64] Anderoglu O, Misra A, Wang H, Zhang X. Thermal stability of sputtered Cu films with nanoscale growth twins. J Appl Phys 2008;103:094322.

[65] Bufford D, Wang H, Zhang X. Thermal stability of twins and strengthening mechanisms in differently oriented epitaxial nanotwinned Ag films. Journal of Materials Research 2013;28:1729.

[66] Bezares J, Jiao S, Liu Y, Bufford D, Lu L, Zhang X, Kulkarni Y, Asaro RJ. Indentation of nanotwinned fcc metals: Implications for nanotwin stability. Acta Mater 2012;60:4623.

[67] Hodge AM, Furnish TA, Shute CJ, Liao Y, Huang X, Hong CS, Zhu YT, Barbee Jr TW, Weertman JR. Twin stability in highly nanotwinned Cu under compression, torsion and tension. Scripta Mater 2012;66:872.

[68] Zhang P, Zhang ZJ, Li LL, Zhang ZF. Twin boundary: Stronger or weaker interface to resist fatigue cracking? Scripta Mater 2012;66:854.

[69] Anderoglu O, Misra A, Wang H, Ronning F, Hundley MF, Zhang X. Epitaxial nanotwinned Cu films with high strength and high conductivity. Appl Phys Lett 2008;93:083108.

[70] Chen K-C, Wu W-W, Liao C-N, Chen L-J, Tu KN. Observation of atomic diffusion at twin-modified grain boundaries in copper. Science 2008;321:1066.

[71] Liao X, Zhou F, Lavernia E, He D, Zhu Y. Deformation twins in nanocrystalline Al. Appl Phys Lett 2003;83:5062.

[72] Zhu K, Vassel A, Brisset F, Lu K, Lu J. Nanostructure formation mechanism of α-titanium using SMAT. Acta Mater 2004;52:4101.

[73] Mahajan S, Pande C, Imam M, Rath B. Formation of annealing twins in fcc crystals. Acta Mater 1997;45:2633.

[74] Kaufmann S, Rößler UK, Heczko O, Wuttig M, Buschbeck J, Schultz L, Fähler S. Adaptive modulations of martensites. Phys Rev Lett 2010;104:145702.

[75] Bufford D, Wang H, Zhang X. High strength, epitaxial nanotwinned Ag films. Acta Mater 2011;59:93.

[76] Anderoglu O, Misra A, Ronning F, Wang H, Zhang X. Significant enhancement of the strength-to-resistivity ratio by nanotwins in epitaxial Cu films. J Appl Phys 2009;106.

[77] Tadmor EB, Hai S. A Peierls criterion for the onset of deformation twinning at a crack tip. Journal of the Mechanics and Physics of Solids 2003;51:765.

[78] Bufford D, Liu Y, Zhu Y, Bi Z, Jia QX, Wang H, Zhang X. Formation mechanisms of high-density growth twins in aluminum with high stacking-fault energy. Materials Research Letters 2013;1:51.

[79] Bufford D, Bi Z, Jia QX, Wang H, Zhang X. Nanotwins and stacking faults in high-strength epitaxial Ag/Al multilayer films. Appl Phys Lett 2012;101:223112.

[80] Liu Y, Bufford D, Rios S, Wang H, Chen J, Zhang JY, Zhang X. A formation mechanism for ultra-thin nanotwins in highly textured Cu/Ni multilayers. J Appl Phys 2012;111:073526.

[81] Chen Y, Liu Y, Sun C, Yu K, Song M, Wang H, Zhang X. Microstructure and strengthening mechanisms in Cu/Fe multilayers. Acta Mater 2012;60:6312.

[82] Yu K, Bufford D, Chen Y, Liu Y, Wang H, Zhang X. Basic criteria for formation of growth twins in high stacking fault energy metals. Appl Phys Lett 2013;103:181903.

[83] Yu K, Liu Y, Rios S, Wang H, Zhang X. Strengthening mechanisms of Ag/Ni immiscible multilayers with fcc/fcc interface. Surface and Coatings Technology 2013.

[84] Freund LB, Suresh S. Thin film materials: stress, defect formation and surface evolution: Cambridge University Press, 2004.

[85] Liao XZ, Zhao YH, Srinivasan SG, Zhu YT, Valiev RZ, Gunderov DV. Deformation twinning in nanocrystalline copper at room temperature and low strain rate. Appl Phys Lett 2004;84:592.

[86] Youssef K, Sakaliyska M, Bahmanpour H, Scattergood R, Koch C. Effect of stacking fault energy on mechanical behavior of bulk nanocrystalline Cu and Cu alloys. Acta Mater 2011;59:5758.

[87] Wu X, Tao N, Hong Y, Liu G, Xu B, Lu J, Lu K. Strain-induced grain refinement of cobalt during surface mechanical attrition treatment. Acta Mater 2005;53:681.

[88] Wu X, Tao N, Hong Y, Lu J, Lu K. $\gamma \rightarrow \varepsilon$ martensite transformation and twinning deformation in fcc cobalt during surface mechanical attrition treatment. Scripta Mater 2005;52:547.

[89] Wu X, Zhu YT, Chen MW, Ma E. Twinning and stacking fault formation during tensile deformation of nanocrystalline Ni. Scripta Mater 2006;54:1685.

[90] Jian WW, Cheng GM, Xu WZ, Koch CC, Wang QD, Zhu YT, Mathaudhu SN. Physics and model of strengthening by parallel stacking faults. Appl Phys Lett 2013;103.

[91] Zhang X, Misra A, Wang H, Nastasi M, Embury JD, Mitchell TE, Hoagland RG, Hirth JP. Nanoscale-twinning-induced strengthening in austenitic stainless steel thin films. Appl Phys Lett 2004;84:1096.

[92] Yu KY, Bufford D, Sun C, Liu Y, Wang H, Kirk MA, Li M, Zhang X. Removal of stacking-fault tetrahedra by twin boundaries in nanotwinned metals. Nat Commun 2013;4:1377.

[93] Jian WW, Cheng GM, Xu WZ, Yuan H, Tsai MH, Wang QD, Koch CC, Zhu YT, Mathaudhu SN. Ultrastrong Mg alloy via nano-spaced stacking faults. Materials Research Letters 2013;1:61.

[94] Wang H, Tiwari A, Kvit A, Zhang X, Narayan J. Epitaxial growth of TaN thin films on Si(100) and Si(111) using a TiN buffer layer. Appl Phys Lett 2002;80:2323.

[95] Wegscheider W, Eberl K, Abstreiter G, Cerva H, Oppolzer H. Novel relaxation process in strained Si/Ge superlattices grown on Ge(001). Appl Phys Lett 1990;57:1496.

[96] Neethling JH, Alberts V. Multiple twinning in GaAs epitaxial layers grown on Si(001) and Si(111). J Appl Phys 1994;75:3435.

[97] Dynna M, Marty A, Gilles B, Patrat G. On the nature of L10 ordering in equiatomic AuNi and AuCu thin films grown on Au(001). Acta Mater 1997;45:257.

[98] Liu L, Zhang Y, Zhang T-Y. Strain relaxation in heteroepitaxial films by misfit twinning. I. Critical thickness. J Appl Phys 2007;101:63501.

[99] Zhang Y, Liu L, Zhang T-Y. Strain relaxation in heteroepitaxial films by misfit twinning: II. Equilibrium morphology. J Appl Phys 2007;101.

[100] Dorn JE, Shanley FR. Mechanical behavior of materials at elevated temperatures. New York: McGraw-Hill, 1961.

[101] Amin KE, Mukherjee AK, Dorn JE. A universal law for high-temperature diffusion controlled transient creep. Journal of the Mechanics and Physics of Solids 1970;18:413.

[102] Wei Q. Strain rate effects in the ultrafine grain and nanocrystalline regimes—influence on some constitutive responses. J Mater Sci 2007;42:1709.

[103] Conrad H. High strength materials. John Wiley, New York 1965;1:145.

[104] Dorn J, Mitchell J. High strength materials. John Wiley, New York 1965:510.

[105] Stach EA, Freeman T, Minor AM, Owen DK, Cumings J, Wall MA, Chraska T, Hull R, Morris JW, Jr. A, Zettl U. Development of a Nanoindenter for In Situ Transmission Electron Microscopy. Microscopy and Microanalysis 2001;7:507.

[106] Cao QP, Liu JW, Yang KJ, Xu F, Yao ZQ, Minkow A, Fecht HJ, Ivanisenko J, Chen LY, Wang XD, Qu SX, Jiang JZ. Effect of pre-existing shear bands on the tensile mechanical properties of a bulk metallic glass. Acta Mater 2010;58:1276.

[107] Lu Y, Huang JY, Wang C, Sun S, Lou J. Cold welding of ultrathin gold nanowires. Nat Nano 2010;5:218.

[108] Oh SH, Legros M, Kiener D, Dehm G. In situ observation of dislocation nucleation and escape in a submicrometre aluminium single crystal. Nature Materials 2009;8:95.

[109] Lee JH, Kim I, Hulbert DM, Jiang D, Mukherjee AK, Zhang X, Wang H. Grain and grain boundary activities observed in alumina–zirconia–magnesia spinel nanocomposites by in situ nanoindentation using transmission electron microscopy. Acta Mater 2010;58:4891.

[110] Zheng H, Cao A, Weinberger CR, Huang JY, Du K, Wang J, Ma Y, Xia Y, Mao SX. Discrete plasticity in sub-10-nm-sized gold crystals. Nature communications 2010;1:144.

[111] De Hosson J, Soer W, Minor A, Shan Z, Stach E, Syed Asif S, Warren O. In situ TEM nanoindentation and dislocation-grain boundary interactions: a tribute to David Brandon. J Mater Sci 2006;41:7704.

[112] Jin M, Minor AM, Stach EA, Morris Jr JW. Direct observation of deformation-induced grain growth during the nanoindentation of ultrafine-grained Al at room temperature. Acta Mater 2004;52:5381.

[113] Minor AM, Syed Asif SA, Shan Z, Stach EA, Cyrankowski E, Wyrobek TJ, Warren OL. A new view of the onset of plasticity during the nanoindentation of aluminium. Nature Materials 2006;5:697.

[114] Shan ZW, Mishra RK, Syed Asif SA, Warren OL, Minor AM. Mechanical annealing and source-limited deformation in submicrometre-diameter Ni crystals. Nature Materials 2008;7:115.

[115] Lee JH, Holland TB, Mukherjee AK, Zhang X, Wang H. Direct observation of Lomer-Cottrell Locks during strain hardening in nanocrystalline nickel by in situ TEM. Sci. Rep. 2013;3:1061.

[116] Ohmura T, Minor AM, Stach EA, Morris JW. Dislocation–grain boundary interactions in martensitic steel observed through in situ nanoindentation in a transmission electron microscope. Journal of Materials Research 2004;19:3626.

[117] Kiener D, Hosemann P, Maloy SA, Minor AM. In situ nanocompression testing of irradiated copper. Nature Materials 2011;10:608.

[118] Soer WA, Hosson JTMD, Minor AM, Morris Jr JW, Stach EA. Effects of solute Mg on grain boundary and dislocation dynamics during nanoindentation of Al–Mg thin films. Acta Mater 2004;52:5783.

[119] Li N, Wang J, Huang JY, Misra A, Zhang X. In situ TEM observations of room temperature dislocation climb at interfaces in nanolayered Al/Nb composites. Scripta Mater 2010;63:363.

[120] Bragg WL. The diffraction of short electromagnetic waves by a crystal. Proceedings of the Cambridge Philosophical Society, vol. 17, 1913. p.43.

[121] Oliver WC, Pharr GM. An improved technique for determining hardness and elastic modulus using load and displacement sensing indentation experiments. Journal of Materials Research 1992;7:1564.

[122] Pethica J, Oliver W. Mechanical properties of nanometer volumes of material: use of the elastic response of small area indentations. Thin Films—Stresses and Mechanical Properties, MRS Symposium Proc, vol. 130: Cambridge Univ Press, 1989. p.13.

[123] Herbert EG, Pharr GM, Oliver WC, Lucas BN, Hay JL. On the measurement of stress–strain curves by spherical indentation. Thin Solid Films 2001;398–399:331.

[124] Zhu T, Li J. Ultra-strength materials. Progress in Materials Science 2010;55:710.

[125] Liu Y, Chen Y, Yu KY, Wang H, Chen J, Zhang X. Stacking fault and partial dislocation dominated strengthening mechanisms in highly textured Cu/Co multilayers. Int J Plast 2013;49:152.

[126] Betteridge W. The properties of metallic cobalt. Progress in Materials Science 1980;24:51.

[127] Spriano S, Vernè E, Faga MG, Bugliosi S, Maina G. Surface treatment on an implant cobalt alloy for high biocompatibility and wear resistance. Wear 2005;259:919.

[128] Aykut Ş, Bagci E, Kentli A, Yazıcıoğlu O. Experimental observation of tool wear, cutting forces and chip morphology in face milling of cobalt based super-alloy with physical vapour deposition coated and uncoated tool. Mater Design 2007;28:1880.

[129] Kim SH, Aust KT, Erb U, Gonzalez F, Palumbo G. A comparison of the corrosion behaviour of polycrystalline and nanocrystalline cobalt. Scripta Mater 2003;48:1379.

[130] Wang YM, Ma E. On the origin of ultrahigh cryogenic strength of nanocrystalline metals. Appl Phys Lett 2004;85:2750.

[131] Karimpoor AA, Erb U, Aust KT, Palumbo G. High strength nanocrystalline cobalt with high tensile ductility. Scripta Mater 2003;49:651.

[132] Ericsson T. The temperature and concentration dependence of the stacking fault energy in the Co-Ni system. Acta Metall 1966;14:853.

[133] Zheng G-P. Grain-size effect on plastic flow in nanocrystalline cobalt by atomistic simulation. Acta Mater 2007;55:149.

[134] Zheng GP, Wang YM, Li M. Atomistic simulation studies on deformation mechanism of nanocrystalline cobalt. Acta Mater 2005;53:3893.

[135] Zheng GP. Molecular dynamics and first-principles studies on the deformation mechanisms of nanostructured cobalt. J Alloy Compd 2010;504:467.

[136] Huang JY, Wu YK, Ye HQ. Phase transformation of cobalt induced by ball milling. Appl Phys Lett 1995:308.

[137] Jesser WA, Matthews JW. Growth of f.c.c. cobalt on nickel. Acta Metall 1968;16:1307.

[138] Schneider CM, Hammond MS, Schuster P, Cebollada A, Miranda R, Kirschner J. Observation of magnetic circular dichroism in uv photoemission from ferromagnetic fcc cobalt films. Phys Rev B 1991;44:12066.

[139] Aeschlimann M, Bauer M, Pawlik S, Weber W, Burgermeister R, Oberli D, Siegmann HC. Ultrafast spin-dependent electron dynamics in fcc Co. Phys Rev Lett 1997;79:5158.

[140] Abu Al-Rub RK. Interfacial gradient plasticity governs scale-dependent yield strength and strain hardening rates in micro/nano structured metals. Int J Plast 2008;24:1277.

[141] Wang J, Hoagland RG, Hirth JP, Misra A. Atomistic modeling of the interaction of glide dislocations with "weak" interfaces. Acta Mater 2008;56:5685.

[142] Wang J, Misra A. An overview of interface-dominated deformation mechanisms in metallic multilayers. Curr Opin Solid State Mater Sci 2011;15:20.

[143] Misra A, Verdier M, Kung H, Embury JD, Hirth JP. Deformation mechanism maps for polycrystalline metallic multilayers. Scripta Mater 1999;41:973.

[144] Zbib HM, Overman CT, Akasheh F, Bahr D. Analysis of plastic deformation in nanoscale metallic multilayers with coherent and incoherent interfaces. Int J Plast 2011;27:1618.

[145] Banerjee R, Ahuja R, Fraser HL. Dimensionally induced structural transformations in titanium-aluminum multilayers. Phys Rev Lett 1996;76:3778.

[146] Banerjee R, Zhang XD, Dregia SA, Fraser HL. Phase stability in Al/Ti multilayers. Acta Mater 1999;47:1153.

[147] Ahuja R, Fraser H. Structure and mechanical properties of nanolaminated Ti-Al thin films. JOM 1994;46:35.

[148] Zhang JY, Liu Y, Chen J, Chen Y, Liu G, Zhang X, Sun J. Mechanical properties of crystalline Cu/Zr and crystal–amorphous Cu/Cu–Zr multilayers. Mater Sci Eng A 2012;552:392.

[149] Zhu XY, Luo JT, Chen G, Zeng F, Pan F. Size dependence of creep behavior in nanoscale Cu/Co multilayer thin films. J Alloy Compd 2010;506:434.

[150] Nallet P, Chassaing E, Walls MG, Hytch MJ. Interface characterization in electrodeposited Cu/Co multilayers. J Appl Phys 1996;79:6884.

[151] Gómez E, Labarta A, Llorente A, Vallés E. Electrochemical behaviour and physical properties of Cu/Co multilayers. Electrochim Acta 2003;48:1005.

[152] Johnson MT, Bloemen PJH, Broeder FJAd, Vries JJd. Magnetic anisotropy in metallic multilayers. Reports on Progress in Physics 1996;59:1409.

[153] Lagerlöf KPD, Castaing J, Pirouz P, Heuer AH. Nucleation and growth of deformation twins: A perspective based on the double-cross-slip mechanism of deformation twinning. Phil Mag A 2002;82:2841.

[154] Kibey S, Liu JB, Johnson DD, Sehitoglu H. Predicting twinning stress in fcc metals: Linking twin-energy pathways to twin nucleation. Acta Mater 2007;55:6843.

[155] Cotterill RMJ, Doyama M. Energy and atomic configuration of complete and dissociated dislocations. I. edge dislocation in an fcc metal. Phys Rev 1966;145:465.

[156] Häkkinen H, Mäkinen S, Manninen M. Edge dislocations in fcc metals: Microscopic calculations of core structure and positron states in Al and Cu. Phys Rev B 1990;41:12441.

[157] Zhang X, Misra A, Wang H, Lima AL, Hundley MF, Hoagland RG. Effects of deposition parameters on residual stresses, hardness and electrical resistivity of nanoscale twinned 330 stainless steel thin films. J Appl Phys 2005;97:1.

[158] Liu Y, Hay J, Wang H, Zhang X. A new method for reliable determination of strain-rate sensitivity of low-dimensional metallic materials by using nanoindentation. Scripta Mater 2014;77:5.

[159] Horita Z, Furukawa M, Nemoto M, Barnes AJ, Langdon TG. Superplastic forming at high strain rates after severe plastic deformation. Acta Mater 2000;48:3633.

[160] Sergueeva AV, Stolyarov VV, Valiev RZ, Mukherjee AK. Superplastic behaviour of ultrafine-grained Ti–6A1–4V alloys. Mater Sci Eng A 2002;323:318.

[161] Hedworth J, Stowell MJ. The measurement of strain-rate sensitivity in superplastic alloys. J Mater Sci 1971;6:1061.

[162] Lu L, Li SX, Lu K. An abnormal strain rate effect on tensile behavior in nanocrystalline copper. Scripta Mater 2001;45:1163.

[163] Dalla Torre F, Van Swygenhoven H, Victoria M. Nanocrystalline Electrodeposited Ni: Microstructure and Tensile Properties. Acta Materialia 2002;50:3957.

[164] Valiev RZ, Alexandrov IV, Zhu YT, Lowe TC. Paradox of strength and ductility in metals processed bysevere plastic deformation. Journal of Materials Research 2002;17:5.

[165] Wang YM, Ma E. Temperature and strain rate effects on the strength and ductility of nanostructured copper. Appl Phys Lett 2003;83:3165.

[166] Wei Q, Cheng S, Ramesh KT, Ma E. Effect of nanocrystalline and ultrafine grain sizes on the strain rate sensitivity and activation volume: Fcc versus bcc metals. Mater Sci Eng A 2004;381:71.

[167] Gu C, Lian J, Jiang Z, Jiang Q. Enhanced tensile ductility in an electrodeposited nanocrystalline Ni. Scripta Mater 2006;54:579.

[168] May J, Höppel HW, Göken M. Strain rate sensitivity of ultrafine-grained aluminium processed by severe plastic deformation. Scripta Mater 2005;53:189.

[169] Li YJ, Mueller J, Höppel HW, Göken M, Blum W. Deformation kinetics of nanocrystalline nickel. Acta Mater 2007;55:5708.

[170] Cheng S, Ma E, Wang YM, Kecskes LJ, Youssef KM, Koch CC, Trociewitz UP, Han K. Tensile properties of in situ consolidated nanocrystalline Cu. Acta Mater 2005;53:1521.

[171] Dalla Torre FH, Pereloma EV, Davies CHJ. Strain hardening behaviour and deformation kinetics of Cu deformed by equal channel angular extrusion from 1 to 16 passes. Acta Mater 2006;54:1135.

[172] Wang YM, Hamza AV, Ma E. Temperature-dependent strain rate sensitivity and activation volume of nanocrystalline Ni. Acta Mater 2006;54:2715.

[173] Zhang X, Wang H, Scattergood RO, Narayan J, Koch CC, Sergueeva AV, Mukherjee AK. Studies of deformation mechanisms in ultra-fine-grained and nanostructured Zn. Acta Mater 2002;50:4823.

[174] Mayo MJ, Siegel RW, Liao YX, Nix WD. Nanoindentation of nanocrystalline ZnO. Journal of Materials Research 1992;7:973.

[175] Mayo MJ, Siegel RW, Narayanasamy A, Nix WD. Mechanical properties of nanophase TiO₂ as determined by nanoindentation. Journal of Materials Research 1990;5:1073.

[176] Maier V, Durst K, Mueller J, Backes B, Hoppel HW, Goken M. Nanoindentation strain-rate jump tests for determining the local strain-rate sensitivity in nanocrystalline Ni and ultrafine-grained Al. Journal of Materials Research 2011;26:1421.

[177] Pollock HM, Maugis D, Barquins M. Characterization of submicrometre surface layers by indentation. In: Blau PJ, Lawn BR, editors. Microindentation Techniques in Materials Science and Engineering. Philadelphia: ASTM, 1986. p.47.

[178] Lucas BN, Oliver WC. Indentation power-law creep of high-purity indium. Metall Mater Trans A 1999;30:601.

[179] Hay J, Agee P, Herbert E. Continuous stiffness measurement during instrumented indentation testing. Experimental Techniques 2010;34:86.

[180] Maier V, Merle B, Göken M, Durst K. An improved long-term nanoindentation creep testing approach for studying the local deformation processes in nanocrystalline metals at room and elevated temperatures. Journal of Materials Research 2013;28:1177.

[181] Weihs TP, Pethica JB. Monitoring time-dependent deformation in small volumes. MRS Online Proceedings Library 1991;239:null.

[182] Sneddon IN. The relation between load and penetration in the axisymmetric boussinesq problem for a punch of arbitrary profile. International Journal of Engineering Science 1965;3:47.

[183] Pharr GM, Oliver WC, Brotzen FR. On the generality of the relationship among contact stiffness, contact area, and elastic modulus during indentation. Journal of Materials Research 1992;7:613.

[184] Schwaiger R, Moser B, Dao M, Chollacoop N, Suresh S. Some critical experiments on the strain-rate sensitivity of nanocrystalline nickel. Acta Mater 2003;51:5159.

[185] Shen YF, Xue WY, Wang YD, Liu ZY, Zuo L. Mechanical properties of nanocrystalline nickel films deposited by pulse plating. Surface and Coatings Technology 2008;202:5140.

[186] Gray Iii GT, Lowe TC, Cady CM, Valiev RZ, Aleksandrov IV. Influence of strain rate & temperature on the mechanical response of ultrafine-grained Cu, Ni, and Al-4Cu-0.5Zr. Nanostruct Mater 1997;9:477.

[187] Pan D, Nieh TG, Chen MW. Strengthening and softening of nanocrystalline nickel during multistep nanoindentation. Appl Phys Lett 2006;88:161922.

[188] Chen J, Lu L, Lu K. Hardness and strain rate sensitivity of nanocrystalline Cu. Scripta Mater 2006;54:1913.

[189] Carreker Jr RP, Hibbard Jr WR. Tensile deformation of high-purity copper as a function of temperature, strain rate, and grain size. Acta Metall 1953;1:654.

[190] Jiang Z, Liu X, Li G, Jiang Q, Lian J. Strain rate sensitivity of a nanocrystalline Cu synthesized by electric brush plating. Appl Phys Lett 2006;88:143115.

[191] Ye JC, Wang YM, Barbee JTW, Hamza AV. Orientation-dependent hardness and strain rate sensitivity in nanotwin copper. Appl Phys Lett 2012;100:261912.

[192] Cahn JW, Nabarro FRN. Thermal activation under shear. Phil Mag A 2001;81:1409.

[193] Dao M, Lu L, Asaro RJ, De Hosson JTM, Ma E. Toward a quantitative understanding of mechanical behavior of nanocrystalline metals. Acta Mater 2007;55:4041.

[194] Jin ZH, Gumbsch P, Albe K, Ma E, Lu K, Gleiter H, Hahn H. Interactions between non-screw lattice dislocations and coherent twin boundaries in face-centered cubic metals. Acta Mater 2008;56:1126.

[195] Zhu T, Gao H. Plastic deformation mechanism in nanotwinned metals: An insight from molecular dynamics and mechanistic modeling. Scripta Mater 2012;66:843.

[196] Asaro RJ, Suresh S. Mechanistic models for the activation volume and rate sensitivity in metals with nanocrystalline grains and nano-scale twins. Acta Mater 2005;53:3369.

[197] Zhu T, Li J, Samanta A, Kim HG, Suresh S. Interfacial plasticity governs strain rate sensitivity and ductility in nanostructured metals. Proc. Natl. Acad. Sci. 2007;104:3031.

[198] Wang J, Misra A, Hirth JP. Shear response of Σ3{112} twin boundaries in face-centered-cubic metals. Phys Rev B 2011;83:064106.

[199] Wang YB, Sui ML, Ma E. In situ observation of twin boundary migration in copper with nanoscale twins during tensile deformation. Phil Mag Let 2007;87:935.

[200] Wang J, Li N, Anderoglu O, Zhang X, Misra A, Huang JY, Hirth JP. Detwinning mechanisms for growth twins in face-centered cubic metals. Acta Mater 2010;58:2262.

[201] Zhu YT, Wu XL, Liao XZ, Narayan J, Kecskés LJ, Mathaudhu SN. Dislocation–twin interactions in nanocrystalline fcc metals. Acta Mater 2011;59:812.

[202] Ma E, Wang YM, Lu QH, Sui ML, Lu L, Lu K. Strain hardening and large tensile elongation in ultrahigh-strength nano-twinned copper. Appl Phys Lett 2004;85:4932.

[203] Yamamoto A, Narita N, Takamura J-i, Sakamoto H, Matsuo N. Stacking fault energy and deformation twinning in copper crystals. J Jpn I Met 1983;47:903.